# Measurement of the Prompt J/Psi Pair Production Cross Section in pp Collisions at sqrt(s) = 8 TeV with CMS

A Dissertation Presented for the

Doctor of Philosophy

Degree

The University of Tennessee, Knoxville

Grant Valentine Riley

December 2017

© by Grant Valentine Riley, 2017
All Rights Reserved.

*Dedicated to my parents*

# Acknowledgments

I would like to thank my Ph.D. advisor, Dr. Stefan Spanier for providing me with the motivation funding and opportunity to travel to CERN and participate in exciting research. Through his project I met many mentors and friends, who have all contributed to this thesis in their own way. Specifically I would like to thank my supervisors and predecessors, Andrew York, Dean Hidas, Keith Rose and Paul Lujan for their guidance and assistance. I would like to thank the CMS BRIL group and the B-Physics group for their role in educating me over the course of my hardware project and analysis respectively. Also I would like to thank by name several friends and family who have helped me complete this thesis by being supportive and available when I needed them. Thank you to Pieter, Judy, Cooper and Karson Riley, Johnna Easter, Cory Thornsberry and Paul Thompson.

# Abstract

The cross section for the prompt production of $J/\psi$ [J/Psi] meson pairs in proton-proton collisions at $\sqrt{s}$[sqrt(s)] = 8 TeV at the LHC from a sample corresponding to an integrated luminosity of $20.2 \pm 0.5$ fb$^{-1}$ [inverse femtobarns] has been measured with the CMS detector. It provides unique insight into particle production and proton structure in proton-proton (pp) collisions. The two $J/\psi$ mesons are fully reconstructed in their $\mu^+\mu^-$[mu+ mu-] decay. An acceptance region is defined by the individual $J/\psi$ transverse momentum $p_{\mathrm{T}}^{J/\psi}$ [J/Psi pT] and rapidity $|y^{J/\psi}|$ [J/Psi Rapidity]. The total fiducial cross section assuming unpolarized prompt $J/\psi$ pair production is found to be $\sigma_{fid} = 195.7 \pm 11.1\ (stat) \pm 22.1\ (syst) \pm 5.1\ (lumi) \pm 2.3\ (BF)$ pb. The differential cross sections for prompt $J/\psi$ pair production within this acceptance region are measured in eight event variables.

Most predictions for particle production in pp collisions at the LHC assume dominance of single parton (gluon, quark) interactions (SPS) at the leading order perturbation theory. This assumption is tested with the final state measured in this analysis. Significant contributions from next-to-leading order processes and double parton scattering (DPS) are observed.

In addition, the single $J/\psi$ production cross section is estimated from theory and measured with pp collision data. Single $J/\psi$ production is compared to the pair production via DPS and quantified via an effective cross section. This quantity is further compared to several particle pair production processes. In particular, the $J/\psi$ pair production probes the contributions of gluons.

All particle production measurements with CMS depend on the precise knowledge of the LHC luminosity. A detector, the Pixel Luminosity Telescope, based on solid state technology is used to count charged particle tracks from pp collisions, a measure of the instantaneous

luminosity. The measurement is provided online for every crossing of the LHC beams. Tests of sensors and the development work for the detector are presented.

# Table of Contents


**1 Motivation and Physics Background** **1**

1.1 Background . . . 1

1.2 The Standard Model of Particle Physics . . . 2

1.2.1 Elementary Particles . . . 2

1.2.2 The Fundamental Forces . . . 4

1.3 Quantum Chromodynamics at the LHC . . . 7

1.3.1 High Energy Interactions . . . 7

1.3.2 Color Singlet and Color Octet States . . . 9

**2 Experimental Setup** **11**

2.1 The Large Hadron Collider . . . 11

2.2 The Compact Muon Solenoid . . . 16

2.2.1 The Silicon Pixel Detector and Silicon Strip Tracker . . . 19

2.2.2 The Muon Detection System . . . 20

2.3 Event Selection and Reconstruction . . . 24

2.3.1 Event Selection . . . 24

2.3.2 Reconstruction . . . 26

**3 The Pixel Luminosity Telescope** **30**

3.1 The Luminosity Measurement . . . 30

3.2 The Pixel Luminosity Telescope . . . 32

3.3 Diamond Based Detector Studies . . . 36

3.3.1 Pixelated Diamond Tests . . . 36

3.3.2 TCT studies . . . 41

**4 Data Analysis** **46**

4.1 Motivation . . . 46
4.2 Analysis Strategy . . . 50
4.3 Samples . . . 51
4.3.1 Data . . . 51
4.3.2 Simulation . . . 51
4.4 Event Selection and Reconstruction . . . 53
4.4.1 Initial Selection . . . 53
4.5 Acceptance Definition . . . 55
4.6 Signal Extraction . . . 59
4.6.1 Fit to Baseline Sample . . . 60
4.6.2 Fit to Final Sample . . . 63
4.6.3 Pileup Dependence . . . 66
4.7 Acceptance and Efficiency Correction . . . 69
4.7.1 Model Contribution Fit . . . 69
4.7.2 Single Muon Efficiency . . . 72
4.8 $J/\psi$ Polarization . . . 75
4.9 Systematic Uncertainties . . . 77
4.10 Cross Section Measurement . . . 85
4.11 Effective Cross Section . . . 92
4.11.1 Single $J/\psi$ Cross Section Scaling . . . 92
4.11.2 DPS Cross Section . . . 95
4.11.3 Result . . . 98

**5 Conclusion** **100**

5.1 Review and Discussion . . . 100
5.2 Summary and Outlook . . . 105

**Bibliography** **107**

**Vita** **118**

# List of Tables


1.1 The fundamental interactions described by the standard model . . . . . 6

4.1 The data set used in this analysis and the corresponding integrated luminosity ($\mathcal{L}$). . . . . 52

4.2 The event yield after successive applications of initial quality criteria for the selection of $J/\psi J/\psi$ candidates. Also shown is the % reduction in sample size due to each requirement. . . . . 54

4.3 The absolute correlation factors between four 4-Muon kinematic variables are listed for the data sample and compared to the MC samples at reco and gen level. The generator level MC samples are required to be within the $J/\psi$ acceptance. . . . . 58

4.4 The parameters used in the two variable fit to $ct_{xy}$ and Distance Significance for signal (sig) and background (bkg) (G: Gaussian, Exp: Exponential, L: Landau, pol2: Chebyshev polynomial of degree 2). . . . . 62

4.5 The parameterization of the one variable Maximum Likelihood Fit. . . . . 66

4.6 The summary of relative systematic uncertainties in the differential cross section measurements. The values with ranges show the highest and lowest systematic uncertainty for the 8 variables. The rows without ranges indicate that the systematic uncertainty is kept constant for all bins and all variables. The uncertainty on the branching fraction and luminosity are kept separate from the other uncertainties for the measurement, and not included in the differential plots. . . . . 82

4.7 Summary of the differential cross section measured in bins of 4-muon mass, $M^{JJ}$, listed together with the signal yield $N_{sig}$ extracted with a ML fit. The uncertainties are statistical first, then systematic. . . . . 87
4.8 Summary of the differential cross section measured in bins of 4-muon transverse momentum, $p_{\mathrm{T}}^{JJ}$, listed together with the signal yield $N_{sig}$ extracted with a ML fit. The uncertainties are statistical first, then systematic. . . . . 88
4.9 Summary of the differential cross section measured in bins of absolute 4-muon rapidity, $|y|$, listed together with the signal yield $N_{sig}$ extracted with a ML fit. The uncertainties are statistical first, then systematic. . . . . 88
4.10 Summary of the differential cross section measured in bins of absolute difference in rapidity between the $J/\psi$, $|\Delta y|$, listed together with the signal yield $N_{sig}$ extracted with a ML fit. The uncertainties are statistical first, then systematic. . . . . 88
4.11 Summary of the differential cross section measured in bins of absolute difference in $\phi$ angle between the $J/\psi$, $|\Delta\phi|$, listed together with the signal yield $N_{sig}$ extracted with a ML fit. The uncertainties are statistical first, then systematic. . . . . 90
4.12 Summary of the differential cross section measured in bins of the transverse momentum momentum $p_{\mathrm{T}}^{J_1}$ for the high-$p_{\mathrm{T}}$ $J/\psi$, listed together with the signal yield $N_{sig}$ extracted with a ML fit. The uncertainties are statistical first, then systematic. . . . . 90
4.13 Summary of the differential cross section measured in bins of the transverse momentum $p_{\mathrm{T}}^{J_2}$ for the low-$p_{\mathrm{T}}$ $J/\psi$, listed together with the signal yield $N_{sig}$ extracted with a ML fit. The uncertainties are statistical first, then systematic. . . . . 90
4.14 Summary of the differential cross section measured in bins of The $p_{\mathrm{T}}$ asymmetry of the $J/\psi$, $p_{\mathrm{T}}^{J/\psi}\mathcal{A}$, together with the signal yield $N_{sig}$ extracted with a ML fit. The uncertainties are statistical first, then systematic. . . . . 90
4.15 The integral of each differential cross section distribution. The uncertainty is statistical first, then systematic. . . . . 91

4.16 Summary of the relative systematic uncertainties. . . . . 98

# List of Figures

1.1 The particles of the Standard Model (SM) categorized into quarks, leptons and bosons . . . . . 4
1.2 A rendition of a high energy proton, where sea quarks and gluons become the more dominant producers of pp collisions . . . . . 5
1.3 The left most interaction can describe a gluon splitting into a quark-antiquark pair, a quark-antiquark annihilation forming a gluon, or a quark emitting or absorbing a gluon. The center diagram shows an excited gluon emitting another gluon, or two gluons fusing into one. The right diagram shows a pair of gluons interacting to exchange quantum numbers. . . . . 7

2.1 A schematic of the LHC accelerator complex. The 4 major experiments and the primary CERN site are labeled, with the Compact Muon Solenoid detector circled in red. . . . . 11
2.2 A schematic of all the accelerator facilities at CERN. The arrows show the direction of particle beams in each accelerator, the gray arrows representing the proton beams. . . . . 12
2.3 A schematic of a full bunch pattern in the LHC, showing the various gaps to accommodate kicker magnets. 72 bunch groups, called batches are accelerated in the PS and delivered to the SPS. The SPS then further accelerates the protons and transfers groups of 3 or 4 batches into the LHC. . . . . 13

2.4 Production rates, corresponding to cross sections are shown for various center of mass energies. In the LHC regime, the total production $\sigma_{tot}$ can be seen to be 100 mb, with the highest Higgs production mode $\sigma_{ggH} = \sim 20$ pb, many orders of magnitude lower. . . . . 15

2.5 A cutaway of the CMS detector, with persons shown for scale comparison. The outermost layers are muon detectors placed between slabs of iron absorbers. The iron layers also function as return yoke for the magnetic field. From outside inwards the muon detectors are followed by the superconducting solenoid,the hadronic calorimeter, the electromagnetic calorimeter, the silicon strip tracker, and the innermost 3 layers are the silicon pixel detector. The beam pipe enters from each end of CMS and collisions take place in the center of the detector. . . . . 17

2.6 A diagram of the sagitta $s$ for a particle passing through a region of length $L$ with a constant magnetic field. . . . . 18

2.7 A diagram of the silicon pixel detector's barrel layers (green) and endcap disks (red). . . . . 20

2.8 Shown is a cutaway diagram of the pixelated ROCs bump bonded to a silicon sensor. . . . . 21

2.9 The mechanism of charge creation in a material is illustrated. An incident particle deposits energy in the form of electron/hole pairs which are drifted to the edges of the material by means of an applied electric field. The thickness D is about 300 $\mu m$ for CMS silicon detectors, and the typical electric field is $0.1 V/\mu m$ . . . . . 21

2.10 A single quarter of the CMS detector, the interaction point is located at the bottom left corner of the diagram. The components of the muon detection chambers are labeled, and the value of $\eta$ for various angles ($\lambda$) with respect to the z axis is shown. . . . . 22

2.11 Dimuon Invariant mass for events collected with the various quarkonia related triggers. Strong excesses are observed where triggers include requirements on mass ranges, such as around $J/\psi$ (red), $\psi$' (dark blue), and the set of Y resonances (light green). The signal $Z \to \mu\mu$ is clearly visible around 90 GeV 25

2.12 Top: A transverse slice of CMS with various types of particle tracks and their measurable signatures. Bottom: A CMS event display [99] which shows pixel and tracker tracks in dark yellow, ECAL deposits as green towers, HCAL deposits as blue towers, and Muon station hits in bright green (the muon station recording the hit is outlined in red). The tracks of 2 possible muon candidates are highlighted with red lines, and 2 large ECAL deposits can be found. This event is a candidate 4-lepton final state which can be produced by $J/\psi$ pair, or Higgs→ZZ for example. . . . . 29

3.1 This plot shows the integrated luminosity delivered to the CMS detector during the years 2010 (green), 2011 (red), and 2012 (blue). . . . . 31

3.2 A photograph of one half of the PLT detector installed temporarily on metal rails in a clean room. . . . . 32

3.3 A schematic drawing of one quarter of the PLT detector. The sensors are located in the cassette, and the carriage holds front end electronics and cooling infrastructure. The carriage is inserted into the center of CMS such that the telescopes are 1.75 meters from the interaction point. 4 such quarters were installed in 2015. . . . . 33

3.4 A schematic of the read out chain of the PLT. The optomotherboard, port card and telescopes are inside CMS. The optical connections send data to and from the computer center in a nearby cavern. . . . . 33

3.5 A single PLT sensor is shown, the black square is the silicon semiconducting material which creates an electrical signal when a charged particle passes through. The electrical signal is driven into the read out chip (ROC) by means of a bias field applied to the silicon. The information is read out of the ROC through the ribbon cable at the bottom. . . . . 34

3.6 An artist's rendition of a single PLT telescope in relation to the interaction point of CMS. Shown are two types of signals which the PLT is able to distinguish due to particle track reconstruction from position measurements with pixelated detectors in three consecutive planes. Events from the IP due to proton collisions, and beam halo events. Beam halo consists of charged particles which are carried around the LHC but do not originate from the interaction point and hence do not measure luminosity. The contribution of halo tracks to the triple-coincidence rate must be subtracted offline based on the track reconstruction. . . . . 35

3.7 The measured charge collection for 2 diamond types after subsequent exposures to 24 GeV protons. The scCVD is shown in red, and the pCVD diamonds are shown in blue and green. The scCVD diamonds are offset in the x direction by the noted amount. . . . . 38

3.8 The left plot shows charge collection data from the pixel ROC. The ROC groups events such that adjacent pixels over threshold are measured together in a cluster. If charge is spread over 3 or more neighboring pixels, the event is classified as a $\geq 3$ pixel cluster (red). If only 2 pixels contain charge from the event, it is labeled as a 2 pixel cluster (brown). Single pixel clusters are shown in blue. The black trace is the sum of charge collected from all size clusters. On the right, is a charge signal which is indistinguishable from the noise, to illustrate how charge collection reduction in sensors harms their performance. 39

3.9 The charge collected per cluster integrated over time. The source is opened at the $\sim$125 second mark, charge collection begins around 9k electrons per cluster but quickly drops to a plateau of 7k e. . . . . 40

3.10 Tests done with a 650nm red laser on a diamond sensor. The left plot shows the charge collected from 1 pixel clusters, the peaks and valleys correspond exactly to the laser turning on and off respectively. In the right plot is shown the distribution of single pixel clusters (blue), 2 pixel clusters (brown) and $\geq 3$ pixel clusters (red) this plot shows a large change in single and large cluster population while the laser is turned on. . . . . 41

3.11 A schematic of the TCT setup is shown on the left and a photograph of the setup is on the right. . . . . 42
3.12 The top plot shows an unirradiated diamond's average charge collection pulse at different applied voltages. The bottom plot shows a comparison of an average pulse from 3 diamonds with differing levels of irradiation and applied bias. s130 is unirradiated, s122 has a total dose of $3 * 10^{14} n/cm^2$ and m4 has a total dose of $4 * 10^{14} n/cm^2$. . . . . 43
3.13 A representation of the effect of radiation damage in a scCVD diamond when paired with the observed polarization effect. The black curve represents the expected CCE vs. fluence from a diamond which exhibits no polarization, the red curve represents a fully polarized diamond. In reality the measured CCE will be somewhere between the two curves for a given fluence. . . . . 45

4.1 Examples of Feynman diagrams of SPS color-singlet prompt $J/\psi$ pair production in $pp$ collisions in (a) leading-order (LO), (b) next-to-leading order (NLO), and (c) next-to-next leading order (NNLO), and (d) SPS color-octet prompt $J/\psi$- pair production . . . . . 48
4.2 Production of two quark anti-quark pairs in the double parton scattering process. 49
4.3 The plot shows the $\mu\mu$ invariant mass for passing dimuon candidates in the mass interval allowed by the HLT. . . . . 55
4.4 The probability distribution from the vertex fit to 4-muon candidates is shown in figure (a). Figure (b) shows the majority of events have only one 4-muon candidates and a small fraction contain 2 passing candidates. Only one candidate per event is chosen. . . . . 56
4.5 Plot (a) shows the $|\eta^{\mu}|$ versus $p_{\mathrm{T}}^{\mu}$ distribution for the two decay muons in the reconstructed SPS-NLO MC sample. The muon acceptance used in this analysis is indicated with lines. Plot (b) shows the same for the reconstructed DPS MC sample. . . . . 57

4.6 Plot (a) shows the $J/\psi$ $|y|$ versus $p_{\mathrm{T}}$ for the SPS-NLO MC sample after the muon acceptance criteria are applied. The $J/\psi$ requirements are indicated by the red line in the figure. Plot (b) shows the same for the DPS MC sample. . 58

4.7 Maximum likelihood to the event sample with a greater than 0.5% $4\mu$ vertex probability requirement. The distribution of the fit variables $ct_{xy}$ (a) and $d^{J/\psi}$ (b) in data with the result of the fit superimposed. The solid blue line indicates the total fit, the dashed red line the signal and the dashed green line the background distribution. . . . . 62

4.8 10,000 toy MC of the CTxy and DSig fit were generated and refit. The distribution of NLL is shown in the upper left with a line at the NLL value of the main fit, the pull is shown in the upper right. The lower left plot is the distribution of number of signal in each toy with a line at the main fit value. The distribution of the uncertainty of Nsig is the lower right plot. . . . . 63

4.9 (a): The $\mu\mu$ invariant mass distribution of the high $p_{\mathrm{T}}$ $J/\psi$ candidate with a fit superimposed. The signal (red line) agrees with the total fit; the background contribution is invisible. (b): The $\mu\mu$ invariant mass distribution of the low-$p_T$ $J/\psi$ candidate with the fit to signal (red dashed line) and background (green dashed line) superimposed. . . . . 64

4.10 Maximum likelihood to the event sample with a greater than 10% 4-muon vertex probability requirement. The distribution of the fit variables $ct_{xy}$ (a) and $d^{J/\psi}$ (b) in data with the result of the fit superimposed. The solid blue line indicates the total fit, the dashed red line the signal and the dashed green line the background distribution. . . . . 65

4.11 Signal distribution shown on DPS MC (upper left) SPS-NLO MC (upper right) and signal + background fit shown on the full data sample (lower) . . 67

4.12 The distribution of primary vertices in selected events is shown in the upper left. Variable distributions shown split into low pileup ($PvN < 15$ red) and high pileup ($PvN \geq 15$ blue) events shown in the low $p_{\mathrm{T}}$ $J/\psi$ $\mu\mu$ invariant mass (upper right) the 4-Muon invariant mass (lower left) and the 4-muon $p_{\mathrm{T}}$ (lower right). . . . . 68

4.13 The left column shows the acceptance× efficiency correction in bins of several $J/\psi$ pair production variables obtained with the DPS MC simulation sample, the right column shows the corresponding acceptance correction, only. . . . . 70
4.14 The left column shows the acceptance× efficiency correction in bins of several $J/\psi$ pair production variables obtained with the SPS-NLO MC simulation sample, the right column shows the corresponding acceptance correction, only. 71
4.15 Distributions of 4-muon event variables (a) absolute rapidity, (b) transverse momentum, (c) invariant mass, and (d) absolute difference of the two $J/\psi$ candidate rapidities in data (error bars), with SPS-NLO (green histogram) and DPS (red histogram) simulated sample contributions according to the chisquare fit. The black histogram is the sum of the models. . . . . 73
4.16 The difference of the event efficiency between the T&P tables from data and MC simulation ($\epsilon^{data} - \epsilon^{MC}$), evaluated with the selected data sample (data points) and with the reconstructed MC sample composed of 13% DPS events and 87% SPS-NLO events (blue histogram). . . . . 76
4.17 Ratios of acceptance corrected simulated DPS event distributions in 4-muon variables for different assumption of $J/\psi$ polarization. The two ratios in each plot correspond to $\lambda \pm 0.2$ and have been fit to straight lines that are superimposed to the plot. . . . . 78
4.18 Ratios of acceptance corrected simulated SPS-NLO event distributions in 4-muon variables for different assumption of $J/\psi$ polarization. The two ratios in each plot correspond to $\lambda \pm 0.2$ and have been fit to straight lines that are superimposed to the plot. . . . . 79
4.19 Ratios of acceptance corrected simulated data event distributions in 4-muon variables for different assumption of $J/\psi$ polarization. The two ratios in each plot correspond to $\lambda \pm 0.2$ and have been fit to straight lines that are superimposed to the plot. . . . . 80

4.20 Normalized distributions of the angle $\theta$ between the positive decay muon momentum in the rest frame of the $J/\psi$ and the direction of flight of the $J/\psi$ in the laboratory frame for different assumptions for $\lambda$, within the CMS muon acceptance. The height of the distributions at $\cos\theta = 0$ increases in the order $\lambda = +1, 0, -1$. . . . . 81

4.21 The uncertainties of each bin of the cross section, statistical is shown negative for clarity. (a) transverse momentum, (b) the absolute value of the rapidity, (c) invariant mass, and (d) the absolute difference in rapidity between the two $J/\psi$. . . . . 83

4.22 The uncertainties of each bin of the cross section, statistical is shown negative for clarity. (a) the delta phi between $J/\psi$, (b) the transverse momentum of the higher $p_{\mathrm{T}}$ $J/\psi$, (c) the transverse momentum of the lower $p_{\mathrm{T}}$ $J/\psi$, and (d) the asymmetry between the two $J/\psi$ $p_{\mathrm{T}}$. . . . . 84

4.23 Differential cross section distributions for different 4-muon event variables, (a) transverse momentum, (b) the absolute value of the rapidity, (c) invariant mass, and (d) the absolute difference in rapidity between the two $J/\psi$. The points correspond to data, with statistical error shown as the gray box and the total uncertainty by the error bars. The NLO+DPS model is shown in blue with a model uncertainty of 60% as indicated by the blue boxes. The DPS contribution obtained relative to the cross section in data is shown in red without uncertainty. . . . . 86

4.24 Differential cross section distributions for different 4-muon event variables, (a) the absolute difference in phi between the two $J/\psi$, (b) the transverse momentum of the leading $J/\psi$, (c) the transverse momentum of the subleading $J/\psi$, and (d) the asymmetry in $p_{\mathrm{T}}$ between the two $J/\psi$. The points correspond to data, with statistical error shown as the gray box and the total uncertainty by the error bars. The NLO+DPS model is shown in blue with a model uncertainty of 60% as indicated by the blue boxes. The DPS contribution obtained relative to the cross section in data is shown in red without uncertainty. . . . . 89

4.25 The top left plot shows the recombined data sample with a polynomial fit (line) on top. The same polynomial is shown in the top right plot on top of the low statistics reconstructed DPS MC sample (points with errors). This plot shows that the recombined shape still describes the original DPS MC. The bottom plot shows the exponential decay fit to reconstructed SPS-NLO events. . . . . 96

4.26 The plot on the top shows the data sample fit with the SPS (blue) and DPS (red) shapes. The bottom plot shows the same fit with a log scale. . . . . 97

5.1 Effective cross section values from different experiments at various center of mass energies and for different final states. Values measured by the UA2 experiment [58], AFS experiment [24], ATLAS experiment [1, 4, 6, 2], the LHCb experiment [11, 8, 12], The D0 experiment [15, 16, 18, 13, 14], the CDF experiment [20, 19] and the CMS experiment [82, 51, 56]. The measurement made in this thesis is marked with orange. . . . . 103

# Chapter 1

# Motivation and Physics Background

## 1.1 Background

This section describes the elements of particle physics which are used in the study of the $J/\psi$ pair cross section. It explains The Standard Model, describing in particular the fundamental particles and the fundamental forces in Sec. 1.2.2. $J/\psi$ pairs are frequently produced by the gluon fusion process, which is governed by the strong interaction and Quantum Chromodynamics (QCD) which is described in Sec. 1.3.

Particle physics is the study of the building blocks of matter. Scientists in the field observe particles and their interactions in order to completely describe the natural world. A fundamental description would be comprised of a few building blocks with a limited set of interactions. It would be generalizable to all energy scales and provide accurate descriptions of observed quantities. The Standard Model (SM) of particle physics is a quantum field theory that describes elementary particles and their interactions. It describes the weak, electromagnetic and strong interactions in a consistent theoretical framework. It is based on a limited set of particles (fermions) which interact via bosons. Many measurements up to now have provided supporting evidence for the SM. Recently the Higgs boson was discovered at CERN [47] and represented one of the few remaining unknowns in the SM. The Large Hadron Collider (LHC) located underground in Switzerland and France is responsible for the discovery of the Higgs boson. The LHC was built to collide particles together at very high energies. The resulting production of elementary particles is detected by several large

experiments, all built and maintained by teams of thousands of scientists and engineers from around the globe. The experiments provide data to many different research teams, who hope to observe particle interactions or new generations of elementary particles not predicted by the SM. The LHC is an important tool because it accesses entirely unexplored energy regimes where new physics might be found. The extremely high energy and high collision rate at the LHC opens the possibility to observe more massive particles, and particle decays which were too rare for previous accelerator experiments to detect. In addition, many models beyond the SM (e.g. supersymmetry) predict new particles and forces which are theorized to provide a more complete picture of the natural world. The majority of particles immediately emanating from a collision of protons are extremely short lived. Hence, they must be identified through secondary or tertiary decay products as they cannot be observed directly. The SM predicts decay rates and production cross sections of particles to very high precision. However, the strong force at long interaction distances cannot be calculated as series expansions as is done for weak and electromagnetic interactions, since the importance of higher order contributions does not decrease. Numerical approximations are used to calculate decay rates and cross sections. This requires vast computational calculations which can be improved by measuring hadronic processes at the LHC.

## 1.2 The Standard Model of Particle Physics

### 1.2.1 Elementary Particles

The Standard Model is a quantum field theory (QFT) that describes the particle constituents of the universe and the forces that act between them [108]. The constituent particles are called fermions, they are divided into two subgroups, shown in Fig. 1.1. The quarks, up (u), down (d), charm (c), strange (s), top (t) and bottom (b) and the leptons, electron (e), muon ($\mu$) and tau ($\tau$) where each lepton is associated with a neutrino ($\nu_{e,\mu,\tau}$)[69]. Each fermion has a corresponding anti-fermion denoted by a bar above the name ($\bar{e}$ represents a positron, an anti-electron with charge +1). The interactions, classically thought of in terms of force fields, are described in a quantum field theory where particles called bosons

exchange between the fermions. Bosons may briefly exist as virtual particles below their nominal mass to mediate interactions. The virtual existence at forbidden energy is allowed due to the Heisenberg uncertainty principle $\Delta E * \Delta t \geq 1$ (in natural units), which implies large energy uncertainty at short time scales. The photon ($\gamma$) mediates the electromagnetic (EM) force between charged particles, the infinite range of the EM force is allowed due to the zero mass of the photon. The W+, W- and Z bosons are massive and mediate the short range weak interaction which couples to quarks and leptons. The 8 types of gluons (g) are the massless bosons of the strong force. They act between quarks, and couple to other gluons. These gluon-gluon interactions are responsible for the short range nature of the strong force. All QFTs must obey the principle of gauge invariance and renormalization [69]. Renormalization requires that the theory describes interactions at all energies. Gauge invariance requires that different configurations of the underlying fields result in identical observables, i.e. that the forces apply the same at any point in space and time. The field configurations , such as the choice of a local phase of a particle state, are not observable. Transitions between configurations are allowed and are formulated as gauge transformations. Gauge invariance requires that all particles of the SM are massless. However, experiments observe massive quarks and leptons. Masses are generated via interaction of particles with a field, the so-called Higgs field. The interaction strength is proportional to a particle's mass, and the boson that mediates this interaction is the Higgs boson. This boson was recently discovered at the LHC and its mass is found to be 125 GeV. [47]

This discovery provided a fundamental missing piece in the SM but there are still many questions left to answer. Such as "Why is the Higgs mass 125 GeV/$c^2$?" This mass value, as for any other particle, is not predicted by the SM. It is a parameter of the model that is adjusted to fit measurements. Another question is "Why do the coupling strengths of the strong, weak and electromagnetic forces not unify?" The coupling strengths of the strong, electromagnetic and weak interaction seem to meet at a common length scale called the Grand Unification Theory (GUT) scale. However, the strong force does not intersect the electromagnetic and weak coupling strengths when extrapolated to energies of about a GeV. Furthermore "What is the origin of dark matter and energy which constitute about 95% of the universe?" While there is no dark matter candidate particle in the SM, there are several

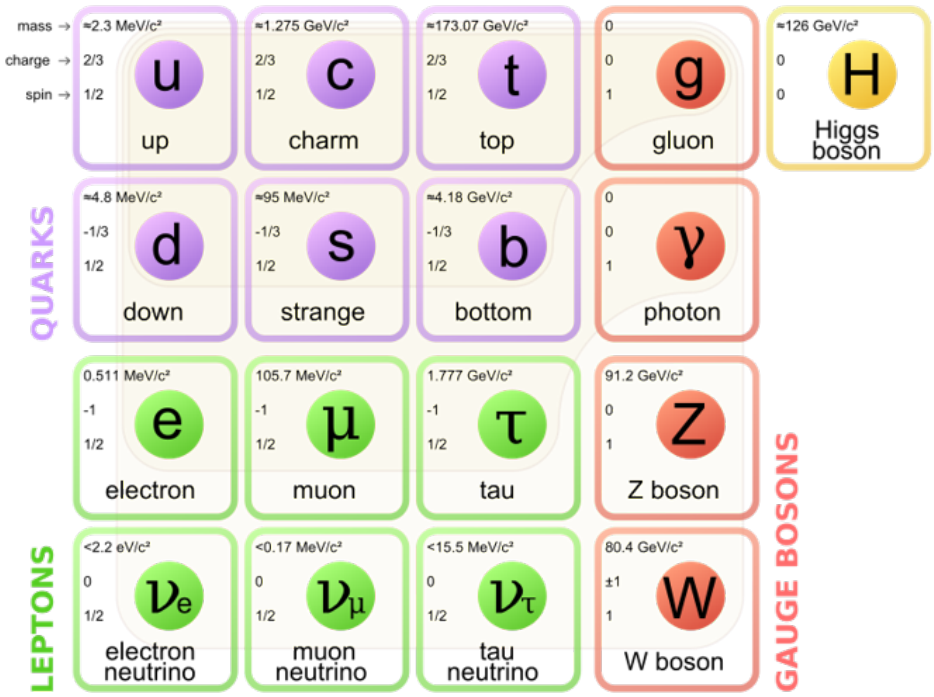



**Figure 1.1:** The particles of the Standard Model (SM) categorized into quarks, leptons and bosons

theories that expand the SM. One such popular theory is the minimally supersymmetric standard model (MSSM) [63] which predicts additional particles that are partners of the existing quarks and leptons. It also predicts several additional Higgs bosons, including lighter ones. The lightest supersymmetric neutrino type particle is potentially a candidate for dark matter. New particles and new forces are searched for at the LHC to answer such questions.

### 1.2.2 The Fundamental Forces

The strong force binds quarks together to form baryons and mesons. It is also responsible for binding protons and neutrons into nuclei. A proton is made of 3 bound quarks ($uud$). The existence of two $u$ quarks in the same location, with the same quantum numbers is forbidden by the Pauli Exclusion Principle, so a quantum number called color charge is introduced [68]. Color has 6 possible values, red, green, blue, and each color has a corresponding anti-color. Quarks have both an electric charge and a color charge simultaneously, the strong interaction only applies to particles with color charge. The constituents of mesons and

baryons combine to form a color neutral object, i.e. the $c\bar{c}$ in a $J/\psi$ could be $red\ \ anti-red$ which is color neutral. The QFT used to describe the strong interaction is called Quantum Chromodynamics or QCD. The strong interaction depends on a coupling constant called $\alpha_S$. $\alpha_S$ is a so called running coupling constant because the value depends on the energy of the interacting particles. As the energy of interaction increases beyond a few hundred MeV the strong coupling constant becomes sufficiently small so that a calculation in terms of an expansion in orders $\alpha_S$ converges rapidly enough. The strong interaction becomes weaker at very short distances, corresponding to higher energies (less than 1fm). This energy scale is called the QCD scale ($\Gamma_{QCD}$). The constituents of high energy hadrons, such as the protons accelerated inside the LHC, can then be treated as quasi-free particles within that size, this dependence is called asymptotic freedom. High energy hadrons can be modeled as collections of several different partons: gluons, valence quarks and sea quarks. The valence quarks are the 3(2) quarks needed to form the baryon(meson). The gluons bind these valence quarks but can also split to form virtual $q\bar{q}$ pairs called sea quarks and additional gluons. The sea quarks can contribute to interactions in pp collisions. However, they do not determine the quantum numbers of the hadron. As the energy increases, sea quarks and gluons become more and more dominant contributors to pp interactions. A representation of a high energy proton is shown in Fig. 1.2 including the sea quarks and gluons alongside the valence quarks. At energies lower than $\Gamma_{QCD}$ proton interaction can be formulated using valence quarks only.

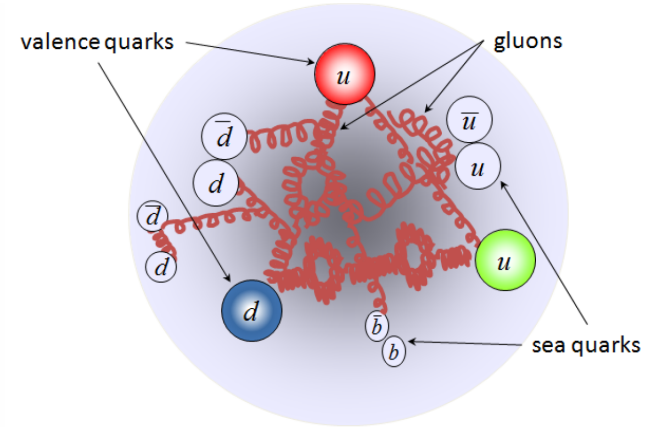



**Figure 1.2:** A rendition of a high energy proton, where sea quarks and gluons become the more dominant producers of pp collisions

**Table 1.1:** The fundamental interactions described by the standard model

| Interaction | Boson | Effective Range | Process in Nature |
|---|---|---|---|
| Strong | gluon | $10^{-15}/m$ | Binds hadrons and nuclei |
| Electromagnetic | photon | $\infty$ | Binds atoms and molecules |
| Weak | Z,W boson | $< 10^{-17}/m$ | Enables $\beta$ decay |

If two quarks are separated, the potential energy between them increases linearly until it exceeds the energy needed to create an additional $q\bar{q}$ pair. This interaction follows energy, charge and color charge conservation and becomes common in very high energy collisions where lone quarks are ejected from a high energy collision. The process of creating $q\bar{q}$ pairs to retain color neutrality is known as hadronization.

The electromagnetic (EM) interaction acts between electrically charged particles via photon exchange. Electrons are bound to protons, and atoms bound into molecules by this force. The photon is a massless particle, and allows EM interactions to occur over infinite range, weakening with distance $r$ as $1/r^2$. At length scales longer than $\sim 1fm$ the EM interaction is the only relevant contributor to particle interactions. Quantum Electrodynamics (QED), the QFT describing electromagnetism, predicts the interaction strength to high precision, on the order ($O'10^{-8}$) [88]. The coupling constant, called the fine structure constant or $\alpha$ changes with the energy of the interaction.

The weak force enables the nuclear $\beta$ decay reaction. It is the shortest range force among the three, and is described using Quantum Flavordynamics (QFD). The weak and EM forces were unified under the overarching Electroweak Theory (EWT) which describes them as consequences of the same force [93, 66, 108]. The very massive $W^{\pm}$ and Z bosons mediate the weak force, which restricts the range. The mass of the $W^{\pm}$ boson is $80.4\,\mathrm{GeV}/c^2$ and the Z is $91.2\,\mathrm{GeV}/c^2$ shown in Fig. 1.1. The weak interaction is unique in that it is the only fundamental force which can violate parity (P) and charge parity (CP) symmetry.

SM interactions require conservation of the fundamental properties, charge, energy, momentum, and color charge, and are illustrated and calculated with Feynman diagrams. An example is shown in Fig. 1.3. Feynman diagrams can be interpreted with any one or two particles as the initial state and the remainder as the final state. Any interaction which

maintains the conservation laws is possible. The interactions shown in Fig. 1.3 are called leading order diagrams. More complex interactions are possible, these are referred to as higher order interactions. A meson decay through the strong interaction, could be described by the left most diagram in Fig. 1.3, with the annihilation of the $q\bar{q}$ creating a gluon. The interaction would not stop because a lone gluon is not color neutral, so the gluon would proceed to splits into a new $q\bar{q}$ state, creating a new meson. Alternatively, the meson could decay to a photon through the EM interaction, or a Z boson by way of the weak interaction. More complex structures, where particle pairs are emitted and annihilated within a single

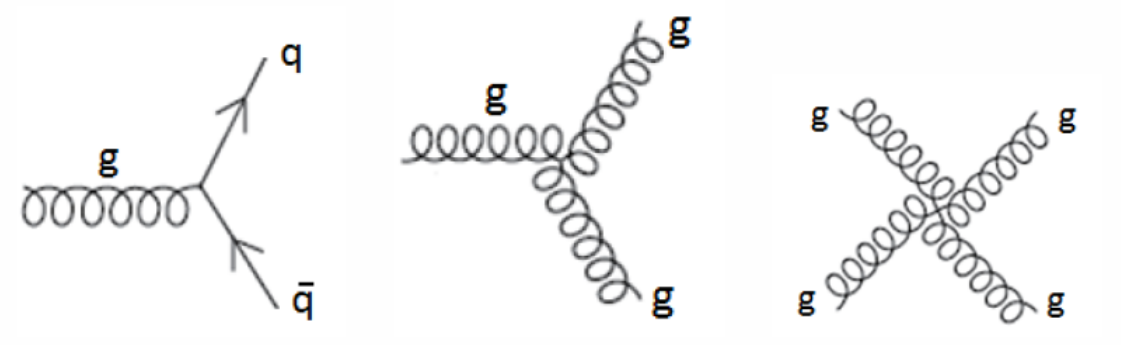



**Figure 1.3:** The left most interaction can describe a gluon splitting into a quark-antiquark pair, a quark-antiquark annihilation forming a gluon, or a quark emitting or absorbing a gluon. The center diagram shows an excited gluon emitting another gluon, or two gluons fusing into one. The right diagram shows a pair of gluons interacting to exchange quantum numbers.

process are called loops. These loop diagrams add factors of the interaction coupling constant and play an increasingly significant role as the interaction energy increases.

## 1.3 Quantum Chromodynamics at the LHC

### 1.3.1 High Energy Interactions

Interactions in the LHC between proton constituents may involve varying amounts of energy depending on how central a collision is. This can be quantified by the amount of energy of the the products of the interaction. When final states receive tens of GeV or more, they were the result of a so called hard scattering processes. Hard scattering processes produce

final states strongly transverse to the beam direction. Soft scattering interactions are much more common than hard scattering and produce final state particles with energy on the order of a few MeV. Many of the products of soft scattering continue to travel along the beam direction with minimal transverse momentum. Double $J/\psi$ final states are only created when the interaction involves a minimum of $2 * Mass^{J/\psi}$ or 6.2 GeV. The scattering of hadrons can be modeled in 3 steps that factorize. Each hadron is described as a distribution of partons, each parton inside a hadron can be considered an unbound particle, and every parton-parton interaction between protons has a chance to produce any end-state hadron. This concept translates into a cross section as shown in Eqn. 1.1:

$$\frac{d\sigma}{dX} = \sum_{j,k} \int_{\hat{X}} f_j(x_i) f_k(x_2) \frac{d\hat{\sigma}_{jk}}{d\hat{X}} F(\hat{X} \to X) \tag{1.1}$$

where:

- $X$ is a hadronic final state kinematic variable,
- $i$ and $j$ are the parton types present in the interacting hadron,
- the function $f_j(x)$ is the parton distribution function (PDF) representing the number density of parton type $j$ with momentum fraction $x$,
- $F(\hat{X} \to X)$ is a function that represents the probability of transition from partonic state $\widehat{X}$ into final hadronic state $X$.

Breaking the process into these parts facilitates combining different theoretical models which describe each piece individually. PDFs can be developed and used independently from hadronization models and different theories can be explored with custom calculations for any or all of the factors. These models are primarily used to predict particle production and compare with data.

Particle production is measured in several ways, usually with respect to a kinematic variable which is measured by the detector. Some common variables are enumerated here and will be referenced throughout the thesis.

- Transverse momentum ($p_{\mathrm{T}}$) is the transverse component of the momentum of a final state particle. Transverse is defined in reference to the incoming and outgoing proton beams at the LHC.

- Rapidity ($y$) is defined as

$$y = \frac{1}{2} ln \left( \frac{E + p_L}{E - p_L} \right) \tag{1.2}$$

  where $p_L$ is the momentum of the final state particle along the beam direction, and $E$ is the particle energy.

- Pseudorapidity ($\eta$) describes the angle relative to the proton beam and is defined as

$$\eta = -ln(tan \left( \frac{\theta}{2} \right)) \tag{1.3}$$

  where $\theta$ is the angle between the proton beam the particle momentum. If the particle is relativistic, the rapidity will be similar to the pseudorapidity.

The interactions between two protons in a collision at the LHC can involve one or more of the constituent partons. When an interaction only involves a single parton from each proton, it is referred to as a single parton scattering (SPS) event. Similarly, when 2 partons contribute to the interaction it is called double parton scattering (DPS). The double $J/\psi$ final state can be produced through both of these scattering types and a primary goal of this thesis is to discriminate the type of interaction responsible for production of the $J/\psi$ pairs and measure the relative contribution of production modes. The frequency of DPS production is a measurable quantity and it is theorized to be independent of process and collision energy, therefore a measurement of this so called effective cross section can be made and compared to previous experiments.

### 1.3.2 Color Singlet and Color Octet States

Observable hadronic particles must exist as color neutral objects, which requires mesons to contain color-anticolor pairs of quarks. The three color charges are denoted red (r), green (g) and blue (b) and their corresponding anticolors $\bar{r}, \bar{g}$, and $\bar{b}$. The color charge content of

a meson cannot be directly measured, so it is represented as a superposition of all possible states, $(r\bar{r} + g\bar{g} + b\bar{b})/\sqrt{3}$. This is known as a color singlet (CS) state. Alternatively, gluons exist in a color octet state (CO) described by the color superpositions listed in Eqn. 1.4.

$$\begin{aligned} (r\bar{b} + b\bar{r})/\sqrt{2} \qquad & (r\bar{g} + g\bar{r})/\sqrt{2} \\ (g\bar{b} + b\bar{g})/\sqrt{2} \qquad & (r\bar{r} + b\bar{b})/\sqrt{2} \\ -i(r\bar{b} + b\bar{r})/\sqrt{2} \qquad & -i(r\bar{g} + g\bar{r})/\sqrt{2} \\ -i(g\bar{b} + b\bar{g})/\sqrt{2} \qquad & (r\bar{r} + b\bar{b} - 2g\bar{g})/\sqrt{6} \end{aligned} \tag{1.4}$$

$J/\psi$ can be produced in a color octet state, the state decays to a color singlet meson by emitting a gluon. This additional gluon emission modifies the kinematics of the final state muons. Color octet production becomes significant in higher rapidity and $p_{\mathrm{T}}$ measurements of $J/\psi$ cross sections.

# Chapter 2

# Experimental Setup

## 2.1 The Large Hadron Collider

The LHC is the highest energy particle accelerator in operation. It is located at the European particle physics laboratory CERN near Geneva, Switzerland [41]. The collider and detectors are located underground as shown in Fig. 2.1. The LHC is designed to produce particle

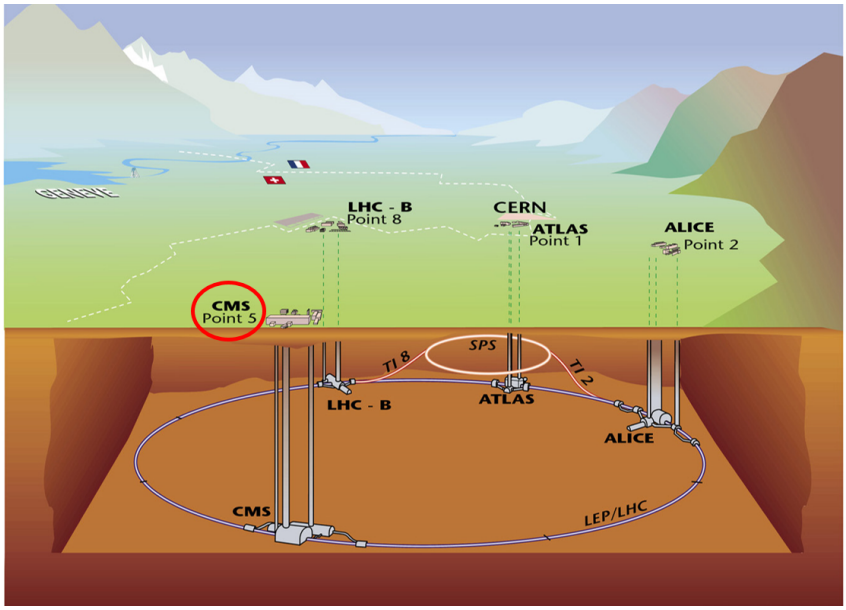



**Figure 2.1:** A schematic of the LHC accelerator complex. The 4 major experiments and the primary CERN site are labeled, with the Compact Muon Solenoid detector circled in red.

interactions at energies significantly higher than previous experiments. These very high energies are needed in order to produce heavy states like the Higgs, and to access even higher mass states. In addition, the low cross sections of interesting processes require high beam intensities and collision rates to make significant measurements. The LHC is a proton storage ring which uses 2 beam pipes surrounded by superconducting magnets to accelerate counter-rotating proton beams. These beams are fed into the LHC by smaller pre-accelerators in small groups of protons, called bunches. Each bunch can contain more than $10^{11}$ protons, and a complete LHC fill contains 2808 bunches. A schematic of all accelerators in the LHC complex is shown in Fig. 2.2.

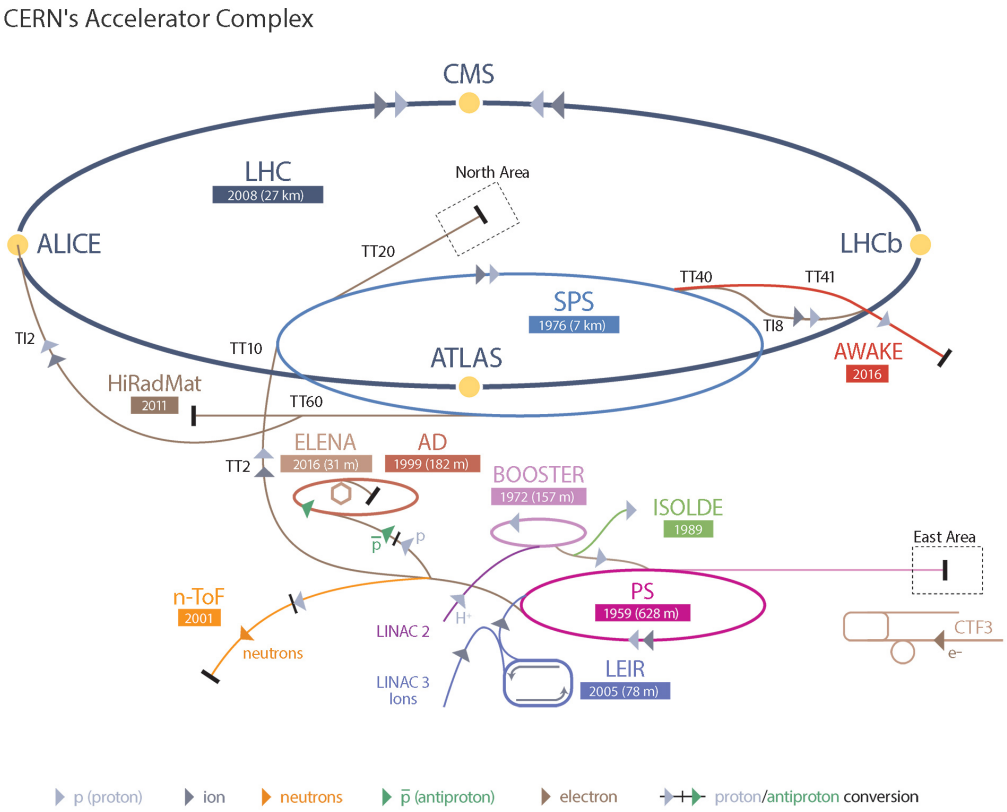



**Figure 2.2:** A schematic of all the accelerator facilities at CERN. The arrows show the direction of particle beams in each accelerator, the gray arrows representing the proton beams.

Bunches are spaced by 25 ns. Groups of filled bunches are separated by specific numbers of un-filled bunches to allow for kicker magnet ramp-up which redirects the bunches from

the smaller accelerators, the Proton Synchrotron (PS) and the Super Proton Synchrotron (SPS), into the LHC. The largest such time interval of $3\mu s$ is called the abort gap. This time is needed to ramp an abort kicker magnet which redirects the LHC beams safely toward a beam dump area in case of unstable beam conditions or an emergency. 72 bunches are grouped into a bunch train and are accelerated in the PS and injected into to the SPS. The SPS gathers 3 or 4 trains from the PS, further accelerates the protons and transfers the batches into the LHC. The total fill pattern of the LHC beams can be seen in Fig. 2.3, blue and red boxes correspond to bunch trains, with the red boxes highlighting the cycle of 4 train batches. Collisions occur at 4 interaction points located around the LHC. The beams are

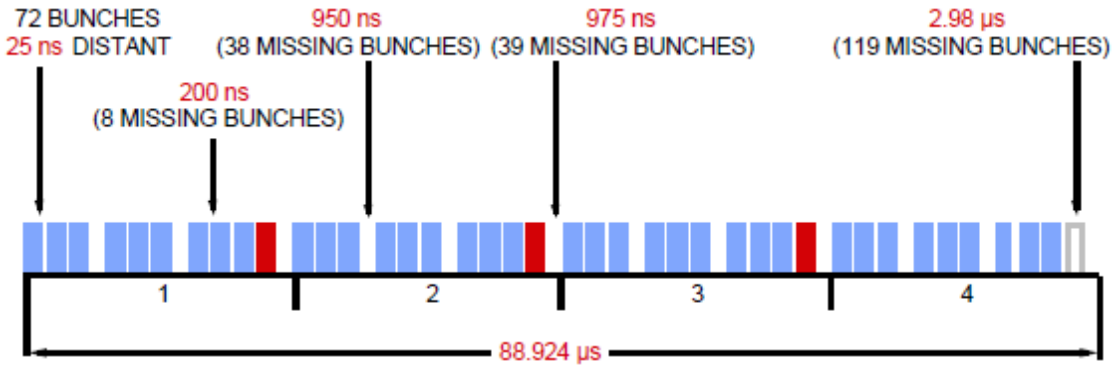



**Figure 2.3:** A schematic of a full bunch pattern in the LHC, showing the various gaps to accommodate kicker magnets. 72 bunch groups, called batches are accelerated in the PS and delivered to the SPS. The SPS then further accelerates the protons and transfers groups of 3 or 4 batches into the LHC.

crossed at each of the interaction points allowing for protons from opposite beams to collide. Protons may collide centrally with most of the collision energy converted into particle that can also acquire substantial transverse momentum in contrast to peripheral collisions where the particles obtain very small transverse momenta. The majority of collisions is peripheral. During the years 2010-2011, collisions occurred at a center of mass (cm) energy of 7 TeV (3.5 TeV per beam). In 2012 the cm energy was increased to 8 TeV and in 2015 the collider achieved energies of 13 TeV.

The instantaneous luminosity $\mathcal{L}$ is defined by parameters of the colliding proton beams:

$$\mathcal{L} = \frac{f(N_1 N_2 n_b)}{4\pi\sigma_x\sigma_y} \tag{2.1}$$

where $N_1$ and $N_2$ are the number of colliding protons in each bunch for beam 1 and beam 2 (more than $10^{11}$ for the LHC), $n_b$ is the number of colliding bunches in each beam (2808), and $f$ is the bunch crossing frequency ($\frac{1}{25ns}$). The $\sigma_{x,y}$ are the transverse sizes of the beam in x and y, assuming a Gaussian profile along those directions. When two particles collide, the effective area within which they must meet in order to interact is called the cross section. Cross sections are defined transverse to the relative motion of the interacting particles and are measured in the unit of area, called the barn ($b = 10^{-24} cm^2$). The rate (R) at which a particular particle process occurs e.g. the production of Higgs, is directly proportional to the Luminosity $\mathcal{L}$ and the cross section ($\sigma$) for a particular particle reaction. $R = \mathcal{L} * \sigma$. The total cross section of production in the LHC at 8 TeV cm energy is about 100 mb as shown in Fig. 2.4. In comparison, the production cross section of the Higgs boson is about 20 pb at that energy. An instantaneous luminosity of $1 Hz/$ nb yields a total rate of particle production of 100 mb $* 1 Hz/$ nb $= 100 MHz$ and a Higgs production rate of $\sim 0.02 Hz$. The peak instantaneous luminosity achieved in 2012 was $7.7 * 10^{33} cm^{-2} s^{-1}$ or $7.7 Hz/$ nb. This analysis uses the 23.3 $\text{fb}^{-1}$ of data delivered to CMS in 2012.

Rare processes such as Higgs production must therefore be distinguished from the much more frequent hadronic production via a distinct final state. Detectors use unique topologies, for example $Higgs \to \gamma\gamma$, a channel with two high energy photons in the final state moving back-to-back, can be detected in a segmented electromagnetic calorimeter. The decay $Higgs \to ZZ \to 4\mu$ is another channel that is distinct as the muons penetrate many layers of detector material and provide a well constrained momentum measurement which allows for precise reconstruction of the Higgs invariant mass. Analogously, a $J/\psi \to \mu\mu$ decay is detected and identified via its final state muons. More details about the reconstruction of this final state are presented in Chapter 2.2. The detector utilizes fast event filters (triggers) based on the topology and kinematics of interesting reactions to enhance their occurrence in the stored data events. Triggers are discussed in more detail in Sec. 2.3.

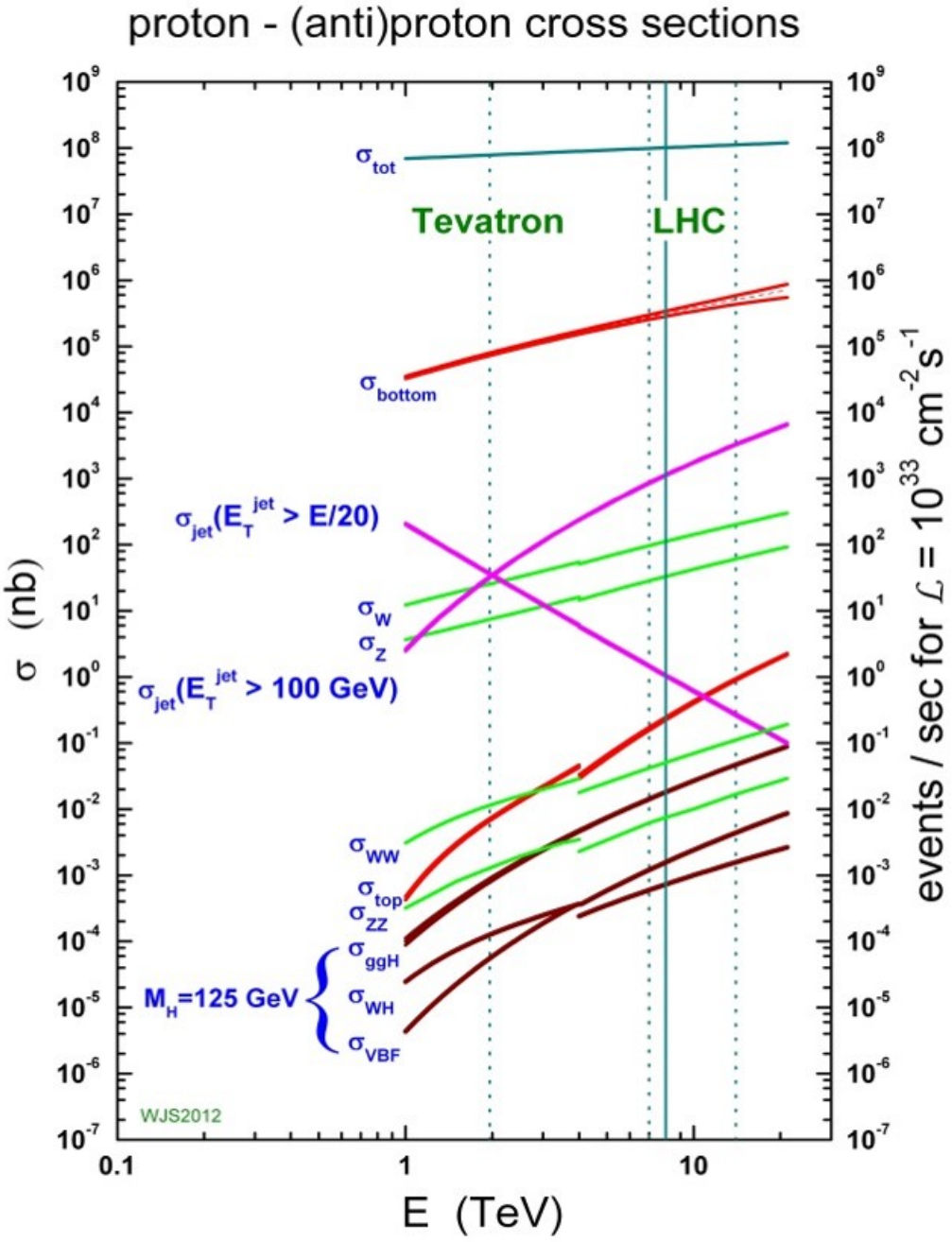



**Figure 2.4:** Production rates, corresponding to cross sections are shown for various center of mass energies. In the LHC regime, the total production $\sigma_{tot}$ can be seen to be 100 mb, with the highest Higgs production mode $\sigma_{ggH} =\sim 20$ pb, many orders of magnitude lower.

## 2.2 The Compact Muon Solenoid

The Compact Muon Solenoid (CMS)[46] detector shown in Fig. 2.5 is one of the 2 multi-purpose particle detectors at the LHC. The other is the ATLAS experiment. CMS is located at one of the 4 interaction points located around the LHC. The proton collisions occur at the center of the cylindrical detector. CMS has 5 major sub-detector components arranged symmetrically around the beam pipe. Listed from the outside in, they are the muon stations, hadronic calorimeter (HCAL), electromagnetic calorimeter (ECAL), silicon strip tracker and the silicon pixel detector. The namesake solenoidal magnet is located between the HCAL and the muon chambers. A dedicated luminosity monitoring detector, called the Pixel Luminosity Telescope (PLT) is located outside the pixel detector. It measures bunch by bunch luminosity delivered to the CMS detector, more details on this system are in Sec. 3.2.

CMS uses its large superconducting solenoid magnet, capable of producing a 3.8 Tesla (T) magnetic field at the center of the detector, to facilitate momentum measurements of charged particles. Since the majority of production occurs in the very forward direction, the solenoid also serves to bend low $p_{\mathrm{T}}$) particles toward the beam pipe, keeping them from impacting the sensitive material and isolating the high $p_{\mathrm{T}}$ tracks associated with central collisions.

A particle with velocity $\vec{v}$ and charge $q$ which moves through a uniform magnetic field $\vec{B}$ experiences a force $\vec{F}$ called the Lorentz force. This force acts according to the "right hand rule" perpendicular to both the direction of $\vec{v}$ and $\vec{B}$. The resulting particle path in a constant field is a helix. The axis of the helix is parallel to the direction of the magnetic field.

In the plane transverse to the particle direction, it follows a circular path with radius $r$ given by

$$r = 0.3 * \frac{p}{q \cdot B} \tag{2.2}$$

where $p$ is the particle momentum. For a high momentum particle only a segment of a circle is detected, and the transverse momentum is obtained as,

$$p_{\mathrm{T}} = \frac{qL^2B}{8s} \tag{2.3}$$

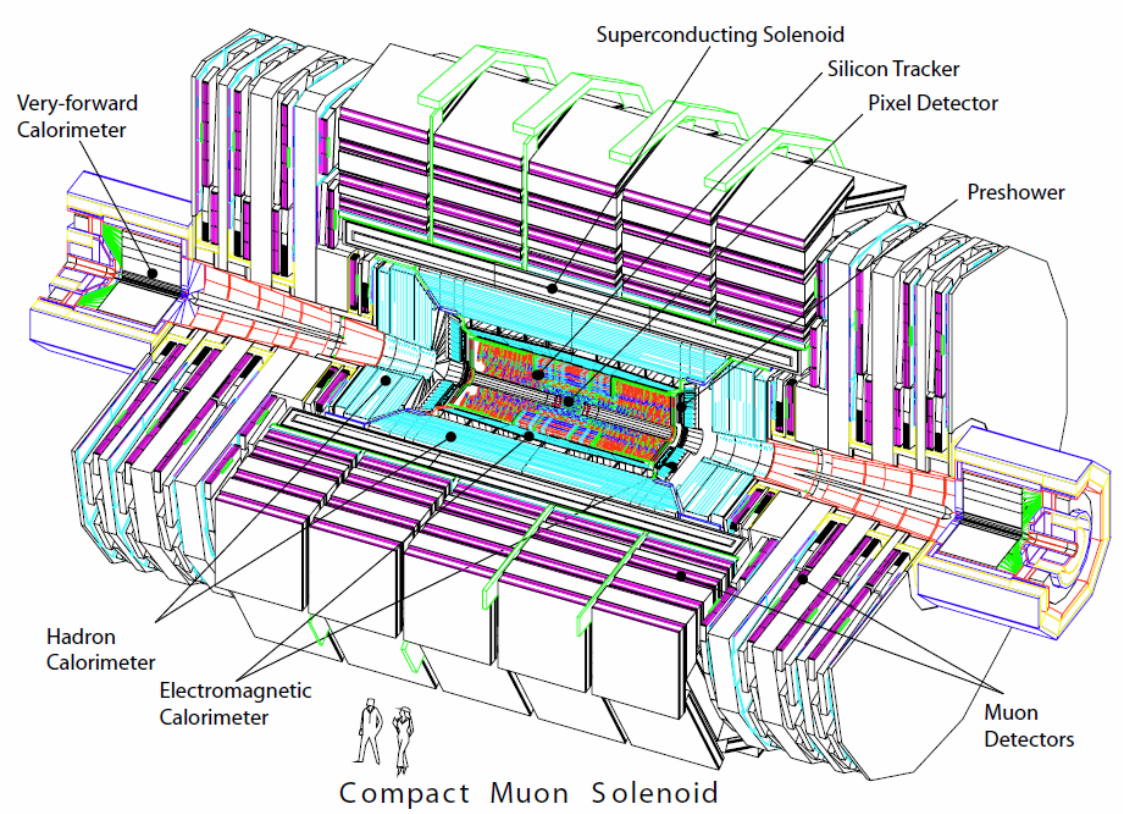



**Figure 2.5:** A cutaway of the CMS detector, with persons shown for scale comparison. The outermost layers are muon detectors placed between slabs of iron absorbers. The iron layers also function as return yoke for the magnetic field. From outside inwards the muon detectors are followed by the superconducting solenoid,the hadronic calorimeter, the electromagnetic calorimeter, the silicon strip tracker, and the innermost 3 layers are the silicon pixel detector. The beam pipe enters from each end of CMS and collisions take place in the center of the detector.

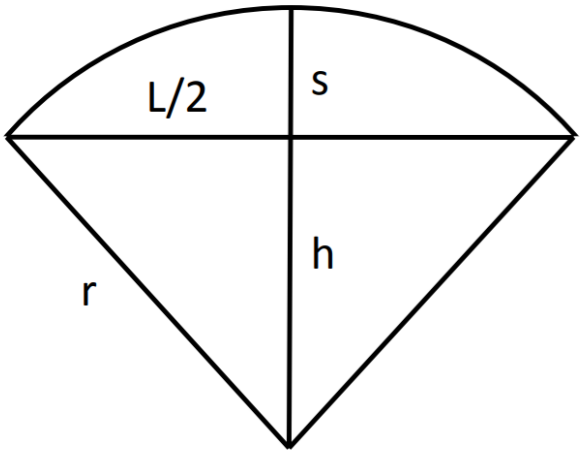



**Figure 2.6:** A diagram of the sagitta $s$ for a particle passing through a region of length $L$ with a constant magnetic field.

where $s$ is the sagitta of the curved path, $L$ is the span of the segment, $q$ is the particle charge and $B$ is the magnetic field strength. The magnitude of the total momentum is given as

$$p = p_{\mathrm{T}}\sqrt{1 + tan^2\lambda} \tag{2.4}$$

where $\lambda$ is the polar angle of the particle path measured from the direction of the proton beam.

The CMS detector is conceptually divided into two regions, the central region where $\eta <\sim 1$, also called the barrel of the detector, and the endcap region $\eta >\sim 1.2$. In the transition region between these two, particles traverse both barrel and endcap detectors as shown in Fig. 2.10. The coordinate system of the detector is defined in Cartesian coordinates with the origin at the center of CMS and z-axis pointing along the direction of the counter-clockwise proton beam. The x-axis points toward the center of the LHC and the y-axis points up, toward the surface. In cylindrical coordinates, the z-axis is defined the same way as in Cartesian, with r measured from the z-axis and $\phi$ measures the angle with respect to the positive Cartesian x-axis.

### 2.2.1 The Silicon Pixel Detector and Silicon Strip Tracker

Located at the center of CMS, the pixel detector is made of silicon semiconductor sensors which are connected to pixelated readout chips (ROCs). They are organized in 3 concentric layers in the barrel region, and 2 disks with fanned blades on each endcap. There are $47,923,200$ pixels in the barrel and $17,971,200$ in the endcap detectors[52].

The silicon strip detector surrounds the pixel detector and also makes use of silicon semiconductor sensors. Together, the pixel detector and silicon strip tracker contain 10 layers of sensitive material to detect charged particle tracks with enough granularity to distinguish nearby particles in the dense hadronic environment created by the pp collisions. During the 2010 - 2012 running period, called run 1, the innermost layer of the CMS pixel detector recorded $9.3*10^{13} tracks/cm^2$ [106]. This represents a hostile radiation environment which can damage sensitive detector material and electronics. The silicon system maintained function throughout the 3 years of data taking, but risks damage moving into the future with plans for higher energy and instantaneous luminosity. A diagram of the pixel detector's barrel layers and endcap disks is shown in Fig. 2.7.

The silicon semiconductor material is electrically connected to the pixel ROCs with bump bonds consisting of indium bumps. The pixels are rectangular and measure $150\mu m$ by $100\mu m$. The short side is parallel to the magnetic field and the long side is in the direction of the Lorentz force which smears moving charges over multiple pixels. A cutaway diagram of a pixel chip connected to a silicon plane can be seen in Fig. 2.8. The silicon sensor combines a p-type semiconductor with an n-type to create a p-n junction. Excess electrons from the n-type material diffuse into the p-type area creating an intrinsic electric field which depletes the area of free charge. This so called depletion zone remains about $10\mu m$ wide with no external inputs because, the electric field counteracts further charge diffusion causing an equilibrium. The depletion zone can be expanded to the full width of the sensor by applying an external electric field. When a charged particle traverses the silicon, energy is deposited in the material and produces electron/hole (positively charged vacancies) pairs. An average of 3.6 electron volts (eV) is required to produce each pair. In a 300 $\mu m$ thick silicon sensor, a minimum ionizing particle (MIP) deposits about 120 keV of energy resulting in about 33k

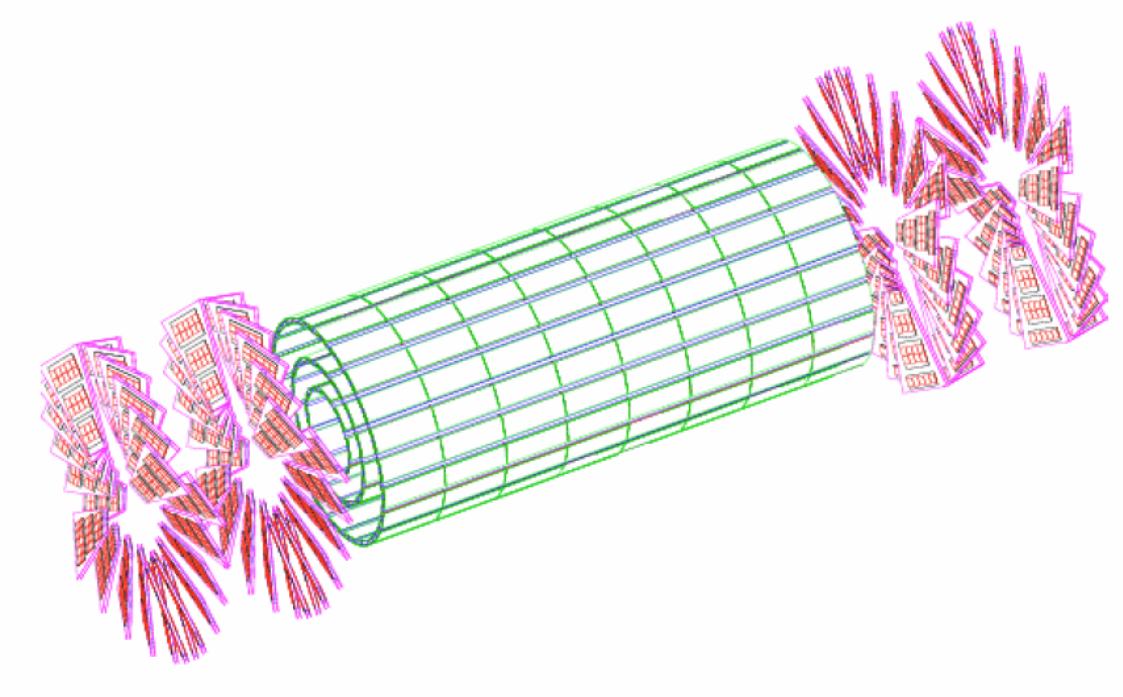


**Figure 2.7:** A diagram of the silicon pixel detector's barrel layers (green) and endcap disks (red).

free electrons. The electrons and their corresponding holes move to opposite sides of the depletion zone. A schematic of this process is shown in Fig. 2.9. As electrons drift toward the bump bonded electrode they induce a mirror charge signal. The signal is integrated over a certain time into a capacitor and then stored until it is drained either by demand from a valid trigger or after some time to allow further charge deposits. The amount of charge collected, and the address of the pixel in which it was collected is stored in a data buffer and sent to the data acquisition system upon request.

### 2.2.2 The Muon Detection System

For the analysis presented in this thesis, the muon detectors are crucial to trigger and identify muons from collisions and obtain high precision muon momentum measurements.

The primary muon detection hardware is collectively referred to as the muon chambers. The muon chambers are designed to measure $J/\psi$, Z, Higgs and other particle decays to muon final states, search for new states which may decay to muons and identify hadronic

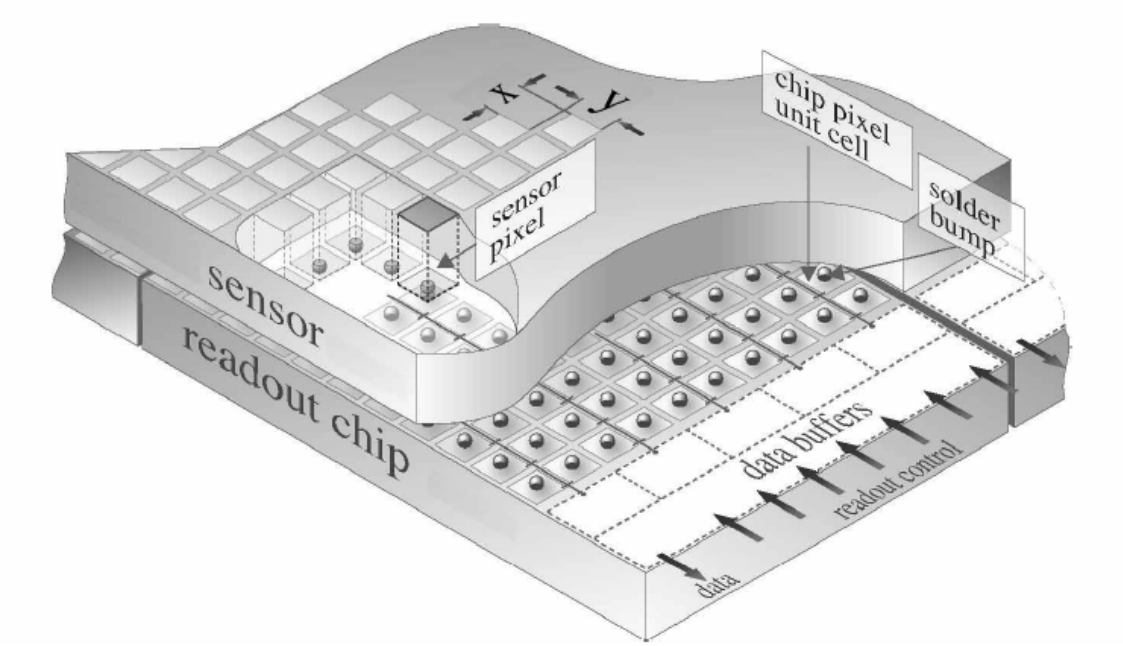



**Figure 2.8:** Shown is a cutaway diagram of the pixelated ROCs bump bonded to a silicon sensor.

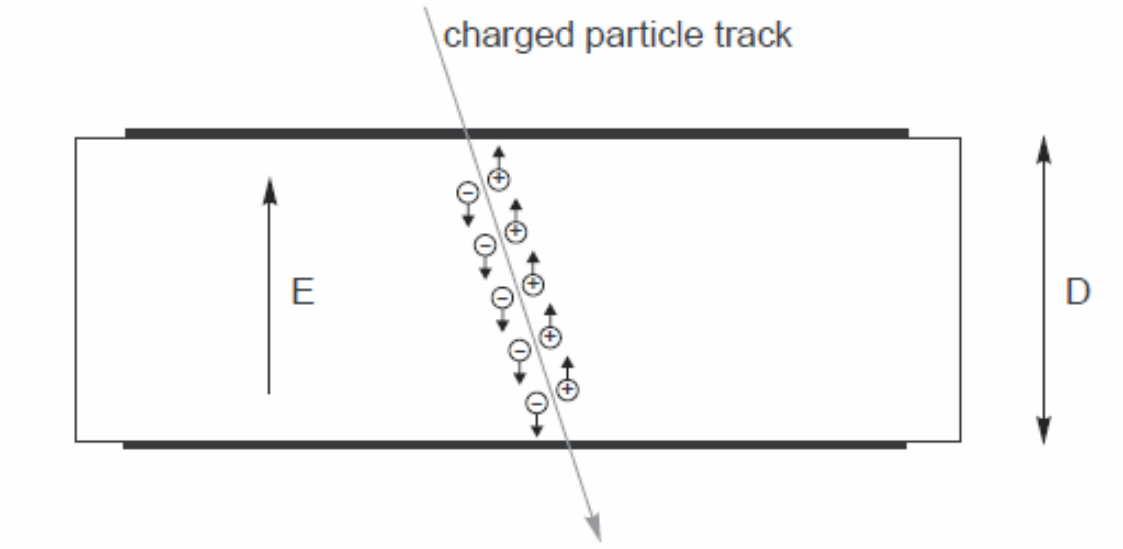



**Figure 2.9:** The mechanism of charge creation in a material is illustrated. An incident particle deposits energy in the form of electron/hole pairs which are drifted to the edges of the material by means of an applied electric field. The thickness D is about 300 $\mu m$ for CMS silicon detectors, and the typical electric field is $0.1 V/\mu m$

jets from b-quark decays (since the $b \rightarrow \mu$ decay is an essential part of Higgs studies and supersymmetry searches). These detectors take advantage of the unique properties of muons:

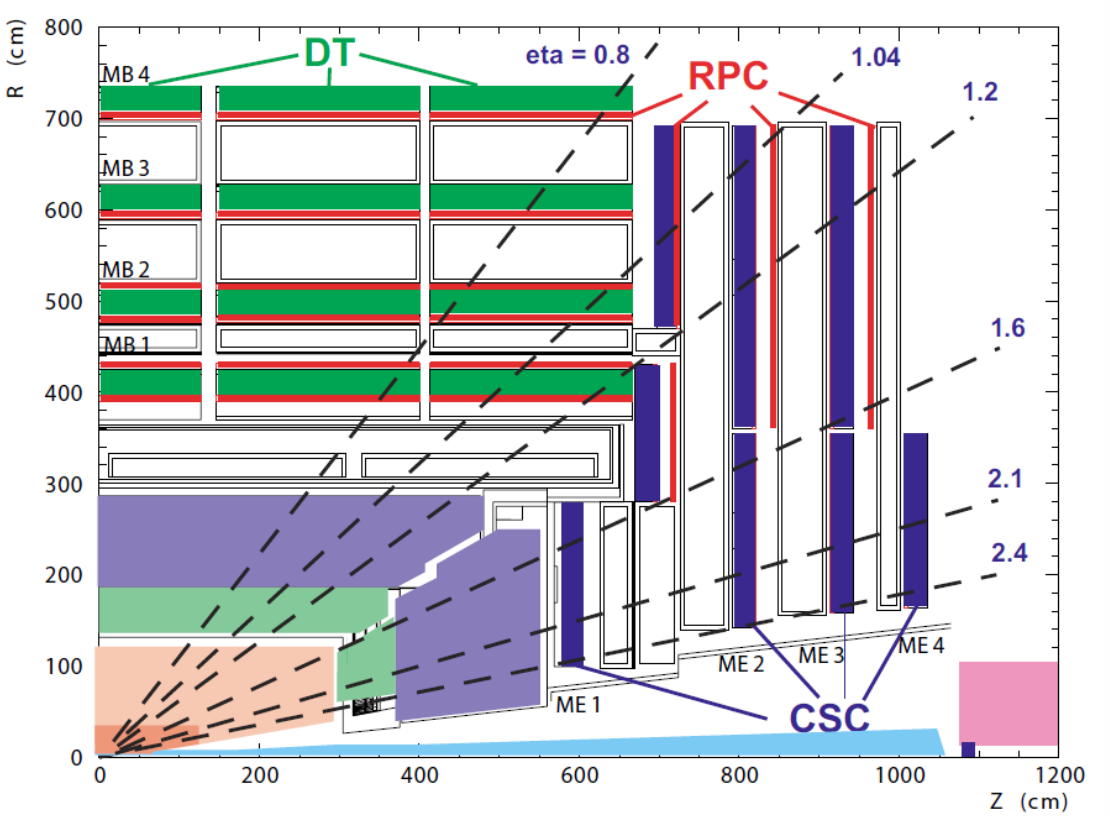



**Figure 2.10:** A single quarter of the CMS detector, the interaction point is located at the bottom left corner of the diagram. The components of the muon detection chambers are labeled, and the value of $\eta$ for various angles ($\lambda$) with respect to the z axis is shown.

- muons have higher mass than electrons and are less strongly deflected by EM fields,
- they do not interact with gluons and therefore little nuclear scattering in the dense calorimeter occurs,
- muons are less likely to emit bremsstrahlung radiation than electrons which causes energy loss,
- and have a relatively long lifetime ($2.2\mu s$ in their rest frame).

These properties allow muons to penetrate more layers of detecting material then electrons with the same energy. The muon detectors are placed the furthest from the interaction point,

requiring particles to traverse the dense calorimeter and solenoid material before reaching the muon chambers. The muon chambers are comprised of three types of detector technologies which complement each other. An image of one quarter of the CMS is shown in Fig. 2.10, with the muon chamber technologies labeled. Aluminum drift tubes (DT) are found in the central region, cathode strip chambers (CSC) populate the end-cap regions, and Resistive plate chambers (RPC) are found throughout the muon stations.

A drift tube is a cathode tube filled with a mixture of $Ar$ & $CO_2$ gas, it contains an anode wire running along the long axis of the tube. A charged particle passing through the DT will ionize atoms in the gas and liberated electrons will move toward the anode wire. The movement of charge will liberate further charge, causing a charge avalanche. The charge avalanche induces a current in the wire. Current pulses are measured with respect to the known electron drift time to reconstruct the position of the charged track within the DT. The DT system includes 3 super layers (SL), each comprised of 4 radial layers of DTs. The two outer SLs are arranged to measure transverse plane coordinates $(r-\phi)$, while the inner layer measures the coordinate in the $z$-direction. Chambers are clustered into stations, with each station containing up to eight chambers (in two groups of four). The measurements in the transverse and $z$-coordinate are combined to build three dimensional track segments. The DT chambers are staggered in such a way that a high $p_{\mathrm{T}}$ track must traverse at least 3 of the 4 stations. DTs are installed in an alternating fashion with RPCs so that high $p_{\mathrm{T}}$ tracks can cross a up to 6 RPC and 4 DT chambers. This results in an expected $z$-position resolution from $100\mu m$ to $250\mu m$ depending on the number of points found in the measurement of the track. The transverse plane resolution is expected to be about $0.5mrad$.

The Cathode Strip Chamber (CSC) is a multi-wire proportional chamber shaped like a trapezoid and filled with a gas mixture containing $CO_2, Ar,$ & $CF_4$. The CSCs are located in the endcap region because they are less sensitive to large non-uniform magnetic fields than the DTs. Each chamber has planes of radial cathode strips and anode wires rotated at 90 degrees to each other. The gas ionization due to a charged particle creates an electron avalanche which is measured in the anode wires, while the image charge is measured in the cathode strips. The wires are spaced by $2.5 - 3.16mm$ allowing the CSC a fast response to

incident charge ($\sim 4.5ns$). The expected spatial resolution of CSC measurements is $\sim 200\mu m$ in the $z$-direction and $\sim 10mrad$ in the transverse plane.

Resistive Plate Chambers (RPC) are parallel plate detectors filled with a mixture of Freon and isobutane operated in avalanche mode. They provide excellent time resolution but relatively poor position resolution ($\sim 3ns$ and $\sim 1cm$ respectively). RPCs consist of an anode plate and a cathode plate, both made of high resistivity plastic material. The plates are separated by spacers. When a charged particle passes through the chamber, electrons freed from the gas cause a charge avalanche which is detected by external metallic strips. The three types of muon detecting technology are built to work in concert, the DTs and CSCs providing well constrained position resolution while the RPCs provide precise timing measurements. There is much intentional overlap in the detector layout to ensure multiple measurement points for any particle and to ensure full coverage with minimal dead zones.

The muon chambers performed as well as expected in early LHC running. The reconstructed hit and segment efficiency for the 2010 data taking period is measured to be at the level of $95\% - 98\%$ throughout the muon chambers. The time resolution was measured to be $3ns$ or better for all chambers, and the spatial resolution was measured to be $80 - 120\mu m$ for the DTs, $40 - 150\mu m$ in the CSCs and $0.8 - 1.2cm$ in the RPCs. The The muon chambers work together with the Level-1 hardware trigger system described in Sec. 2.3.

## 2.3 Event Selection and Reconstruction

### 2.3.1 Event Selection

CMS must be very selective in deciding which events to store, since the high rate of collisions inside the detector, paired with multiple interactions per collision create an amount of data which is impossible to process. The hardware based level 1 (L1) trigger system is the first trigger stage and has a maximum rate of 100 kHz. An L1 accepted event is then analyzed by the software based High Level Trigger (HLT) implemented on a computing cluster with access to the combined detector information [46]. The HLT chooses which events to store

to disk and is limited by the data writing capability of the CMS computer systems. The accepted event rate must be kept below 800 Hz.

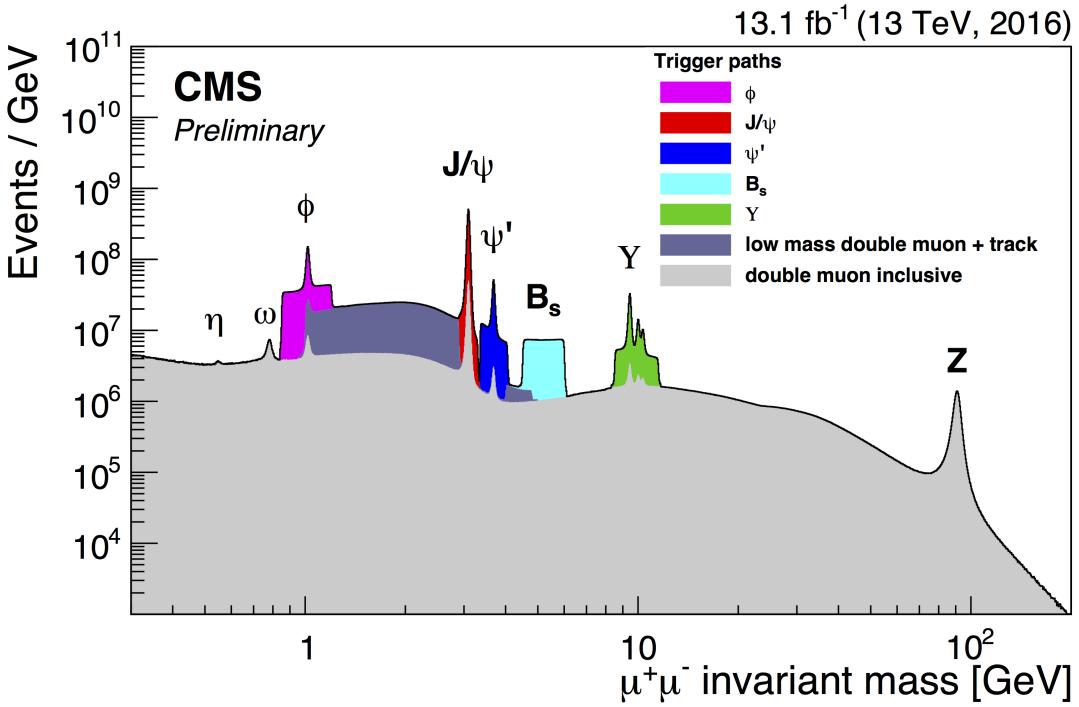



**Figure 2.11:** Dimuon Invariant mass for events collected with the various quarkonia related triggers. Strong excesses are observed where triggers include requirements on mass ranges, such as around $J/\psi$ (red), $\psi$' (dark blue), and the set of Υ resonances (light green). The signal $Z \to \mu\mu$ is clearly visible around 90 GeV

The CMS L1 trigger uses only the hardware information from the calorimeters and muon systems. The silicon system produces too much information to be analyzed on the short time scale needed for the L1. The L1 is divided into two sections called local and global. The local trigger utilizes pattern matching algorithms in each sub detector to identify track segments in the muon chambers and charge deposits in the calorimeters.

Muon reconstruction begins with each DT and CSC muon station matching the hit pattern to a set of muon momentum templates. If the track segment is found to be consistent with a high $p_{\mathrm{T}}$ track originating from the interaction point, the information is forwarded to the Track Finder. The Track Finder draws straight line segments from hit to hit, then combines the segments into a curved track. The curvature of the track corresponds to an approximate $p_{\mathrm{T}}$ measurement of the particle. The four highest $p_{\mathrm{T}}$ muons are used in

the Global Muon Trigger (GMT). The RPC detectors use a different aggregation system called the RPC Pattern Comparator Trigger (PaCT) which matches nearby RPC hits with deposits in the hadronic calorimeter to identify muons in the barrel portion of CMS. The four highest $p_{\mathrm{T}}$ muon candidates from the PaCT are also forwarded to the GMT. The CMS Global Trigger (GT) compiles all the muons from the GMT. If the event matches a table of selection criteria programmed into the GT, the L1 trigger fires and data acquisition (DAQ) begins. This process takes less than $3.2\mu s$.

The CMS HLT reconstructs all L1 events, using the information from L1 in combination with information from the pixel and silicon strip detectors. The HLT reconstruction is a simplified version of the full event reconstruction. HLT average decision time is on the order of $50ms$ per event. This speed is achieved by only reconstructing regions of the detector where L1 flagged objects are present. The addition of the pixel detector and strip tracker information means more accurate $p_{\mathrm{T}}$ measurements. The HLT contains a menu of acceptable final states to compare to each event. There are single object type triggers which accept events with only high $p_{\mathrm{T}}$ leptons , $\gamma$ or multiple jets. The analysis presented in this thesis uses a trigger specifically designed to detect multi-muon events, The L1 filter requires that at least 3 muons are detected in the muon chambers. The event is further filtered by muon charge, vertexing and dimuon invariant mass requirements in the HLT. Several different HLTs are implemented to find events decaying specifically into muons. Shown in Fig. 2.11 is a dimuon mass spectrum including all two muon quarkonia triggers. One can see the $J/\psi$ mass window shows a strong resonance highlighted in red. [55].

### 2.3.2 Reconstruction

Events selected by the HLT are transferred to computers on site, and the total event information is reconstructed, using the newest alignment and calibration information. This is known as offline reconstruction because it can lag behind data collection. The first stage is located at CERN and is called Tier-0 computing (T0). T0 receives the raw data and breaks it into several primary datasets based on the accepted triggers. For example the MuOnia dataset contains all events which pass quarkonia triggers involving muons in the final state. The raw data is archived and a copy of each dataset is sent to the Tier 1 computing centers.

There are 7 Tier 1 computing centers located around the world, the US T1 is located at Fermilab. The reconstruction software suite is known as CMS Software (CMSSW), and is updated as the run progresses to make use of higher statistics measurements of calibration and alignment. Each event is reconstructed to produce C++ objects stored in ROOT tuples for access by scientists.

Many different producer modules are used to transform the digitized detector information into a description of all muons, photons, jets and other particles found in the event. This section will focus on the two most important parts of the reconstruction process, namely the combination of hits in the silicon detectors to make tracks, and the muon reconstruction in the muon chambers. Track reconstruction in the silicon system proceeds in several steps:

- Track candidates are found by a process called seed generation which uses 2 or 3 hits to define the track. A preliminary estimate of the $p_{\mathrm{T}}$ and other properties of the track are calculated.

- A Kalman [64] algorithm extrapolates the seed track along the expected path it would take through the remaining layers of the tracker. A search is done for additional hits close to the expected path which can be added to the track candidate.

- Track fitting software recalculates the parameters of each track using all the hits found in the previous step.

- Quality criteria are tested and tracks are discarded if they do not pass the requirements.

Muon candidates based only on tracker hits are called tracker muons, they pass all the above track requirements and an additional criteria that the extrapolated trajectory intersect with at least one muon chamber that detected a particle. Similarly, a track reconstruction using only the muon station information is performed. The muon chamber track reconstruction creates a particle candidate known as a standalone muon [101]. Combining a tracker muon with a standalone muon candidate to creates a global muon [102]. The global muons use all the information from the tracker and the muon chambers to refit the candidate and remeasure all kinematic quantities. Tracks are also extrapolated inward, toward the interaction point. This extrapolation is used to estimate the origin of the particles,

and determine if two (or more) measured tracks can be fit to the same origin point. A reconstructed event is shown in Fig. 2.12.

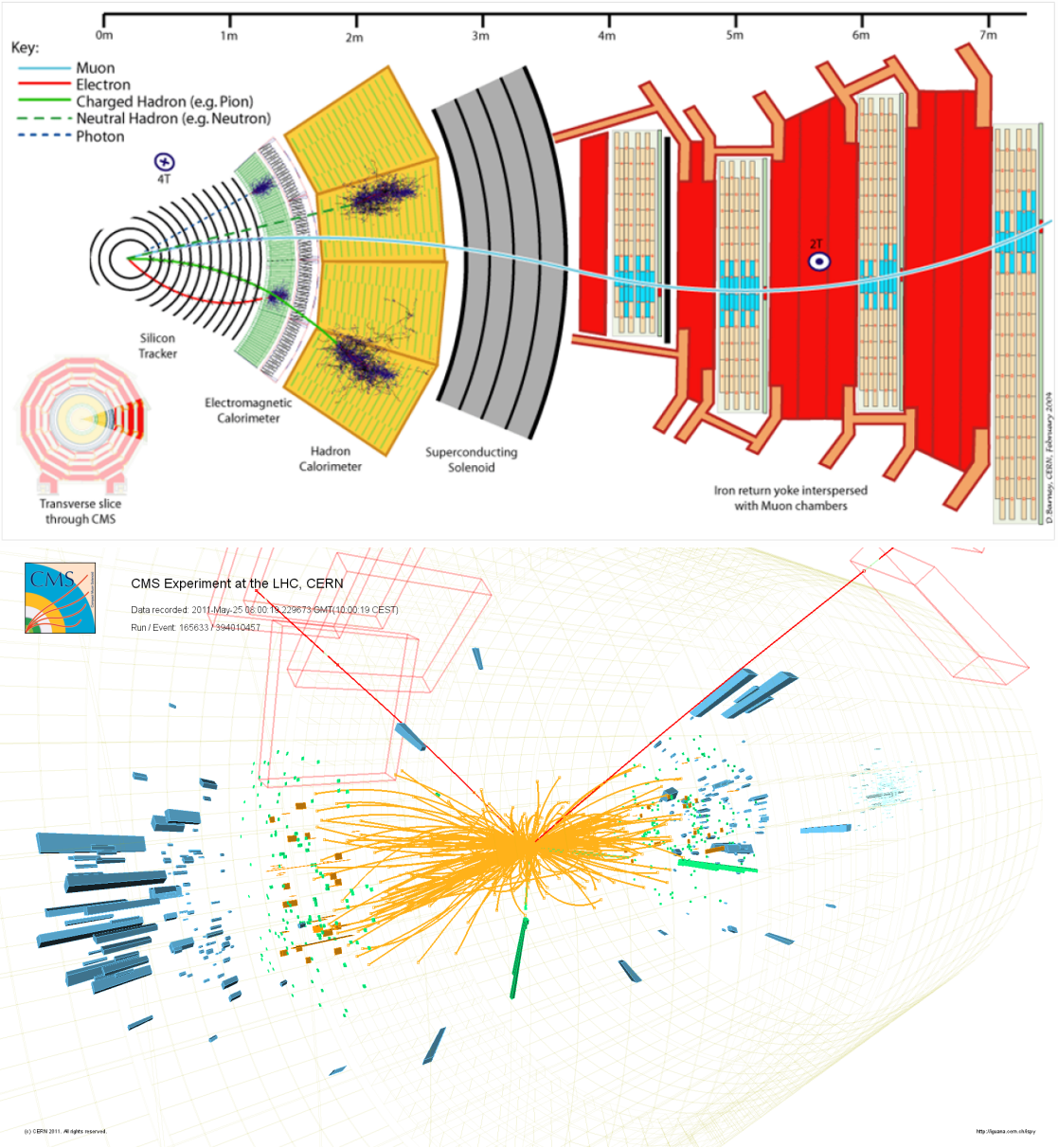



**Figure 2.12:** Top: A transverse slice of CMS with various types of particle tracks and their measurable signatures. Bottom: A CMS event display [99] which shows pixel and tracker tracks in dark yellow, ECAL deposits as green towers, HCAL deposits as blue towers, and Muon station hits in bright green (the muon station recording the hit is outlined in red). The tracks of 2 possible muon candidates are highlighted with red lines, and 2 large ECAL deposits can be found. This event is a candidate 4-lepton final state which can be produced by $J/\psi$ pair, or Higgs→ZZ for example.

# Chapter 3

# The Pixel Luminosity Telescope

## 3.1 The Luminosity Measurement

The integral of the instantaneous luminosity over time is called the integrated luminosity and is measured in inverse barns. The integrated luminosity (and its uncertainty) is used to describe the total amount of data taken by an experiment and as a normalization for cross section measurements and predictions of background contributions based on known cross sections. Therefore, a precise measurement of the luminosity benefits the results of the entire collaboration. In addition, a fast online luminosity measurement can help the LHC control team to optimize beam parameters for physics. Online luminosity measured on the order of 1 second and with ∼1% statistical uncertainty is desirable for this purpose [59]. CMS also requires an estimate of the total radioactive dose delivered to detector components. To measure this, a luminosity monitor should run independently of the normal CMS operation and trigger system, which is only active when stable beams are declared.

The measurement of relative luminosity is calibrated using a procedure known as a Van der Meer scan(VDM) [104]. This scan is performed using low intensity proton beams. The beam resolutions are measured by translating the beams across each other in the X and Y directions while measuring the relative change in particle production rates. The calibration is performed in a much lower luminosity environment than normal operation of the LHC which necessitates a detector with a linear response to particle flux over a large range. VDM scans require unique beam conditions and therefore are done only once or twice per running

year, so a luminometer must make a very stable measurement over long periods of operation. These detectors must also be monitored constantly for any change in reported luminosity, as spurious spikes or dips may cause the LHC Control room to dump the beam for fear of damage to the LHC or its experiments. The integrated luminosity over the runs in 2010, 2011 and 2012 are shown in Fig. 3.1.

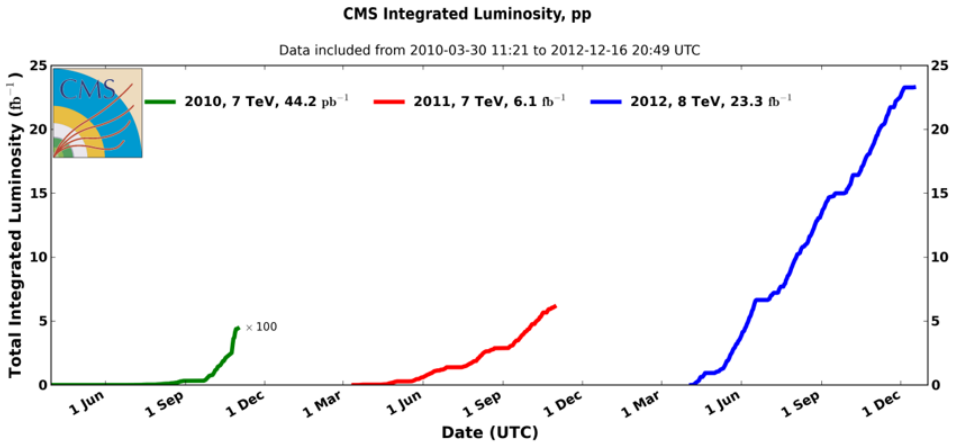



**Figure 3.1:** This plot shows the integrated luminosity delivered to the CMS detector during the years 2010 (green), 2011 (red), and 2012 (blue).

In 2011 and 2012, online luminosity is measured using the Hadronic Forward (HF) calorimeter. This detector is an array of quartz fiber cells. Cerenkov light is created by charged particles traversing the quartz and is guided to photomultipliers. Each cell makes a measurement of the energy deposited within. The number of interactions per bunch crossing can be inferred by counting the fraction of empty cells after each collision (zero counting method). This provides a measurement of the relative luminosity between bunches and is found to be linear in the luminosity range produced by the LHC during run 1. [83] A second method of measuring luminosity uses the silicon pixel detector and counts the number of charge deposits detected in each bunch crossing. This method can only be done offline, after data has been reconstructed. Cluster counting cannot provide the total radioactive dose delivered to CMS as the pixel detector is turned off during unstable beam conditions to protect the sensors. The integrated luminosity was measured with 2.5% relative uncertainty in Run 1 [54].

## 3.2 The Pixel Luminosity Telescope

The Pixel Luminosity Telescope (PLT) is a new luminometer for run 2 which is able to measure bunch by bunch luminosity in any beam conditions, independent of the CMS trigger system. A photograph of the detector is shown in Fig. 3.2 and a schematic drawing of the

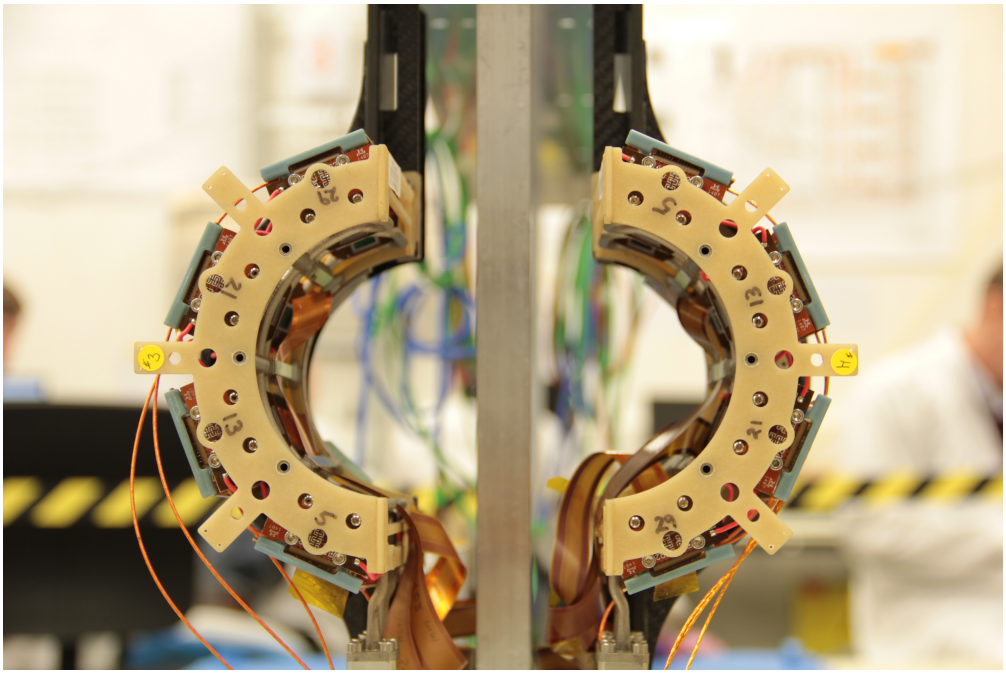


**Figure 3.2:** A photograph of one half of the PLT detector installed temporarily on metal rails in a clean room.

detector is shown in Fig. 3.3. The sensitive area is labeled in the image as the PLT cassette. Each cassette holds 4 telescopes of 3 co-linear silicon pixel detectors (planes) for a total of 12 planes per cassette. There are 4 such cassettes placed symmetrically around the interaction point (IP) of CMS. The beam pipe goes through the semi-circular shape of the cassette. The first sensitive plane of each telescope is located $171cm$ away from the interaction point in the z-direction. The remaining planes are spaced by $3.75cm$ behind the previous plane and $0.102cm$ away from the beam. This offset corresponds to an angle of 0.27 degrees, which directs the telescopes toward the nominal interaction point of CMS [80]. The silicon planes require external cooling to maintain a stable operating temperature and reduce the leakage current after irradiation. Therefore, cooling structures are attached to the cassette

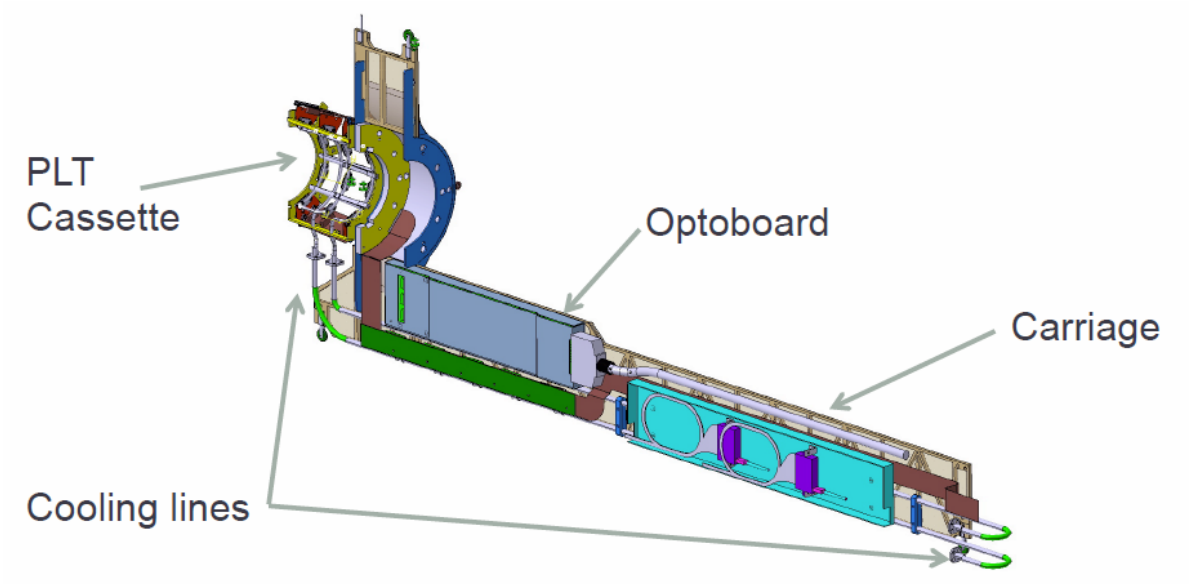



**Figure 3.3:** A schematic drawing of one quarter of the PLT detector. The sensors are located in the cassette, and the carriage holds front end electronics and cooling infrastructure. The carriage is inserted into the center of CMS such that the telescopes are 1.75 meters from the interaction point. 4 such quarters were installed in 2015.

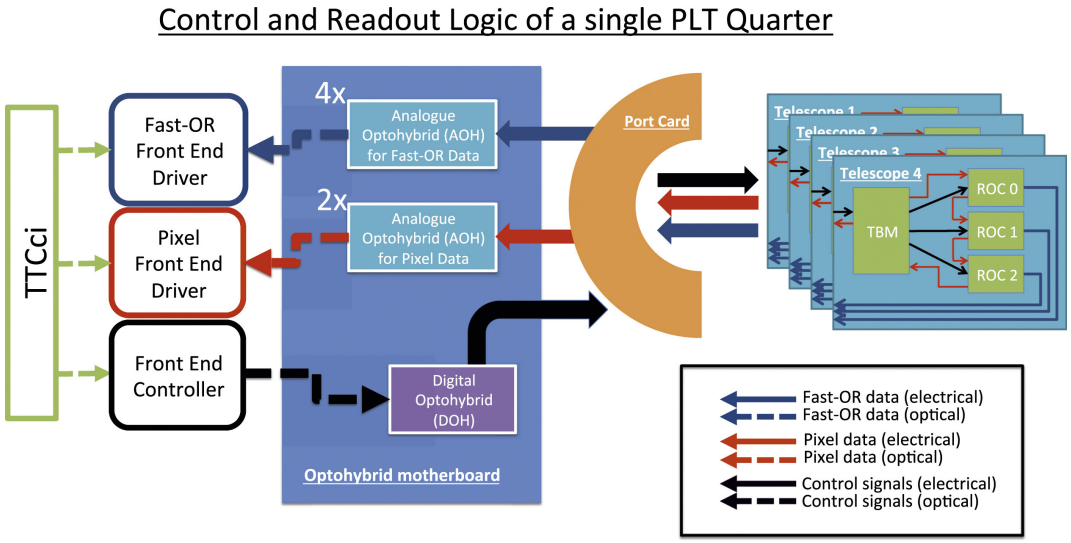



**Figure 3.4:** A schematic of the read out chain of the PLT. The optomotherboard, port card and telescopes are inside CMS. The optical connections send data to and from the computer center in a nearby cavern.

and connected to the CMS silicon tracker cooling station. Individual temperature monitors are placed at various points along the cassette.

The PLT is designed to deliver bunch by bunch luminosity with a statistical precision of $\sim$1% on the time scale of $\sim$1 second. This is achieved due to the high flux of charged particles through the detectors location, and by having a high granularity within the sensitive area to distinguish nearby tracks. The planes are made of a silicon sensor which is bonded to a pixelated read out chip shown in Fig. 3.5, using indium bump bonds. The technology is the same as the silicon pixel detector at the heart of CMS. The sensitive area consists of

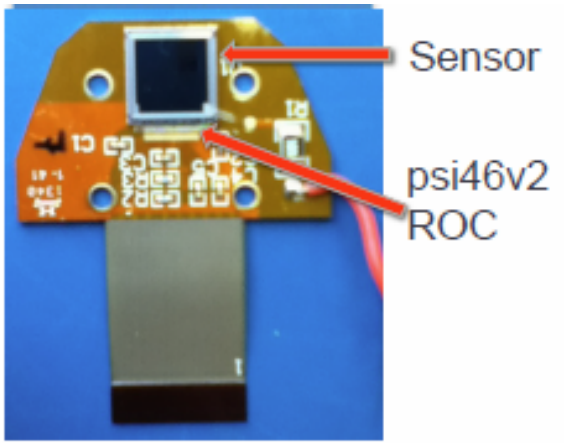



**Figure 3.5:** A single PLT sensor is shown, the black square is the silicon semiconducting material which creates an electrical signal when a charged particle passes through. The electrical signal is driven into the read out chip (ROC) by means of a bias field applied to the silicon. The information is read out of the ROC through the ribbon cable at the bottom.

52 columns and 80 rows of pixels, where each pixel is 150 $\mu$m wide and 100 $\mu$m tall. The pixels are organized into pairs of columns (double columns) and hits are stored in a rotating buffer which increments every 25ns. The signals from the sensors are sent via optical fiber to the optomotherboard, where they are transferred out of the detector and into the back end electronics, the read out chain is shown in Fig. 3.4. The full readout command is sent from the front end driver (FED) which communicates through the digital optohybryd board (DOH) to the port card. The token bit manager (TBM) for each telescope reads the correct buffer entry for each pixel and sends the charge information back to the optomotherboard which converts the electrical readout into an optical signal which is sent to the FED. The FED stores the data on disk through an Slink connection [33].

The pixel chip is equipped with a fast readout mode in addition to the pixel readout. The fast signaling method (fast-or) is a spike shaped signal which is available every $25ns$. This readout mode is the main input of the luminosity measurement. In a given bunch crossing, the FED tests each plane to see if a fast-or signal is present. A positive signal in all 3 planes in a telescope indicates a charged particle traversal of the telescope, and is called a triple coincidence. The triple coincidence count rate is measured in each bunch crossing which corresponds to a bunch-by-bunch relative luminosity. The fast-or can count several well separated hits. However, it does not include any hit location information inside the planes sensitive area. These two signaling methods are used to provide complementary information about the collisions.

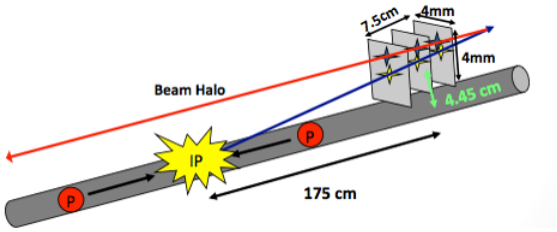



**Figure 3.6:** An artist's rendition of a single PLT telescope in relation to the interaction point of CMS. Shown are two types of signals which the PLT is able to distinguish due to particle track reconstruction from position measurements with pixelated detectors in three consecutive planes. Events from the IP due to proton collisions, and beam halo events. Beam halo consists of charged particles which are carried around the LHC but do not originate from the interaction point and hence do not measure luminosity. The contribution of halo tracks to the triple-coincidence rate must be subtracted offline based on the track reconstruction.

In the offline analysis of pixel data, coincident hits in multiple planes of a telescope are fit with straight line tracks using a chi-square minimization. The slope of a track indicates the origin of the charged particle, tracks consistent with pp collisions will extrapolate to the interaction point of CMS. Tracks which run parallel to the beam may be from beam halo particles. Beam halo consists of charged particles accelerated alongside the proton bunches, which do not result from pp interactions, and therefore should not be counted as luminosity. This is one systematic source of background in the luminosity measurement which the PLT is able to measure explicitly. Another source of background is the miscounting of a triple coincidence which was the result of more than one track, these are called accidentals. The

accidental triple coincidence can occur, for example, when a double coincidence is the result of a steeply sloped track which only traverses the first two planes in a telescope and misses the third. In coincidence, a single hit is registered on the third plane. This telescope would report a triple coincidence in this case, from a non-luminosity event. These events can be distinguished in the full pixel readout by measuring the residuals of the best-fit track. It is unlikely for the 3 hits to be co-linear, so the event will have relatively higher residuals than tracks due to pp collisions. The PLT is also capable of self monitoring the detector efficiency. This is done by extrapolating 2 hits in 2 planes into the third plane of the telescope and counting how often the expected third hit is found. These measurements of background and efficiency have been made in run 2 and applied to the luminosity measurement [86].

## 3.3 Diamond Based Detector Studies

All sensors in CMS must be able to operate consistently in the radiation environment created by the pp collisions. With future upgrades collision and pileup rates will increase for the LHC, the development of detectors must trend toward higher levels of radiation hardness. It is not economically or technically feasible to replace the inner layers of the pixel detector too frequently. The PLT was originally designed to use an alternate detector material, artificially grown carbon vapor deposition (CVD) diamond, instead of silicon. Diamond has a high band gap of $5.5eV$ at $T = 300K$ and high binding energies compared to silicon which is predicted to result in a more radiation hard sensor [34]. Diamond sensors would not need cooling, as stable operation is achieved at room temperature and diamond has a much higher breakdown voltage than silicon allowing the external field to be adjusted through a wider range of $V/\mu m$.

### 3.3.1 Pixelated Diamond Tests

This section details the tests which are performed to help assess the viability of diamond as a sensor material for the PLT showing some unexpected effects and eventually leading to the adoption of silicon.

The two major types of CVD diamond are single crystal (scCVD) and polycrystalline diamond (pCVD). The planned PLT used scCVD diamonds, so the following tests are focused on this type. A minimum ionizing particle (MIP) traversing diamond is expected to liberate an average of 36 electron/hole pairs per $\mu m$ of material. Therefore, a mean signal of 18,000 electrons is expected for perpendicular MIPs when the average diamond thickness is $500\mu m$. This signal is smaller than the average charge created in silicon of lesser thickness, but it is still well above the noise. The ratio between the amount of charge measured by the sensor, and this expected signal is called the charge collection efficiency (cce) and is given in percent. The cce is dependent on the external electric field, relating to the charge mobility $\mu_q$ and the average free charge lifetime $\tau_q$. Shown in the relation Eqn. 3.1 is average charge collected $\langle Q \rangle$ in a diamond where $Q_{gen}$ is the amount of charge created by the incident particle and $l$ is the thickness of the material.

$$\langle Q \rangle = \left( \frac{Q_{gen}}{l} \right) \left[ \frac{(\mu_e \tau_e + \mu_h \tau_h) E}{l} \right] \tag{3.1}$$

The amount of charge collected can also be expressed in terms of charge collection distance (ccd). This represents the mean distance free charge moves within a sensor. Since the charge collection measurement is based on induced current in the electrodes due to charge drift, a shorter ccd results in smaller charge signals.

The measured signal reduction due to proton irradiation in different types of CVD diamond is shown in Fig. 3.7. The curve is a falling exponential of the form $1/ccd = 1/ccd_0 + k\phi$ where $1/ccd_0$ is the charge collection distance of the diamond before exposure to radiation, $\phi$ is the proton fluence and k is a damage constant measured by dosing a diamond several times and measuring the ccd between each dose. Irradiation is known to damage the diamond structure, introducing vacancies capable of trapping free charge. The diamonds measured in this study are consistent with a value of $k =\sim 10^{-18}$ [72]. The scCVD diamonds are shifted to the left by a fluence of $3.8 * 10^{15}$ to show that all diamonds lie on the same curve. This can be better understood by saying the single crystal samples begin with a charge collection distance advantage effectively equivalent to this dose offset. Another way

to think of this effect is that pCVD intrinsically includes a similar number of traps that are created in scCVD after a fluence of $3.8 * 10^{15}$ protons.

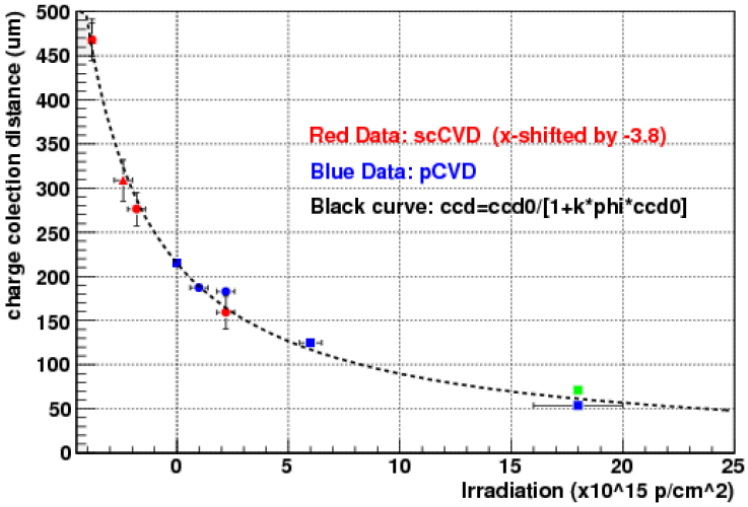



**Figure 3.7:** The measured charge collection for 2 diamond types after subsequent exposures to 24 GeV protons. The scCVD is shown in red, and the pCVD diamonds are shown in blue and green. The scCVD diamonds are offset in the x direction by the noted amount.

When diamonds are attached to pixel chips, charge deposits are often measured by multiple nearby pixels. Offline reconstruction groups adjacent pixels into so called clusters and sums the total charge collected from all pixels in the cluster. Each pixel must set a lower limit signal value which is above the combination of electronic and thermal noise called a threshold. Any charge measurement which exceeds the threshold is stored. If the cce is reduced to an extent that charge deposit signals do not cross the pixel thresholds, the detector efficiency drops.

For example, a MIP deposits charge in a diamond with 50% cce, lets also assume that this charge is detected between three pixels on the chip, distributed unevenly. The average charge deposited is 18,000 electrons, due to the cce only a 9,000 electron signal is detected. This signal is measured across 3 pixels which detect 6,000 e, 2,000 e and 1,000 e respectively. The ROC only reports pixels over threshold, so if the threshold is set to >2k e, only 1 pixel is measured, counting only a 6k e signal. The additional charge and position information from secondary or tertiary pixels is lost. The combination of cce reduction due to radiation and charge sharing in a pixelated sensor can strongly reduce detector performance. Shown

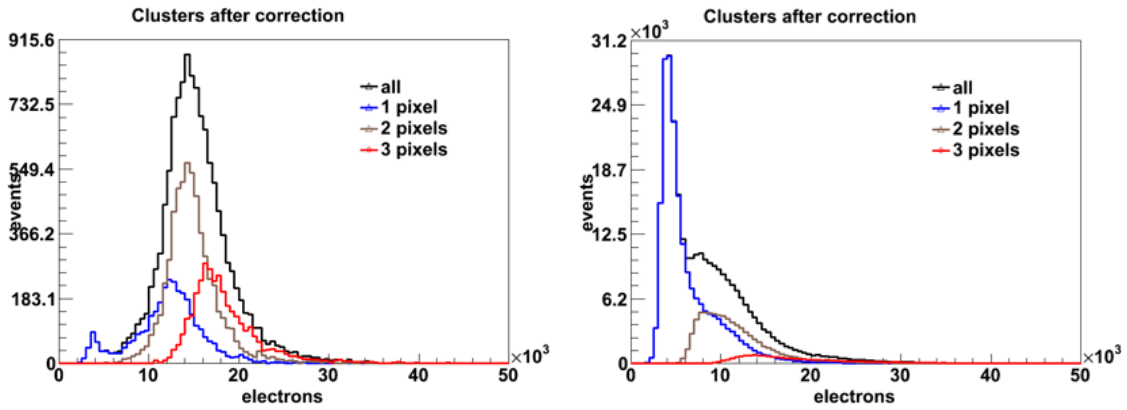



**Figure 3.8:** The left plot shows charge collection data from the pixel ROC. The ROC groups events such that adjacent pixels over threshold are measured together in a cluster. If charge is spread over 3 or more neighboring pixels, the event is classified as a $\geq 3$ pixel cluster (red). If only 2 pixels contain charge from the event, it is labeled as a 2 pixel cluster (brown). Single pixel clusters are shown in blue. The black trace is the sum of charge collected from all size clusters. On the right, is a charge signal which is indistinguishable from the noise, to illustrate how charge collection reduction in sensors harms their performance.

in Fig. 3.8 are two charge signals from pixel ROCs, one which is distinguishable from noise levels and one which is not.

An experiment conducted at Rutgers University utilized diamond sensors which were exposed to unshielded, high rapidity collision products near CMS for most of the 2012 running period. This relatively harsh radiation environment was used as a pilot test for the PLT to probe the ability of the material and hardware to withstand ionizing radiation. After run 1 was complete, the sensors were removed to conduct bench tests. The bench tests were done using a Strontium (Sr) 90 beta ($\beta$) source. The Sr90 undergoes $\beta$ decay with a half life of 28.8 years, producing 0.5 MeV which is split between the decay products, an electron, an anti-neutrino and a yttrium 90 atom. The yttrium 90 $\beta$ decays further, producing 2.3 MeV which is split between an electron, an anti-neutrino and a Zirconium 90 atom which is stable. These two $\beta$ particles both impinge on the detector surface, the higher energy electron often penetrates the entire sensor, while the lower energy beta particle often stops in the diamond bulk. The setup is triggered on a coincidence between the pixel chip fast-or signal and a downstream scintillator, so only penetrating betas are measured. The incident rates were

varied between 600Hz and 4kHz based on the distance of the source from the sensor. $\beta$ particles have a slight deviation from a MIP, they are estimated to deposit 6% more charge.

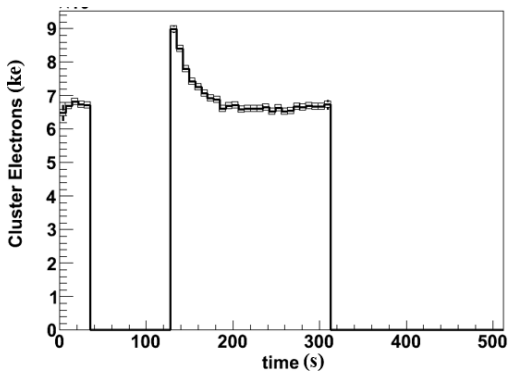



**Figure 3.9:** The charge collected per cluster integrated over time. The source is opened at the ∼125 second mark, charge collection begins around 9k electrons per cluster but quickly drops to a plateau of 7k e.

The source is opened at the $\sim$ 125 second mark and a charge collection drop observed in Fig. 3.9. This behavior is seen in several other irradiated diamond samples which were tested and observed qualitatively. The effect is due to internal polarization and goes hand in hand with trapping centers introduced by irradiation. As electrons and holes drift to opposite sides of the diamond, they are trapped en-route. The build up of charge causes an internal electric field which opposes the external field, further reducing the cce according to Eqn. 3.1. This effect is not accounted for in the damage curve, effectively shortening the lifetime of these sensors in a harsh radiation environment. This polarization in a set of diamonds is studied in detail in [34].

The effect is shown in multiple diamonds with varying magnitudes. The effect is dependent on several factors, these include the surface preparation of the diamond detector, the rate of incident charged particles and the darkness of the experimental setup. Several tests are done with laser light at various wavelengths directed into the diamond. The hypothesis is that the trapped charge could be freed by the appropriate wavelength of light, eliminating the internal electric field, and keeping the diamond cce consistent with the damage curve shown in Fig. 3.7. One test of this hypothesis is shown with a 650nm red laser pointer in Fig. 3.10. Charge collection fluctuations on the order of ∼60% are seen

to coincide with laster light. Several other wavelengths of laser and LED light are studied

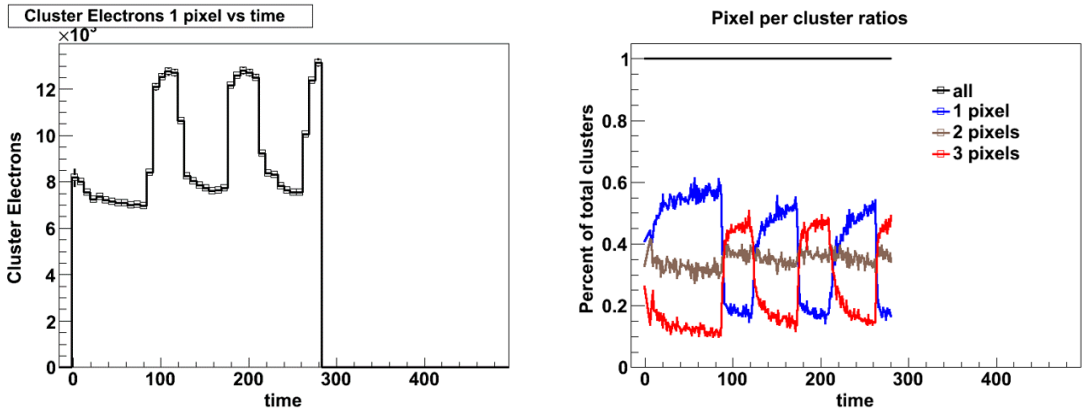



**Figure 3.10:** Tests done with a 650nm red laser on a diamond sensor. The left plot shows the charge collected from 1 pixel clusters, the peaks and valleys correspond exactly to the laser turning on and off respectively. In the right plot is shown the distribution of single pixel clusters (blue), 2 pixel clusters (brown) and $\geq 3$ pixel clusters (red) this plot shows a large change in single and large cluster population while the laser is turned on.

including green laser light, and infrared spectrum LEDs. These results, in combination with other tests inside the PLT collaboration resulted in the determination that scCVD diamond, in its current state, is not technically feasible to install into the PLT, when so much unexpected cce reduction was present. The PLT was redesigned to use silicon sensors, with diamonds undergoing further investigation for future applications.

### 3.3.2 TCT studies

Additional bench tests on diamond sensors are performed to better understand the internal electric field of irradiated sensors by applying the Transient Current Technique (TCT)[91]. A TCT measurement involves depositing a large amount of charge on one side of the diamond sensor, then drifting either the electrons or holes across the material with an applied electric field. The charge is created using Polonium (Po) 210 which decays through $\alpha$ radiation into Lead (Pb) 206. The 5.3 MeV $\alpha$-particles, unlike MIPs, only penetrate about 10 $\mu m$ into the diamond, depositing all their energy within this distance. 13 eV is required to liberate an electron/hole pair in diamond, so the 5.3 MeV $\alpha$-particles produce a total charge signal of

~400k electrons which are drifted across the entire sensor. Other studies using this technique are detailed in [91].

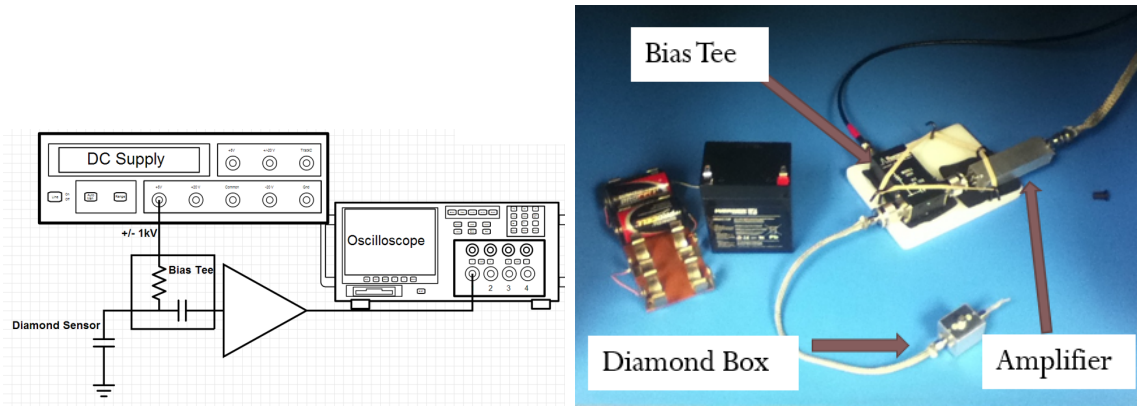



**Figure 3.11:** A schematic of the TCT setup is shown on the left and a photograph of the setup is on the right.

The TCT experimental setup, shown in Fig. 3.11, utilizes a DC voltage supply which is applied to one side of the diamond sensor up to a maximum of $\pm 1kV$ through the so called bias tee. The bias tee decouples the diamond sensor and the high voltage from the sensitive amplifier using a capacitor. The alpha source is placed on the grounded side of the diamond sensor and the charge is drifted toward the DC supply. The drifting charge modifies the voltage on the sensor, which is compensated for by means of a small current from the supply. This current also changes the charge on the bias tee capacitor which is measured by the amplifier and displayed on the oscilloscope.

Some preliminary results from the TCT studies are shown in Fig. 3.12. A non irradiated diamond is measured applying different bias voltages. The pulse shape can be seen to widen with decreasing bias. Each pulse in the figure is the average of several hundred measurements. The length of the pulses, corresponding to electron transit time $t_c$ range from $10 - 15ns$, which implies a drift velocity $v_{dr}$ of electrons $v_{dr}(E) = \frac{d}{t_c(E)}$. Where $d$ is the width of the sensor ($\sim 500\mu m$). Drift velocity depends on electric field strength E as can be seen in the figure.

An additional qualitative study was done on 3 different diamonds exposed to increasing neutron fluences. These sensors were measured with TCT, and an average of several hundred pulses for each diamond at the listed voltage is shown in Fig. 3.12. The diamonds were

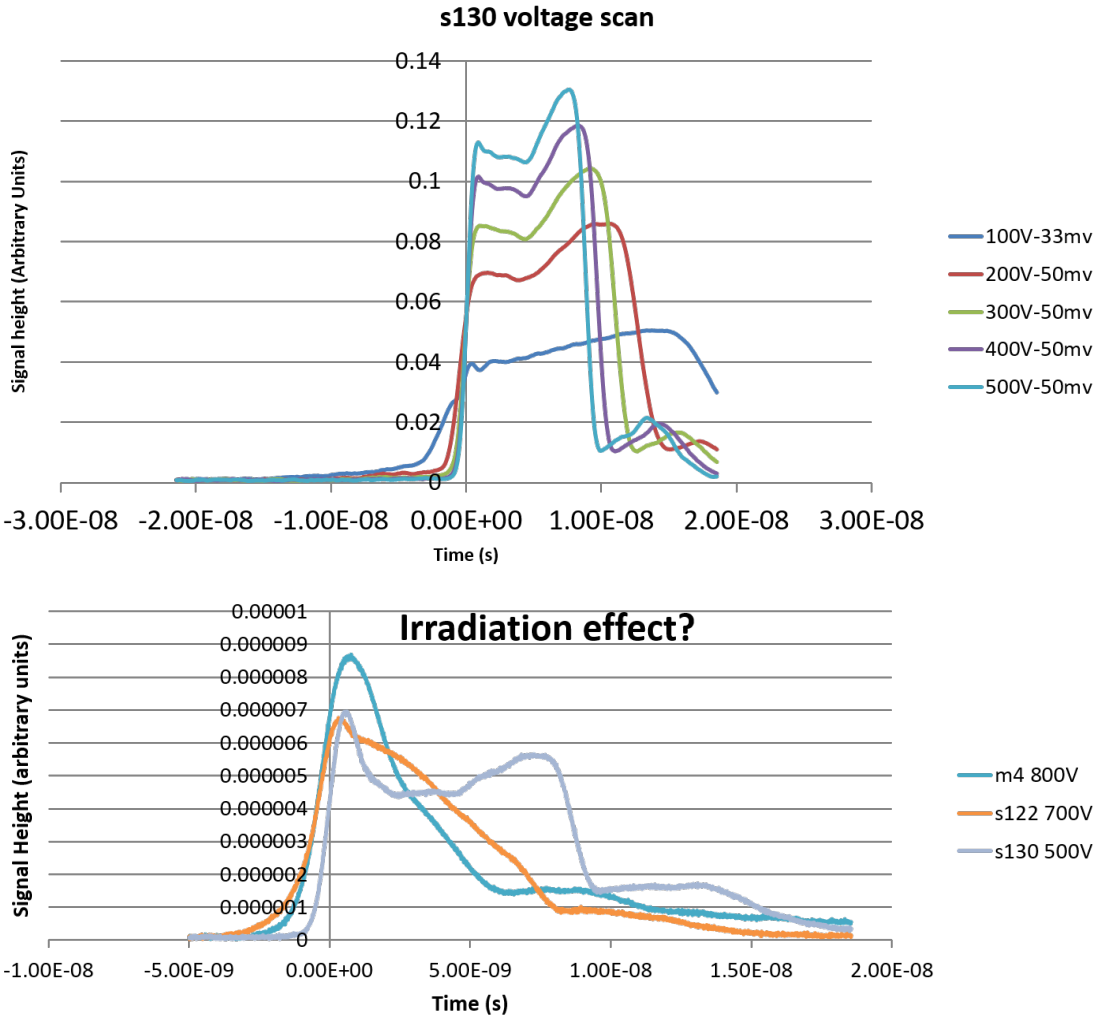



**Figure 3.12:** The top plot shows an unirradiated diamond's average charge collection pulse at different applied voltages. The bottom plot shows a comparison of an average pulse from 3 diamonds with differing levels of irradiation and applied bias. s130 is unirradiated, s122 has a total dose of $3 * 10^{14} n/cm^2$ and m4 has a total dose of $4 * 10^{14} n/cm^2$.

irradiated using the High Flux Isotope Reactor (HIFR) at Oak Ridge National Laboratory (ORNL). The sensor named s130 is not irradiated to a significant dose, s122 has a total dose of $3 * 10^{14} neutrons/cm^2$ and the diamond named m4 has been exposed to a dose of $4 * 10^{14} neutrons/cm^2$. The diamonds can be seen to have very different pulse shapes with shorter pulse lengths corresponding to higher neutron fluence.

These charge pulses also show a lower cce for heavily irradiated diamonds, this can be related to the charge carrier lifetime through Eqn. 3.1. As more trapping centers are created through radiation damage, the average free charge lifetime in the diamond decreases. Several further studies can be done to improve the understanding of the trapping and polarization effects. TCT studies while using a high rate $\beta$ source to polarize the diamond can probe the polarization field. Also, laser light can be introduced to irradiated diamonds, to see if the charge lifetime is restored. In addition a TCT pulse could be measured in a test which fills all the traps in a diamond with a high rate source, then a laser is turned on to free the trapped charge carriers. The shape of this pulse could give hints to the trap location within the diamond.

The polarization effect shortens the sensor lifetime of pixelated scCVD diamond detectors in high radiation environments as shown in Fig.3.13. The expected CCE vs. radiation damage is shown by the black curve, with the red curve representing the CCE observed in a diamond after a trapped charge steady state is reached. In reality, a sensors CCE would vary in the gap between the two curves depending on the amount of trapped charge. Turning the high voltage off, or reversing the polarity frees trapped charges, also exposing the diamond to light as in the red laser tests, affects the polarization. This effect is disadvantageous for a luminosity monitor which relies on consistent efficiency over many variations in run and beam conditions to produce a measurement with low systematic uncertainties. In addition the sensors CCE falls to a critical level at lower fluence than initially expected, eliminating the sensor lifetime gain due to radiation hardness. Ultimately the diamond PLT was re-designed to use existing silicon sensors for the 2015-18 run period of CMS. The manufacturing of scCVD diamonds may improve such that they are suitable for usage in High Luminosity LHC detectors in the future.

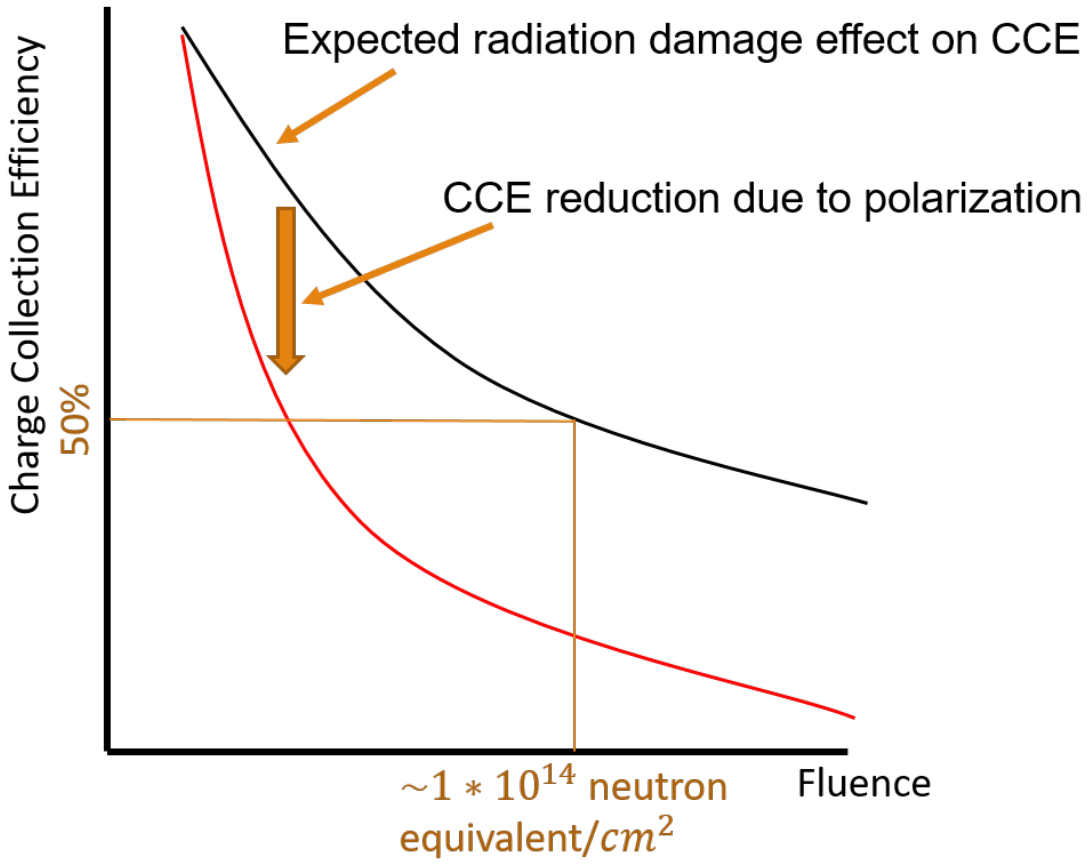



**Figure 3.13:** A representation of the effect of radiation damage in a scCVD diamond when paired with the observed polarization effect. The black curve represents the expected CCE vs. fluence from a diamond which exhibits no polarization, the red curve represents a fully polarized diamond. In reality the measured CCE will be somewhere between the two curves for a given fluence.

# Chapter 4

# Data Analysis

## 4.1 Motivation

The measurement of the simultaneous production of two prompt $J/\psi$ mesons in the collision of protons at $\sqrt{s} = 8$ TeV provides general insight into heavy quarkonia production in proton collisions in the LHC. In contrast to earlier experiments where quark-anti-quark annihilation dominated [27, 28], in the case of proton-proton collisions at the LHC, the production process in lowest order $\alpha_S$ is gluon-gluon fusion [71].

Earlier theoretical predictions assume single parton scattering (SPS) [74, 71, 107, 84, 92, 78, 35, 85, 81, 98] using color-singlet models (CSM)[45, 29, 30]. In other SPS models using non-relativistic QCD (NRQCD)[39] at parton level the two $J/\psi$ mesons are either produced as color singlet states or color octet states that turn into singlets after emitting gluons. Color octet contributions at $J/\psi$ pair transverse momenta below 15 GeV/$c$ and low invariant masses are expected to be negligible, but play a greater role as transverse momenta increase [35, 92]. According to next-to-leading order QCD calculations, contributions from color singlet heavy-quark pair production are enhanced toward higher transverse momenta [44, 26, 67, 82]. Fig. 4.1 shows representative diagrams for prompt $J/\psi$ pair production in different orders of $\alpha_s$ in perturbative QCD. There are 31 Feynman diagrams in leading order of perturbative QCD describing color-singlet charmonium pair production in the reaction $gg \to J/\psi J/\psi$ corresponding to $\alpha_S^4$. At $\alpha_S^5$ (e.g. Fig. 4.1 (b)) additional gluons are emitted: $gg \to J/\psi J/\psi g$. Other processes of lesser importance are $gq \to J/\psi J/\psi q$ where

an incoming or outgoing gluon are substituted with a quark. Typically, loop contributions can be neglected leading to 438 diagrams with real emissions. At $\alpha_s^6$ processes such as $gg \to J/\psi J/\psi c\bar{c}c$ (Fig. 4.1 (c)) contribute with more than 2000 non-trivial Feynman graphs.

The CMS experiment samples a $J/\psi$ regime complementary to LHCb, with coverage of higher transverse momenta and central rapidity values and hence is more attuned to such contributions. Lansberg et al. [82] find that next-to leading order single parton scattering calculations at $\alpha_s^5$ dominate the yield at large momenta when compared to the CMS measurement of prompt $J/\psi$ pair production at $\sqrt{s} = 7$ TeV [103] and D0 at the Tevatron [17].

With the high flux of incoming partons at the LHC, it is expected that multiple hard parton scatterings take place, where the simplest is two short distance interactions from a single hadron-hadron collision, commonly referred to as double parton scattering (DPS) [79, 31, 36, 32]. An example diagram for DPS is shown in Fig. 4.2.

These multi-parton scattering contributions are difficult to address within the framework of perturbative QCD and experimental studies are needed (see e.g. Ref. [78] and references therein). The DPS contribution to $J/\psi$ pair production in contrast to hadronic jet and open charm production occurs at lower partonic $p_{\mathrm{T}}$ where different mechanisms may apply [37]. As $J/\psi$ pair production is dominated by interactions of gluons, it can provide information about their transverse momenta and their correlations inside the proton. It also helps with the understanding of backgrounds in new physics searches, such as in multi-jets, and also $Z + \bar{b}b$, $W^+W^-$.

The production of two quarkonia via DPS is usually assumed to result from two different partonic interactions. Neglecting the parton correlations in the proton, the contribution of this mechanism can be estimated from the prompt single $J/\psi$ production cross section $\sigma_{J/\psi}$ as follows [42, 43, 60]:

$$\sigma_{J/\psi J/\psi}^{DPS} = \frac{1}{2}\frac{\sigma_{J/\psi}^2}{\sigma_{eff}} \tag{4.1}$$

where the factor 1/2 accounts for identical particles in the final state. The $\sigma_{eff}$ is an effective cross section that is expected to account for the effective size of the parton-parton interaction and should therefore be independent of process and center-of-mass energy if

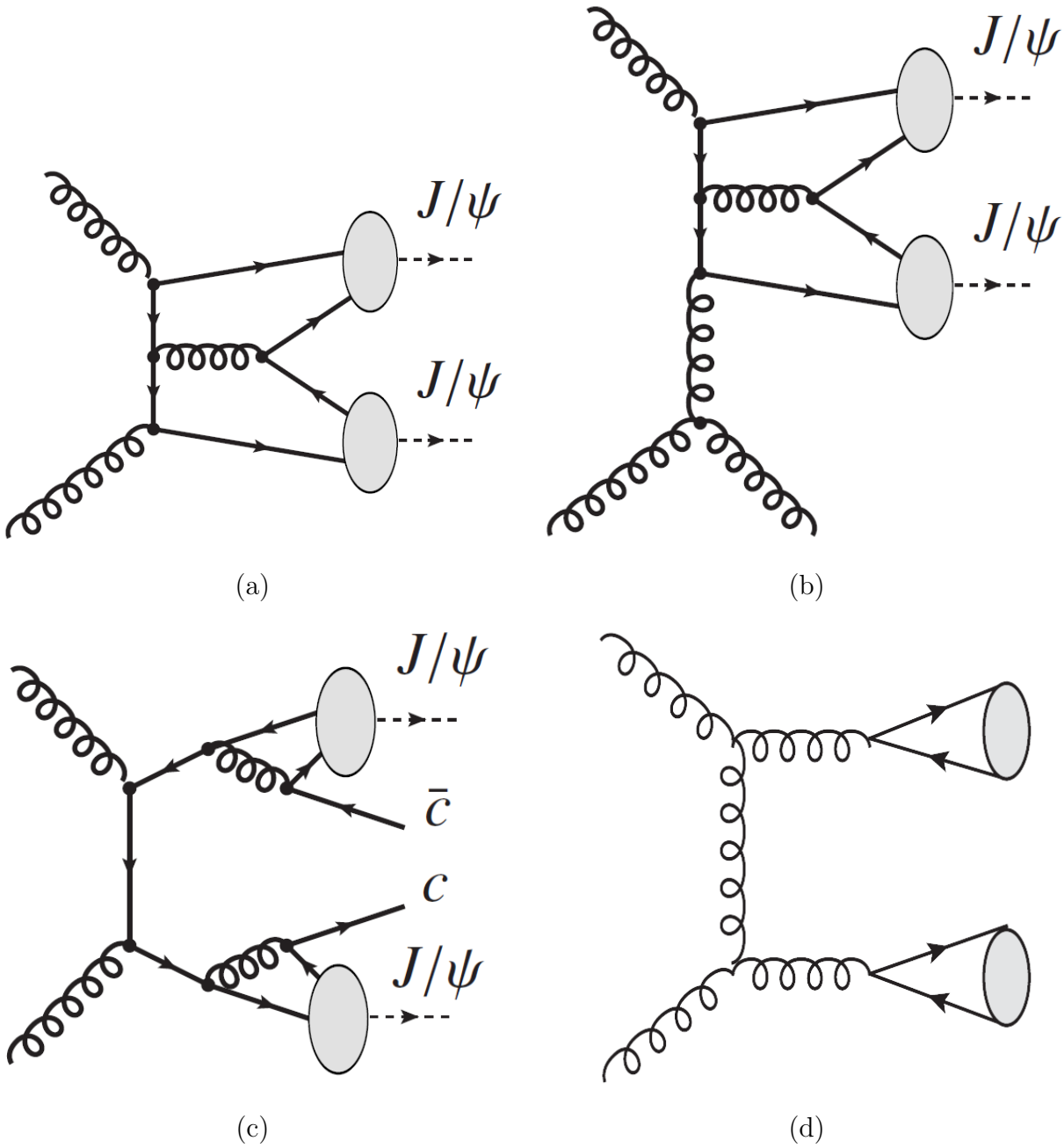



**Figure 4.1:** Examples of Feynman diagrams of SPS color-singlet prompt $J/\psi$ pair production in $pp$ collisions in (a) leading-order (LO), (b) next-to-leading order (NLO), and (c) next-to-next leading order (NNLO), and (d) SPS color-octet prompt $J/\psi$- pair production

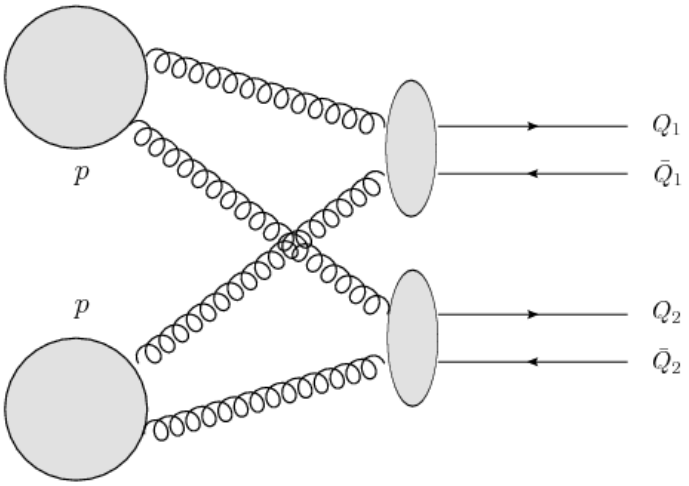



**Figure 4.2:** Production of two quark anti-quark pairs in the double parton scattering process.

factorization is valid. Recent measurements of $\sigma_{eff}$ in final states with jets find it to be in the range $12 - 20$ mb [51, 5, 18, 14]. However, measurements of $J/\psi$ pair [15] and $J/\psi$ $+\Upsilon(1S)$ [16] production in $(\bar{p}p)p$ collisions yield lower values. Causes of the differences are theorized to be related to breaking of factorization (see e.g. [62, 75, 38]). Differences between jet and quarkonia productions may also indicate a dependence on the flavor of the initial partons since jets are also produced from $\bar{q}q$ and $qg$ parton states.

The access to $J/\psi$ pair production at 8 TeV allows for the comparison of data with models that include higher order corrections and became available after the first round of LHC measurements at 7 TeV. The data provide a test of the CM energy dependence, particularly of the DPS contribution. The detailed understanding of the non resonant production in this final state is critical to provide background estimations for 4 muon decay processes. The Higgs boson is expected to decay through a $J/\psi$ pair, as one example. Both the Higgs and prompt $J/\psi$ pair production occur primarily though gluon-gluon fusion which allows studies of SPS in $J/\psi$ channels to provide insight into gluon behavior in high energy collisions. This chapter details the measurement produced by the author using CMS data from 2012.

The $J/\psi$ pair production cross section is measured using $pp$ collision data collected with the CMS experiment in 2012 at $\sqrt{s} = 8$ TeV. The $J/\psi$ mesons are reconstructed via the $\mu^+\mu^-$ final state, and they are ordered by their transverse momentum. The acceptance region is defined by the individual $J/\psi$ transverse momentum $p_{\mathrm{T}}^{J/\psi}$ and rapidity $|y^{J/\psi}|$: $p_{\mathrm{T}}^{J/\psi} > 8.0$ GeV/$c$ for $|y^{J/\psi}| \leq 0.95$, $p_{\mathrm{T}}^{J/\psi} > 8.0 \rightarrow 5.5$ GeV/$c$ (where the $p_{\mathrm{T}}$ threshold scales

linearly from 8.0 to 5.5 GeV/$c$) in the region $0.95 < |y^{J/\psi}| < 1.40$, and $p_{\mathrm{T}}^{J/\psi} > 5.5\,\mathrm{GeV}/c$ for $1.40 \leq |y^{J/\psi}| \leq 1.90$.

The differential cross section for prompt $J/\psi$ pair production within this acceptance region is measured in several variables. Predictions for different production modes are compared to the differential cross section distributions. The relative content of double parton scattering is estimated. Both $J/\psi$ mesons are assumed to be unpolarized, motivated by the fact that all analyses of quarkonia at LHC yield small polarizations [21, 48, 50, 9, 10].

## 4.2 Analysis Strategy

The cross section measurement is provided in a pre-defined region of the $J/\psi$ acceptance that in turn is constrained by the muon identification and reconstruction capabilities of CMS. The differential cross section of $J/\psi$ pair production in bins of event variable $x$ is calculated using the following equation:

$$\frac{d\sigma(pp \to\ J/\psi\ J/\psi + X)}{dx} = \frac{n_{\mathrm{sig}}}{a \cdot \epsilon \cdot BF(J/\psi\ \to \mu^+\mu^-) \cdot BF(J/\psi\ \to \mu^+\mu^-) \cdot \Delta x \cdot \mathcal{L}} \quad (4.2)$$

with:

- $n_{\mathrm{sig}}$, measured signal yield extracted with a maximum likelihood fit,
- $a$, muon acceptance for the given $J/\psi$ variable interval,
- $\epsilon$, CMS detector efficiency for triggering, reconstructing, and identifying muons from $J/\psi$ within the $J/\psi$ acceptance,
- $\mathcal{L}$, total integrated luminosity of the dataset.
- $BF$, The world average of the branching fraction ($J/\psi\ \to \mu^+\mu^-$) [90].

The total cross section in the $J/\psi$ acceptance is determined by summing over all intervals $\Delta x$. This analysis measures differential production in $\Delta x$ bins of 8 variables including:

- $J/\psi$ pair invariant mass ($M^{\mathrm{JJ}}$),

- absolute rapidity ($|y^{\mathrm{JJ}}|$),
- absolute separation in rapidity between the $J/\psi$ ($|\Delta y|$),
- the $J/\psi$ pair transverse momentum ($p_{\mathrm{T}}^{\mathrm{JJ}}$),
- the leading $J/\psi$ $p_{\mathrm{T}}$, ($p_{\mathrm{T}}^{J_1}$) is the higher $p_{\mathrm{T}}$ $J/\psi$,
- the subleading $J/\psi$ $p_{\mathrm{T}}$, ($p_{\mathrm{T}}^{J_2}$) the lower $p_{\mathrm{T}}$ $J/\psi$,
- the $p_{\mathrm{T}}$ asymmetry ($p_{\mathrm{T}}^{J/\psi}\mathcal{A}$) defined as $p_{\mathrm{T}}\mathcal{A} = |\frac{p_{\mathrm{T}}^{J_1} - p_{\mathrm{T}}^{J_2}}{p_{\mathrm{T}}^{J_1} + p_{\mathrm{T}}^{J_2}}|$,
- the absolute separation in $\phi$ between the $J/\psi$ ($|\Delta\phi|$) where $\phi$ is the angle defined from the positive x-axis of CMS

## 4.3 Samples

### 4.3.1 Data

The data for this analysis were accumulated with the CMS detector during the $\sqrt{(s)} = 8\,\mathrm{TeV}$ running period of the LHC in 2012. The total integrated luminosity delivered to CMS was $23.3\,\mathrm{fb}^{-1}$ of which CMS recorded $21.79\,\mathrm{fb}^{-1}$ [54]. The reconstruction uses the official software releases `CMSSW_5_3_7_patch5 (2012 data)`. The data sets are selected according to the official JSON files:

`Cert_190456-208686_8TeV_22Jan2013ReReco_Collisions12_JSON_MuonPhys.txt`.

This analysis uses the `MuOnia` dataset which consists of the subset of all events collected during times when the muon chambers and the tracker were performing well. The data used in this analysis correspond to an integrated luminosity of $20.2\,\mathrm{fb}^{-1}$. The data sets are listed in Table 4.1.

### 4.3.2 Simulation

This analysis utilizes several types of Monte Carlo simulations to generate prompt $J/\psi$ pair events.

**Table 4.1:** The data set used in this analysis and the corresponding integrated luminosity ($\mathcal{L}$).

| Data Set Name | $\mathcal{L}$ ( $\text{fb}^{-1}$ ) |
|---|---|
| /MuOnia/Run2012A-22Jan2013-v1/AOD | 0.44 |
| /MuOnia/Run2012B-22Jan2013-v1/AOD | 4.83 |
| /MuOnia/Run2012C-22Jan2013-v1/AOD | 7.31 |
| /MuOnia/Run2012D-22Jan2013-v1/AOD | 7.58 |
| MuOnia 2012 Sum | 20.16 |

- DPS prompt $J/\psi$ pair without pileup at 8 TeV: Events in the Double Parton Scattering (DPS) Monte Carlo are produced in Pythia 8 [97] using the CTEQ6L1 PDF set with double hard scattering and charmonium production enabled. Higher states are forced to decay through $J/\psi$ which is forced to decay to 2 muons. A filter was applied at generator level requiring that events contain at least one $J/\psi$ and that the muons fall inside loose acceptance criteria, namely $|\eta^{\mu}| < 2.5$ and $p_{\mathrm{T}}^{\mu} > 1\,\mathrm{GeV}/c$. Only events passing the `HLT_Dimuon0_Jpsi_Muon` trigger path were reconstructed.

- DPS prompt $J/\psi$ pair with pileup at 8 TeV: Events are produced the same way as the no-pileup DPS sample, with pileup mixing occurring at the RAW tier according to the `mix_2012_Summer_50ns_PoissonOOTPU_cfi` configuration.

- SPS-LO and NLO $J/\psi$ pair at 8 TeV: Events in the Single Parton Scattering (SPS) Color Singlet $J/\psi$ pair hard processes are generated using the HELAC-Onia generator package [94, 95] and passed to Pythia 8 as a LesHouches file to be hadronized. The $J/\psi$ are generated inside a loose acceptance ($p_{\mathrm{T}}^{J/\psi} \geq 4$ GeV/$c$ and $|y^{J/\psi}| \leq 5$). Only events passing the `HLT_Dimuon0_Jpsi_Muon` trigger path were reconstructed.

- SPS-LO and NLO $J/\psi$ pair at 8 TeV with Pileup: Events are produced the same way as the no-pileup SPS sample, with pileup mixing occurring at the RAW tier according to the `mix_2012_Summer_50ns_PoissonOOTPU_cfi` configuration.

- $J/\psi$ re-throwing for acceptance studies: $J/\psi$ candidates from Data, DPS and SPS-NLO are re-decayed into muons several thousand times. The muon acceptance is applied to

the resulting muon sample to measure event by event acceptances. This MC is also used to study $J/\psi$ polarization in Sec. 4.8.

- SPS-LO: Events are produced by a generator detailed in [35] and hadronized with Pythia 6 [96]. The generator produces the color singlet $J/\psi$ pair hard process which allows feed down process from $J/\psi$' to decay to $J/\psi$.

Simulated MC events are selected with the same criteria as data events.

## 4.4 Event Selection and Reconstruction

### 4.4.1 Initial Selection

This analysis utilizes the `HLT_Dimuon0_JPsi_Muon` trigger path, designed by the BPH-trigger group to select di-$J/\psi$ to 4-muon events without requiring a prescale factor. This trigger requires the presence of at least three muons, two of which must be oppositely charged, have a dimuon invariant mass $m_{\mu\mu}$ in the $J/\psi$ mass window $2.85 < m_{\mu\mu} < 3.35$ GeV/$c^2$ and a vertex fit probability greater than 0.5% as determined by a Kalman vertex algorithm [64]. The event selection relies on many muon, dimuon and 4-muon candidate requirements. The initial selection is shown in detail in Table 4.2. The requirements are also described in the following paragraphs. The initial selection is designed to be a minimum of requirements which maintains good muon candidate quality while not reducing the sample to extremely low statistics. Further cuts are applied later in the analysis based on inspection of the initially selected sample.

At least four muons in the event are required to belong to the `tracker muon` or `global muon` category. The specific definitions of `tracker muons` and `global muons` can be found in [89] . Reconstruction of muons proceeds by associating segments in the muon chambers with tracks provided by the silicon tracker. A given muon segment can be associated with more than one silicon track at the time of reconstruction, allowing reconstructed muons to share segments. An arbitration algorithm described in [89] then assigns each muon segment to a unique muon track. The candidate selection requires that all muons satisfy the arbitration `MuOneStationTight`. Muons are further required to pass the following quality

criteria: the associated track segment must have a hit in at least 1 layer of the pixel detector and have at least 6 total tracker layers with hits, muons with a transverse impact parameter $d_0$ greater than 0.3 cm or a longitudinal impact parameter $d_z$ greater than 20 cm are excluded. These criteria correspond to the `soft muon` selection as defined by the B-Physics group [100], but were not available as selector for release CMSSW_5_3_8_patch3.

**Table 4.2:** The event yield after successive applications of initial quality criteria for the selection of $J/\psi J/\psi$ candidates. Also shown is the % reduction in sample size due to each requirement.

| Requirement | N Events | (2012) %Fraction$_{\text{step}}$ |
|---|---|---|
| Trigger | 6768257 | 100.0 |
| >4 Global OR Tracker Muons | 5278377 | 78.0 |
| MuOneStationTight | 3064313 | 58.1 |
| $>0$ pixel layers / track | 2535059 | 82.7 |
| $>5$ tracker layers / track | 1616156 | 63.8 |
| track $d_0 < 0.3$ cm, $d_z < 20$ cm | 1510697 | 93.5 |
| two $\mu^+\mu^-$ candidates | 872114 | 57.7 |
| $J/\psi$ vtx prob $> 0.5$ % | 515923 | 59.1 |
| $p_{\mathrm{T}}(\mu\mu) > 0$ & $\lvert\eta\rvert < 2.4$ | 511423 | 99.1 |
| $2.85 \leq m_{\mu\mu} \leq 3.35\,\mathrm{GeV}/c^2$ | 38996 | 7.6 |
| $J/\psi$ pair candidates | 20489 | 52.5 |
| 3 muons L3 matched | 16070 | 78.4 |
| 4-$\mu$ vtx prob $> 0.5$ % | 3594 | 22.4 |

All `soft muon` candidates in an event passing the above quality criteria are required to be within a preliminary muon acceptance defined as $\eta \leq 2.4$.

The muons are combined into charge neutral pairs to create dimuon candidates. These dimuon candidates are fit to a common vertex using a Kalman Vertex algorithm [64], the probability for this fit is required to be greater than 0.5%.

The invariant mass of both dimuon candidates is required to fall within a range corresponding to the interval allowed by the HLT, centered at the $J/\psi$ mass: $m_{\mu\mu} \in [2.85, 3.35]\,\mathrm{GeV}/c^2$. Fig. 4.3 shows the invariant $\mu\mu$ mass of dimuon candidates passing the above criteria in the MuOnia datasets. An enhancement near the nominal mass of $J/\psi$ (3.097 $\mathrm{GeV}/c^2$) is visible. Muons are matched to the L3 level trigger via object matching by filter (*hltTripleMuL3PreFiltered0*). The default matching criteria based on the offline

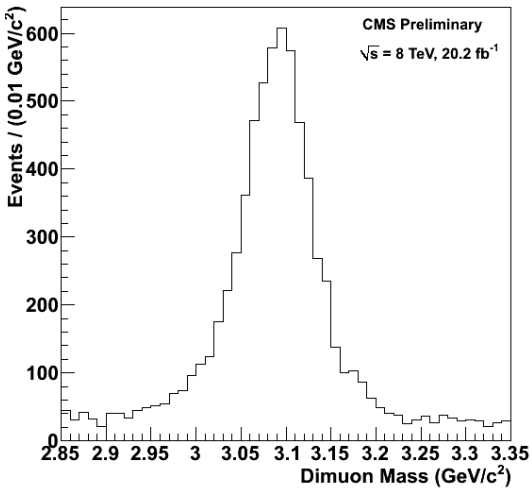



**Figure 4.3:** The plot shows the $\mu\mu$ invariant mass for passing dimuon candidates in the mass interval allowed by the HLT.

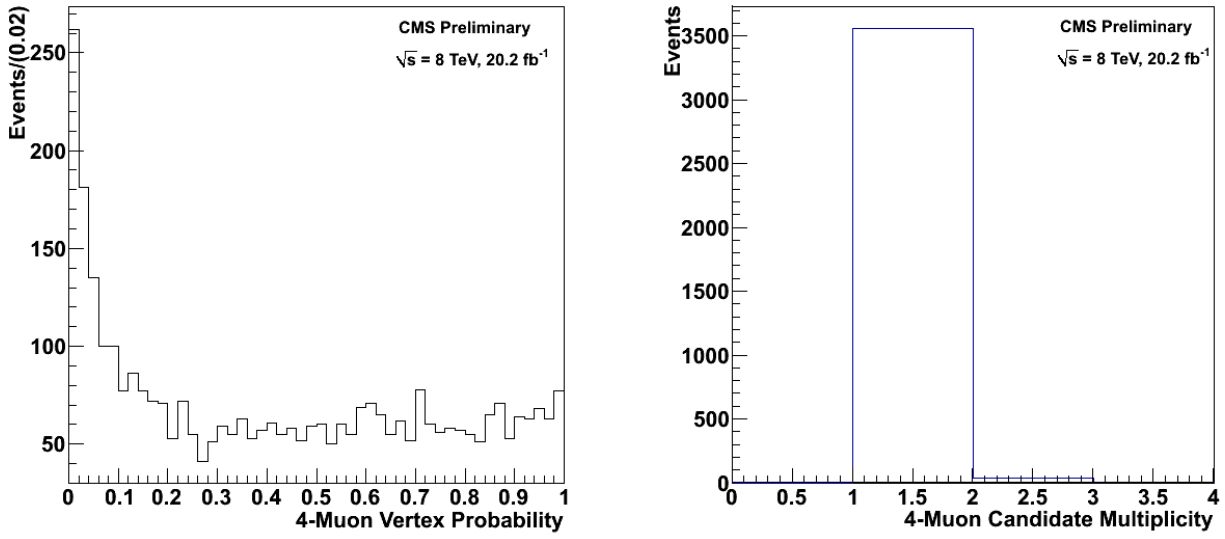
reconstructed muon momentum at vertex and the L3 momentum at vertex are $\Delta R < 0.5$ and $\Delta p_{\mathrm{T}}/p_{\mathrm{T}} < 0.5$.

Both $J/\psi$ pair candidates are fit to a common 4-muon vertex using a Kalman Vertex algorithm and the probability for this fit is required to be greater than 0.5%. Fig. 4.4 (a) shows the distribution of the probability for the $4\mu$ vertex fit in data. In the rare case that there is more than one passing $J/\psi$ pair candidate in an event, the candidate with the highest 4-muon vertex-fit probability is chosen. In 98% of all events only a single candidate is found. Fig. 4.4 (b) shows the number of candidates per event before the choice is made.

This combination of initial selection requirements produces a sample of 3594 4-muon candidates with no more than one per event.

## 4.5 Acceptance Definition

The $J/\psi$ and muon acceptances reflect the geometric coverage of the CMS detector. The acceptance limits are developed based on simulated $J/\psi$ pair events, and the coverage of the muon efficiency tables given in [109].



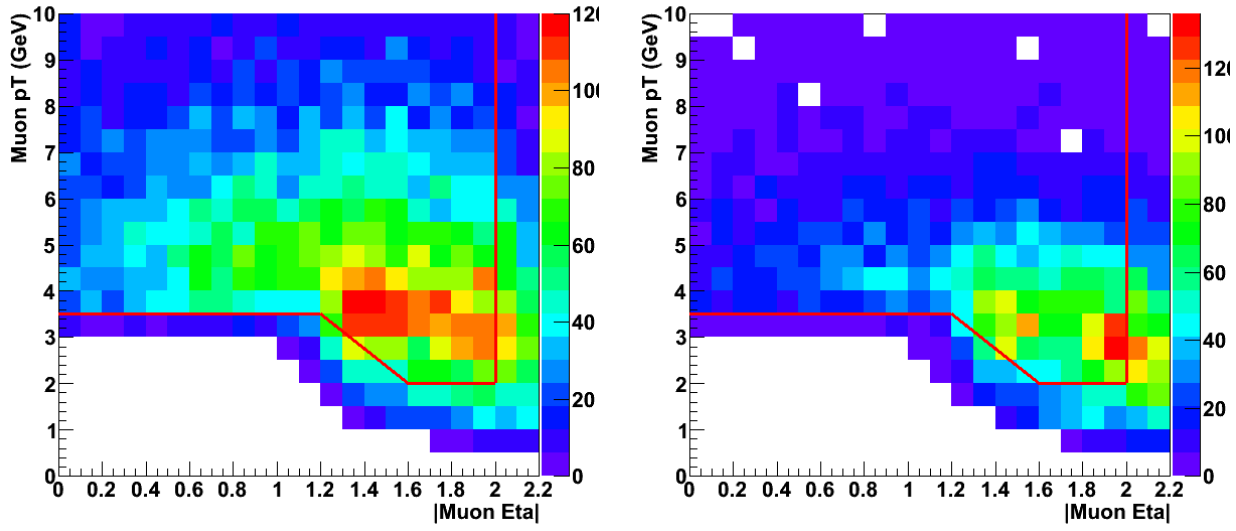

(a) (b)

**Figure 4.4:** The probability distribution from the vertex fit to 4-muon candidates is shown in figure (a). Figure (b) shows the majority of events have only one 4-muon candidates and a small fraction contain 2 passing candidates. Only one candidate per event is chosen.

The single muon acceptance criteria are chosen to ensure that reconstruction and identification efficiency is roughly higher than 50%. The definition of the region in muon transverse momentum $p_{\mathrm{T}}^{\mu}$ and magnitude of pseudo-rapidity $|\eta^{\mu}|$ is listed in Eqn. 4.3.

$$MuonAcceptance \begin{cases} |\eta^{\mu}| \leq 1.2, & p_{\mathrm{T}}^{\mu} \geq 3.5\,\mathrm{GeV}/c \\ 1.2 < |\eta^{\mu}| \leq 1.6, & p_{\mathrm{T}}^{\mu} > (-3.75 * |\eta^{\mu}| + 8) \\ 1.6 < |\eta^{\mu}| \leq 2.0, & p_{\mathrm{T}}^{\mu} \geq 2.0\,\mathrm{GeV}/c \end{cases} \tag{4.3}$$

The requirements are imposed on all four muons in initially selected candidates. The particular "stepped" choice in the middle rapidity region is based on the kinematic distribution of the lowest $p_{\mathrm{T}}^{\mu}$ muon. According to MC simulation this criterion allows a significant increase in the signal yield as compared to constant $p_{\mathrm{T}}^{\mu}$ cuts. The muon kinematic distributions of the reconstructed MC samples are shown in Fig. 4.5 with the chosen muon acceptance shown with a red line.




(a) (b)

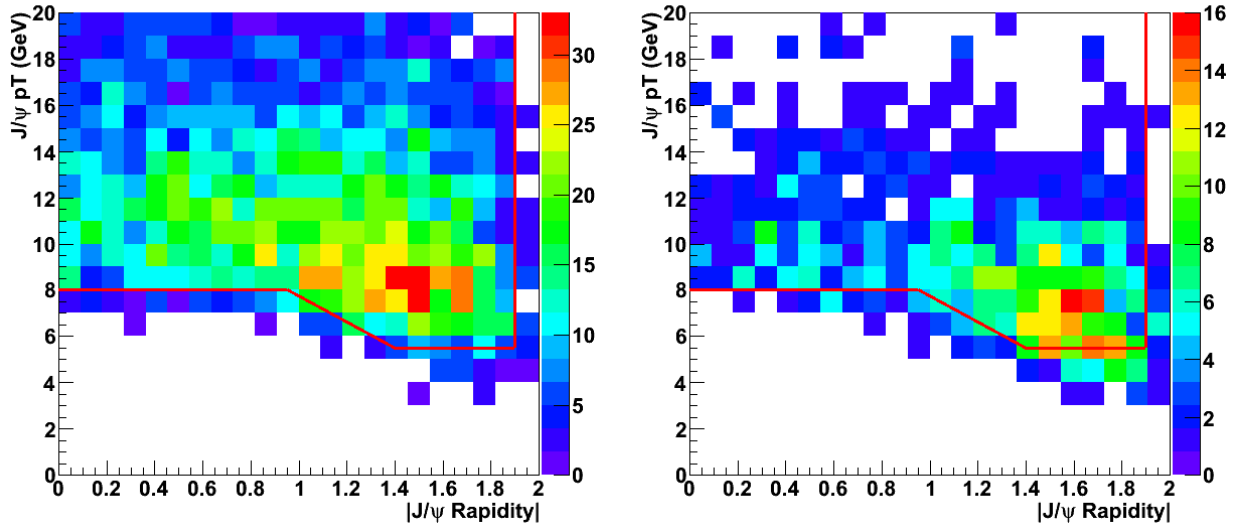
**Figure 4.5:** Plot (a) shows the $|\eta^{\mu}|$ versus $p_{\mathrm{T}}^{\mu}$ distribution for the two decay muons in the reconstructed SPS-NLO MC sample. The muon acceptance used in this analysis is indicated with lines. Plot (b) shows the same for the reconstructed DPS MC sample.

The $J/\psi$ acceptance is in turn constrained by the muon acceptance conditions. The absolute $J/\psi$ rapidity $|y^{J/\psi}|$ versus the transverse momentum $p_{\mathrm{T}}^{J/\psi}$ is shown in Fig. 4.6. The acceptance boundary is indicated by the red line in the figure. It is as inclusive as possible, while avoiding unpopulated bins:

$$J/\psi Acceptance \begin{cases} |y^{J/\psi}| \leq 0.95 & p_{\mathrm{T}}^{J/\psi} > 8.0\,\mathrm{GeV}/c \\ 0.95 < |y^{J/\psi}| < 1.4 & p_{\mathrm{T}}^{J/\psi} > (-5.55 * |y^{J/\psi}| + 13) \\ 1.4 \leq |y^{J/\psi}| \leq 1.9 & p_{\mathrm{T}}^{J/\psi} > 5.5\,\mathrm{GeV}/c \end{cases} \tag{4.4}$$

Four of the kinematic variables used in the measurement of the differential cross section are 4-muon $p_{\mathrm{T}}, |y|$, Mass and the absolute difference in rapidity between the two $J/\psi$ ($\Delta y$). The Pearson Correlation Coefficients [40] measured between these variables are listed in Table 4.3 in data and different model simulations.

From these results it can be seen that 4-muon $p_{\mathrm{T}}$ and $|y|$ are the least linearly correlated of any variable pair.




(a) (b)

**Figure 4.6:** Plot (a) shows the $J/\psi$ $|y|$ versus $p_{\mathrm{T}}$ for the SPS-NLO MC sample after the muon acceptance criteria are applied. The $J/\psi$ requirements are indicated by the red line in the figure. Plot (b) shows the same for the DPS MC sample.

**Table 4.3:** The absolute correlation factors between four 4-Muon kinematic variables are listed for the data sample and compared to the MC samples at reco and gen level. The generator level MC samples are required to be within the $J/\psi$ acceptance.

| Sample | $p_{\mathrm{T}} : \lvert y\rvert$ | $\Delta y : \lvert y\rvert$ | $\Delta y : p_{\mathrm{T}}$ | $Mass : p_{\mathrm{T}}$ | $Mass : \lvert y\rvert$ | $Mass : \Delta y$ |
|---|---|---|---|---|---|---|
| Data | 0.006 | 0.49 | 0.32 | 0.43 | 0.40 | 0.78 |
| DPS reco | 0.005 | 0.83 | 0.005 | 0.13 | 0.73 | 0.88 |
| NLO reco | 0.11 | 0.23 | 0.27 | 0.52 | 0.21 | 0.57 |
| DPS gen | 0.05 | 0.84 | 0.04 | 0.12 | 0.76 | 0.89 |
| NLO gen | 0.17 | 0.3 | 0.26 | 0.43 | 0.24 | 0.61 |

## 4.6 Signal Extraction

In this section an extended Maximum Likelihood Fits (MLF) is used to extract the prompt $J/\psi$ pair yield. The event sample is defined via two selection strategies. The purpose is to determine if a majority of background events can be eliminated with a 10% 4-muon vertex fit probability cutoff. A MLF is a multi-variable fitting technique. A likelihood ($l$) for each event is estimated from event variable distributions for signal and background. The signal and background are assigned PDFs obtained from simulated events, A general expression for the likelihood of an event $j$ is obtained by summing the product of yields $n_i$ and the PDFs $P_i^k$ which include parameterizations of the event variable distributions $k$.

$$l_j = n_{sig}[P^1_{sig} * P^2_{sig}] + n_{bkg}[P^1_{bkg} * P^2_{bkg}] \tag{4.5}$$

An extended likelihood function treats the number of events as a parameter of the fit. The number of events $N$ follows a Poissonian PDF and the best fit is found by maximizing the likelihood function [73]. The product of likelihoods for each event with the Poissonian term in Eqn. 4.6 gives an extended likelihood function $\mathcal{L}$.

$$\mathcal{L} = \frac{e^{-N} N^{N_{obs}}}{N_{obs}!} * \prod_j l_j \tag{4.6}$$

Where $N_{obs}$ represents the number of events observed in the dataset.

Different parameterizations are used for the PDFs. The set of uncorrelated event variables is chosen by eliminating the least significant variables in successive fits. The goodness of fit is obtained from the $\chi^2$ value of the fit to individual variable projections. Several PDFs are tried and the difference in signal yield is taken as systematic uncertainty. A MLF is then validated by throwing simulated datasets according to the PDFs found by the fit and subjecting them to the fit. The likelihood value, yields, and the signal yield pull of several such experiments are compared to the results of the fit to data.

### 4.6.1 Fit to Baseline Sample

After application of the acceptance criteria and limiting the 4-muon invariant mass to 60 GeV/$c^2$ the sample consists of 670 events. An unbinned extended maximum likelihood fit [105] is used to estimate the prompt $J/\psi$ pair contribution. The majority of prompt $J/\psi$ pairs are expected to originate from either single or double parton scattering production. These contributions and background sources in the $J/\psi$ pair final state have been studied in [103] at 7 TeV. The major sources of background were found to include non resonant muon pairs (combinatorial) and non-prompt $J/\psi$ production (B-background). Events containing two $J/\psi$ from different vertices were found to be negligible. Such so called pileup events are strongly suppressed as this analysis requires that all four muons originate from the same vertex with high probability.

Four largely uncorrelated event variables are used to identify background contributions:

- di-muon invariant mass of the higher-$p_{\mathrm{T}}$ $J/\psi$ candidate;
- di-muon invariant mass of the lower-$p_{\mathrm{T}}$ $J/\psi$ candidate;
- the proper decay length of the higher-$p_{\mathrm{T}}$ $J/\psi$ candidate in the transverse plane, $J/\psi_1$, $ct_{xy}$. The $J/\psi$ candidates are considered to originate from secondary vertices. The primary vertex for an event is defined as the origin of charged particle tracks with the highest sum of transverse momentum squared that can be fit to a common position without beam spot constraint. The muons from reconstructed $J/\psi$ candidates are removed from this track sample and the primary vertex is refit. The proper decay length is calculated from the decay length in the laboratory frame $L_{xy} = (\vec{r}_T \cdot \vec{p}_T)/p_T)$, where $\vec{r}_T$ is the vector pointing from the primary vertex to the $J/\psi$ vertex in the transverse plane. Then $ct_{xy} = (m/p_T) \cdot L_{xy}$.
- the separation distance significance between the two $J/\psi$ candidates, $d^{J/\psi}$. It is calculated from the difference in position between the two $J/\psi$ candidates, $\Delta\vec{r}$, and the uncertainty of this distance, $\sigma_{\Delta\vec{r}}$, which includes the uncertainty of the $J/\psi$ vertex given by the Kalman fit and the uncertainty of the muon track fit. It is given as: $d^{J/\psi} = |\Delta\vec{r}|/\sigma_{\Delta\vec{r}}$.

The probability density functions (PDFs) for signal were determined by fitting to DPS and SPS (LO, NLO) MC simulation samples. These shapes were found to be very similar and the SPS-NLO PDF was chosen and then fixed for the fit on data. The PDF functional forms for non-prompt background were obtained from a generic $B$-meson decay sample and earlier fits performed in [103] and combined.

We fit successively to quantify the prompt signal content. In a first step the fit is performed to the sample with the 4-muon vertex probability greater than 0.5% to quantify at higher significance the non-prompt contributions. In the second step we fit a sample with the 10% vertex probability cut and identify residual non-prompt contributions by measuring the residual combinatorial background and signal.

The first step uses the event variables proper decay length and the separation distance significance, as the two $\mu^+\mu^-$ invariant masses provide the least likelihood significance. The likelihood for event $j$ is obtained from Eqn.4.5 using PDFs $P_i(ct_{xy})$ and $S_i(d^{J/\psi})$ from the signal and background categories $i$.

$$l_j = N_{sig}\left(P_{sig}(ct_{xy}) \cdot S_{sig}(d^{J/\psi})\right) + N_{bkg}\left(P_{bkg}(ct_{xy}) \cdot S_{bkg}(d^{J/\psi})\right) \tag{4.7}$$

where $\mathcal{L} = \frac{e^{-N}N^{N_{obs}}}{N_{obs}!} * \prod_j l_j$. The Poisson term is due to the extended nature of the likelihood fit. The yields $N_i$ are determined by minimizing the quantity -ln$\mathcal{L}$,

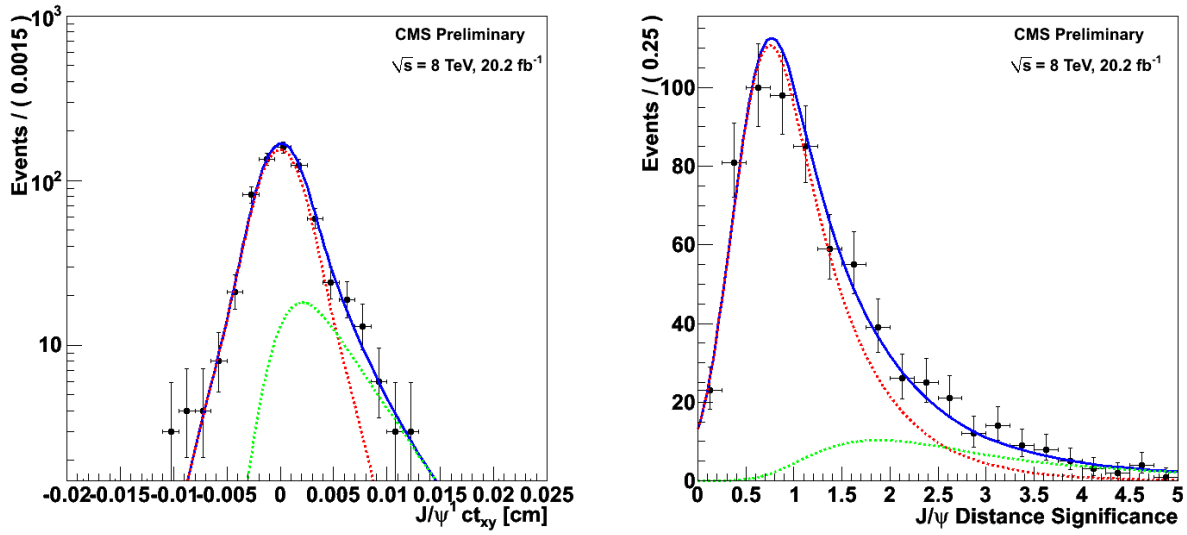
The signal $ct_{xy}$ distribution is parameterized with a double Gaussian resolution function, a dominant core and a smaller and wider tail. The mean and width parameters are obtained from simulation and fixed in the fit. The non-prompt background component is fit by an exponential function convolved with a single Gaussian resolution function (`RooDecay`). The resolution parameters are found to agree with the core resolution of the signal and hence fixed to the same values. The lifetime parameter is left free to float. The significance of the distance $d^{J/\psi}$ between two $J/\psi$ candidates is parameterized with a single Gaussian resolution function convolved with an exponential function for the signal, and a Landau function plus a second degree Chebyshev polynomial for the background. The Landau parameters are obtained from the non-prompt MC and constrained within 2 standard deviations while the polynomial parameters are left free to float. Table 4.4 summarizes the parameterization of

the central fit. The functional forms and parameters were varied to estimate the systematic uncertainty.

**Table 4.4:** The parameters used in the two variable fit to $ct_{xy}$ and Distance Significance for signal (sig) and background (bkg) (G: Gaussian, Exp: Exponential, L: Landau, pol2: Chebyshev polynomial of degree 2).

| Variable | | Shape | Fixed parameters | Floating parameters |
|---|---|---|---|---|
| $ct_{xy}$ | sig | G + G | $m_1^{ct}, m_2^{ct}, \sigma_1^{ct}, \sigma_2^{ct}, f^{ct}$ | - |
| | bkg | G $\otimes$ Exp | $m_1^{ct}, \sigma_1^{ct}$ | $\lambda^{ctb}$ |
| $d^{J/\psi}$ | sig | G $\otimes$ Exp | $m^{dsig}, \sigma^{dsig}, \lambda^{dsig}$ | - |
| | bkg | L + pol2 | $m^{dbkg}, \sigma^{dbkg}$ | $a_0^{dbkg}, a_1^{dbkg}, f^{dbkg}$ |

The fit to the 0.5% vertex cut sample yields $564 \pm 25.4$ signal and $106 \pm 10$ background events. The result of the fit to data with the final function superimposed is shown in Fig. 4.7. The fit was validated by repeatedly generating and fitting samples with the PDFs




(a) (b)

**Figure 4.7:** Maximum likelihood to the event sample with a greater than 0.5% $4\mu$ vertex probability requirement. The distribution of the fit variables $ct_{xy}$ (a) and $d^{J/\psi}$ (b) in data with the result of the fit superimposed. The solid blue line indicates the total fit, the dashed red line the signal and the dashed green line the background distribution.

that were modeled to fit the data. A total of 10,000 such toy experiments are performed. The distributions documenting the toys are displayed in Fig. 4.8. The log-likelihood value

obtained from the fit to data (red line) is in the center of the log-likelihood distribution; no bias is observed in the signal yield from the pull distribution, and the number of measured signal events agrees with the mean of the signal event distribution. The mean signal yield error agrees with the error obtained in the fit.

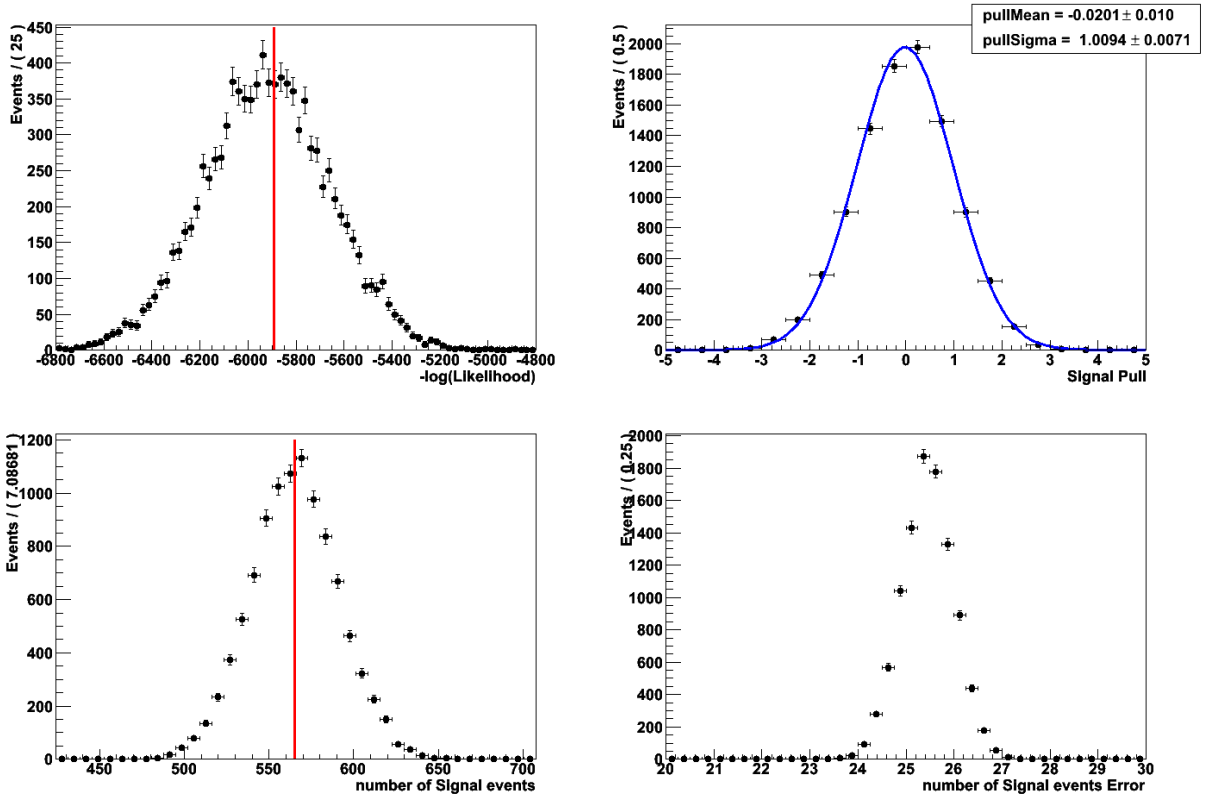


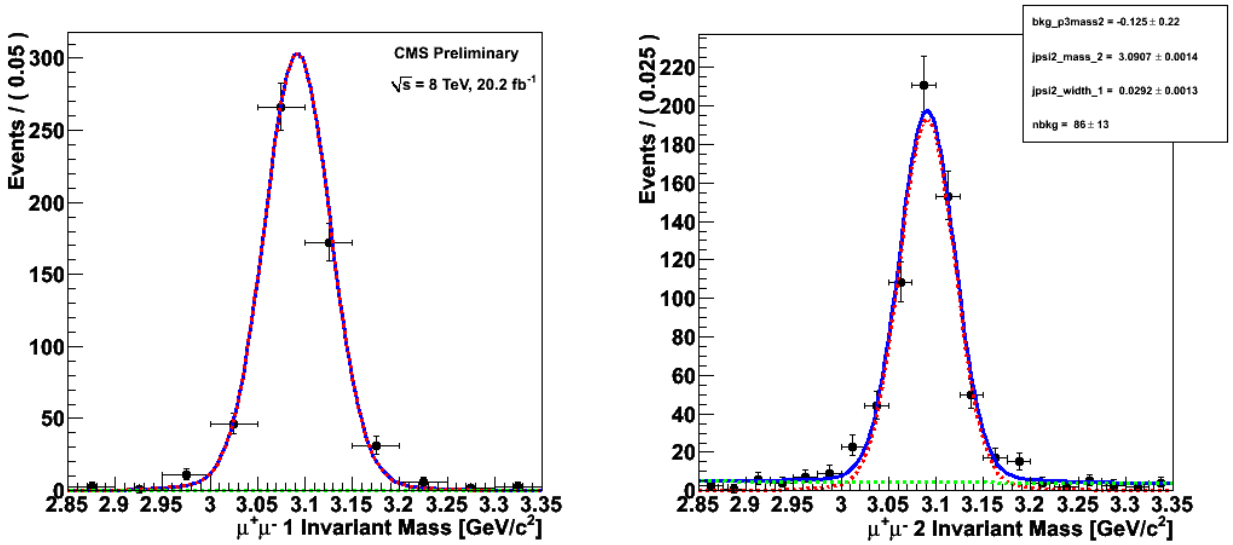

**Figure 4.8:** 10,000 toy MC of the CTxy and DSig fit were generated and refit. The distribution of NLL is shown in the upper left with a line at the NLL value of the main fit, the pull is shown in the upper right. The lower left plot is the distribution of number of signal in each toy with a line at the main fit value. The distribution of the uncertainty of Nsig is the lower right plot.

### 4.6.2 Fit to Final Sample

We inspect the sample after applying a 10% 4-muon vertex probability cut. It consists of 544 candidate events. The sample is expected to be dominated by prompt-prompt $J/\psi$ pair contributions as can be inferred from Fig. 4.10. The figure also shows the result from the maximum likelihood fit described in the previous sub-section applied to this sample.

To estimate the background contribution due to peaking background we revisit the $\mu^+\mu^-$ invariant mass distributions for the two $J/\psi$ candidates in the 0.5% 4-muon vertex probability cut (baseline) data sample (see Fig. 4.9). The distributions are fit separately for signal and background. The signal shape is the sum of two Gaussians with parameters obtained from the MC signal samples.

Combinatorial background contributions are expected to remain flat under the invariant mass distributions, while properly reconstructed non-prompt background from $B$-meson decays is expected to exhibit peaking behavior. Peaking background is difficult to constrain in a fit because the shapes are identical to the shape of the signal. However, the combinatorial background can be extrapolated under the $J/\psi$ peak with a linear or quadratic function and it is mostly constrained by the sideband population. A polynomial of degree 1 and 2 is included in the fit to the $\mu\mu$ invariant mass. No such background contribution is found in a fit to the high-$p_T$ $J/\psi$ shown in Fig. 4.9) (a). Fitting the $\mu\mu$ invariant mass distribution

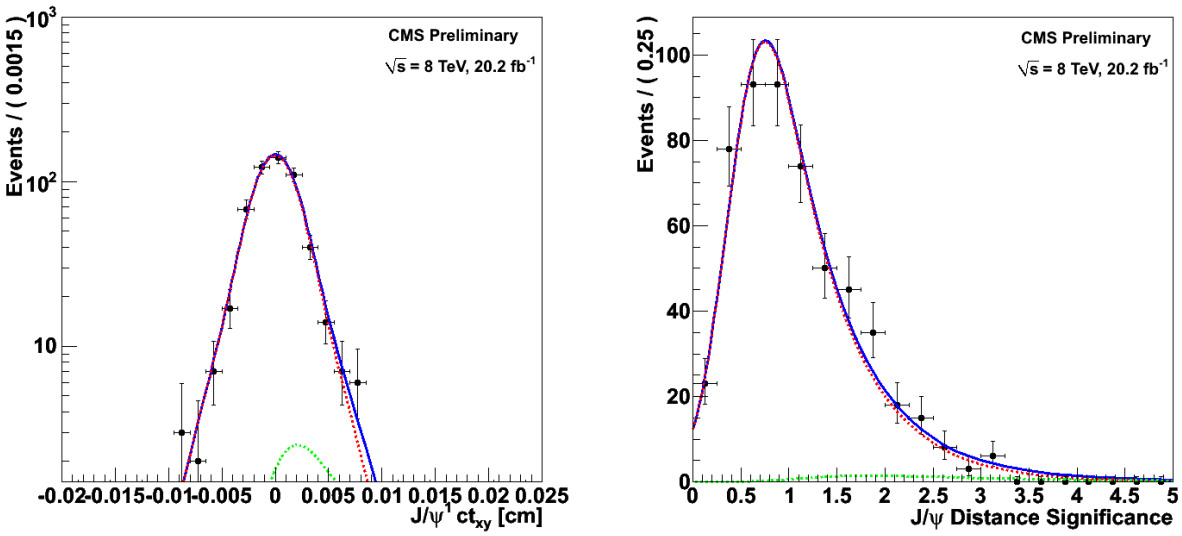



(a) (b)

**Figure 4.9:** (a): The $\mu\mu$ invariant mass distribution of the high $p_{\mathrm{T}}$ $J/\psi$ candidate with a fit superimposed. The signal (red line) agrees with the total fit; the background contribution is invisible. (b): The $\mu\mu$ invariant mass distribution of the low-$p_T$ $J/\psi$ candidate with the fit to signal (red dashed line) and background (green dashed line) superimposed.

for the low $p_{\mathrm{T}}$ $J/\psi$ candidate Fig. 4.9 (b) while fixing the number of signal events and only

allowing the background parameters to float yields 86 background events. Given that the 2-variable fit found 106 background events in total, the remaining peaking background could account for $\approx$ 20 events. In the most pessimistic case, all these events would survive the 10% $4\mu$ vertex probability requirement and remain in the final sample. In this case they constitute only 4% of the signal. However, $B$-background events are more discriminately suppressed by the vertex probability criterion.




(a) (b)

**Figure 4.10:** Maximum likelihood to the event sample with a greater than 10% 4-muon vertex probability requirement. The distribution of the fit variables $ct_{xy}$ (a) and $d^{J/\psi}$ (b) in data with the result of the fit superimposed. The solid blue line indicates the total fit, the dashed red line the signal and the dashed green line the background distribution.

Because of the loss in discriminatory power of the ML fit after applying the 10% 4-muon vertex fit probability criterion, it is abandoned in favor of the fit to $\mu\mu$ invariant mass of the low $p_{\mathrm{T}}$ $J/\psi$ candidate. As can be seen from Fig. 4.9 the $\mu^+\mu^-$ invariant mass of the low $p_{\mathrm{T}}$ $J/\psi$ candidate is not populated outside the central signal region. Hence, only the low $p_{\mathrm{T}}$ candidate is used to estimate the residual background contribution in the sample.

The signal PDF shape for $J/\psi_2$ mass is parameterized with a double Gaussian, and alternatively with the Crystal Ball function [65]. The Gaussians use a common mean, core and tail widths, and a relative fraction. The values of the tail width and the relative fraction

between the core and tail Gaussian are fixed from simulated events. A degree-one Chebyshev Polynomial is used for background shape with one parameter varied freely. Alternatively, a degree-two polynomial is applied. The central parameterization is summarized in Table 4.5.

**Table 4.5:** The parameterization of the one variable Maximum Likelihood Fit.

| Variable | | Shape | Fixed parameters | Floating parameters |
|---|---|---|---|---|
| $m(\mu\mu)$ $J/\psi_2$ | sig | G + G | $\sigma_{tail}, fraction$ | $\sigma_{core}, mean$ |
| | bkg | pol1 | – | $a_0$ |

The fit to the $J/\psi$ shown in Fig. 4.11 converges with $N_{sig} = 483.9 \pm 23.5$ and the $N_{bkg} = 59.1 \pm 11.2$ events. The signal parameters were obtained from the fit to a SPS-NLO sample. The fit is shown on the DPS MC sample for comparison.

For the measurement of the differential cross sections the fit to the low $p_{\mathrm{T}}$ $J/\psi$ invariant mass distribution is used. This variable has the highest significance for the combinatorial background yield. Using only this variable for the fit to samples in bins of different 4-muon production variables reduces systematic uncertainties while the signal statistical significance is only reduced by 5% relative to the fit to the baseline sample.

### 4.6.3 Pileup Dependence

The dependence on pileup is expected to be negligible due to the requirement that all four muons originate from the same vertex with greater than 10% probability. The dependence on pileup was tested by dividing the event sample based on the number of primary vertices ($PvN$) found in each data event. The samples are defined with respect to the mean primary vertex number as low ($PvN < 15$) and high ($PvN \geq 15$) pileup sample. Fig. 4.12 shows the distribution of the number of primary vertices and distributions of different event variables for those samples. The variable distributions for low and high pileup agree within the statistical uncertainties.

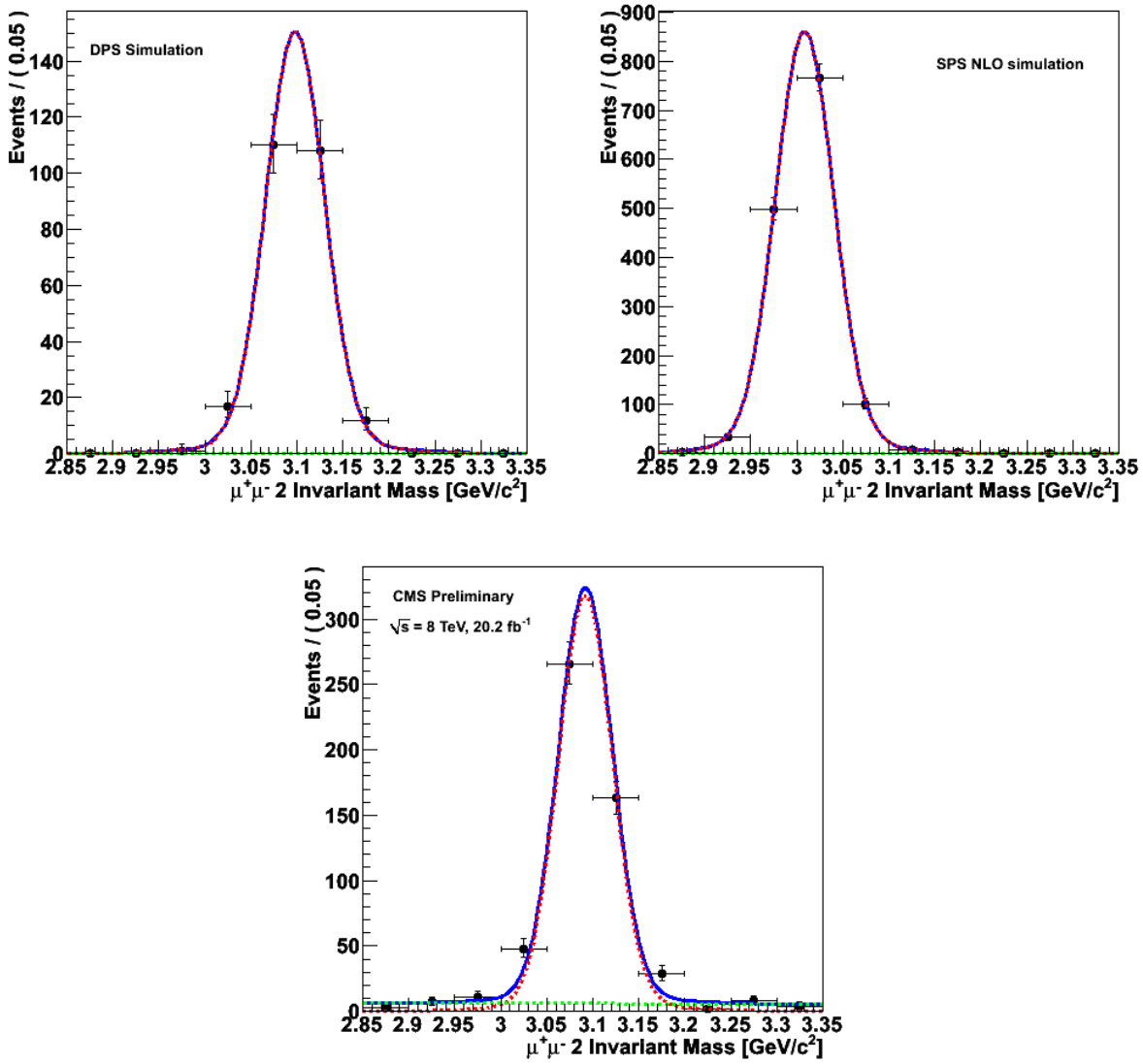



**Figure 4.11:** Signal distribution shown on DPS MC (upper left) SPS-NLO MC (upper right) and signal + background fit shown on the full data sample (lower)

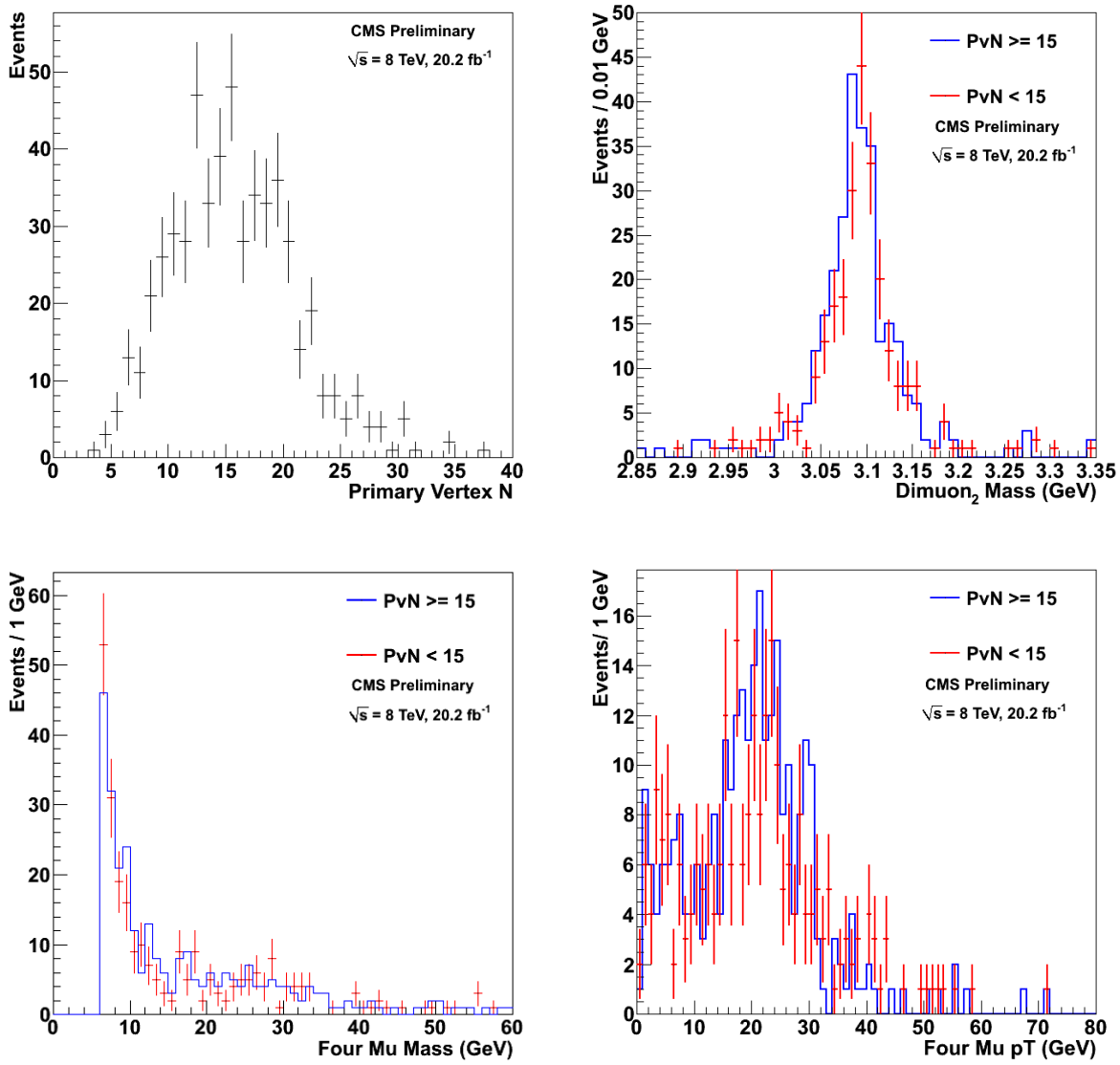



**Figure 4.12:** The distribution of primary vertices in selected events is shown in the upper left. Variable distributions shown split into low pileup ($PvN < 15$ red) and high pileup ($PvN \geq 15$ blue) events shown in the low $p_{\mathrm{T}}$ $J/\psi$ $\mu\mu$ invariant mass (upper right) the 4-Muon invariant mass (lower left) and the 4-muon $p_{\mathrm{T}}$ (lower right).

## 4.7 Acceptance and Efficiency Correction

### 4.7.1 Model Contribution Fit

The correction for muon acceptance within the single $J/\psi$ acceptance region and for trigger, detection, identification efficiencies is obtained from simulated samples. Corrections to the efficiency and uncertainties due differences between data and detector simulation are obtained from single muon efficiencies utilizing the Tag&Probe Technique [100]. To ensure that the topological and kinematic distributions in data are closely matched by the simulated samples we perform a fit with different models to the 4-muon event variables $p_{\mathrm{T}}$ and $|y|$ that are least correlated (see Table 4.3). It has been shown on $pp$ collision data at 7 TeV [103, 82] that a combination of SPS-NLO and DPS production events is a close match to data. In a first step we perform a fit with reconstructed events simulated with three models, SPS-LO, SPS-NLO, and DPS, to reconstructed data with floating relative fraction. The fitted mix is then used to estimate the total acceptance times efficiency correction $\omega$ in each sample as:

$$\omega = \frac{N_{reco}}{N_{gen}} \tag{4.8}$$

with $N_{reco}$ the number of events surviving muon quality and acceptance criteria from an initial sample of $N_{gen}$ $J/\psi$ pair events generated within the single $J/\psi$ acceptance. The value of the acceptance correction, and the total acceptance times efficiency correction is shown in Fig. 4.13 for DPS and Fig. 4.14 for NLO.

Events generated according to the three production models SPS-LO, SPS-NLO, and DPS and subjected to the full detector simulation are reconstructed and selected with the identical requirements as the data. Event distributions of these samples are normalized to the total number of data events and added with two relative fractions requiring that the sum of the models adds to the total number of events in data. These fractions are varied in a chisquare fit to histograms of the event variables , absolute 4-muon rapidity $|y|$ and 4-muon transverse momentum $p_{\mathrm{T}}$. The best fit result is shown in Fig. 4.15. It yields 13% relative DPS contribution and 87% SPS-NLO contribution while the SPS-LO contribution fits to

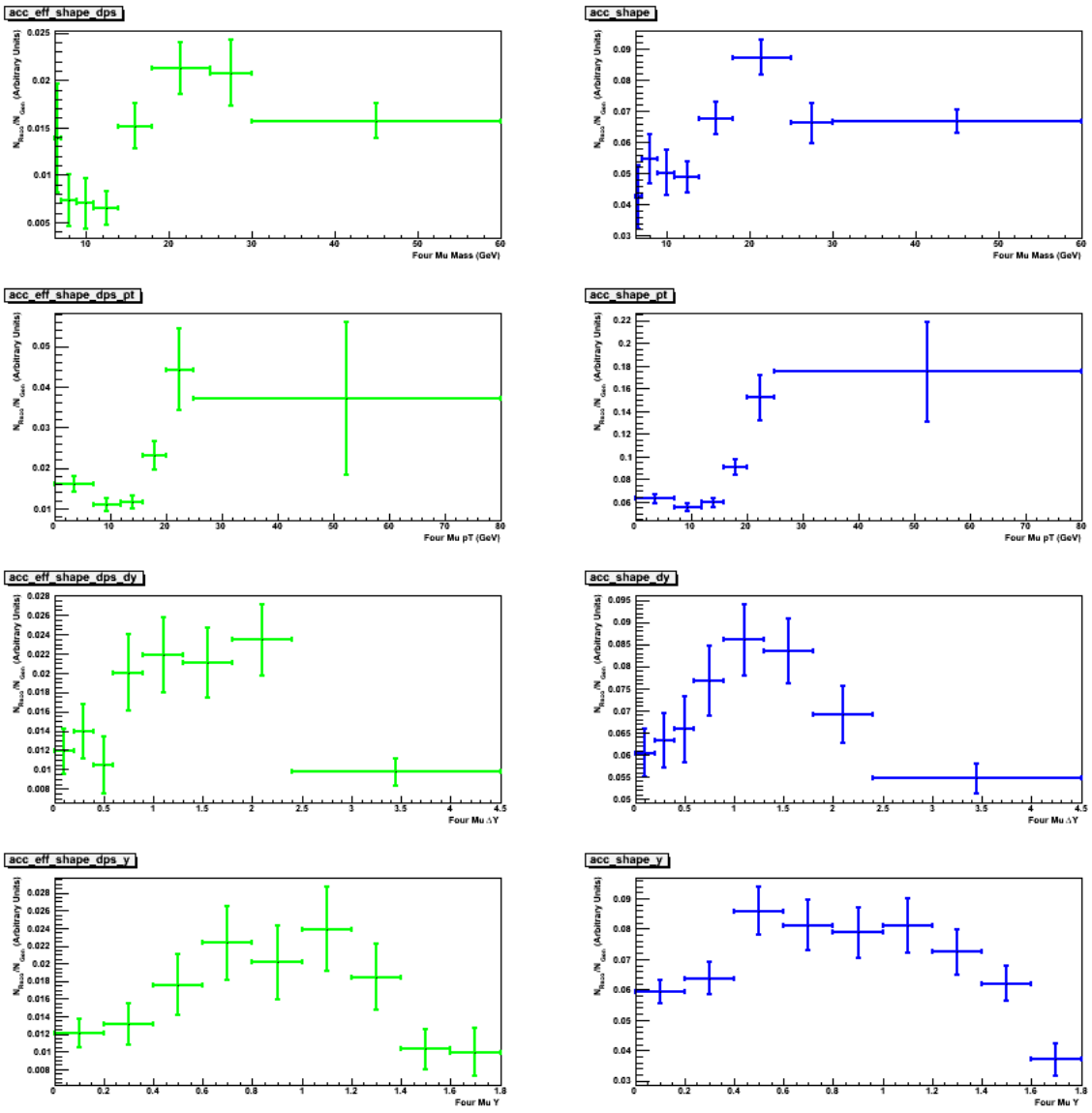



**Figure 4.13:** The left column shows the acceptance× efficiency correction in bins of several $J/\psi$ pair production variables obtained with the DPS MC simulation sample, the right column shows the corresponding acceptance correction, only.

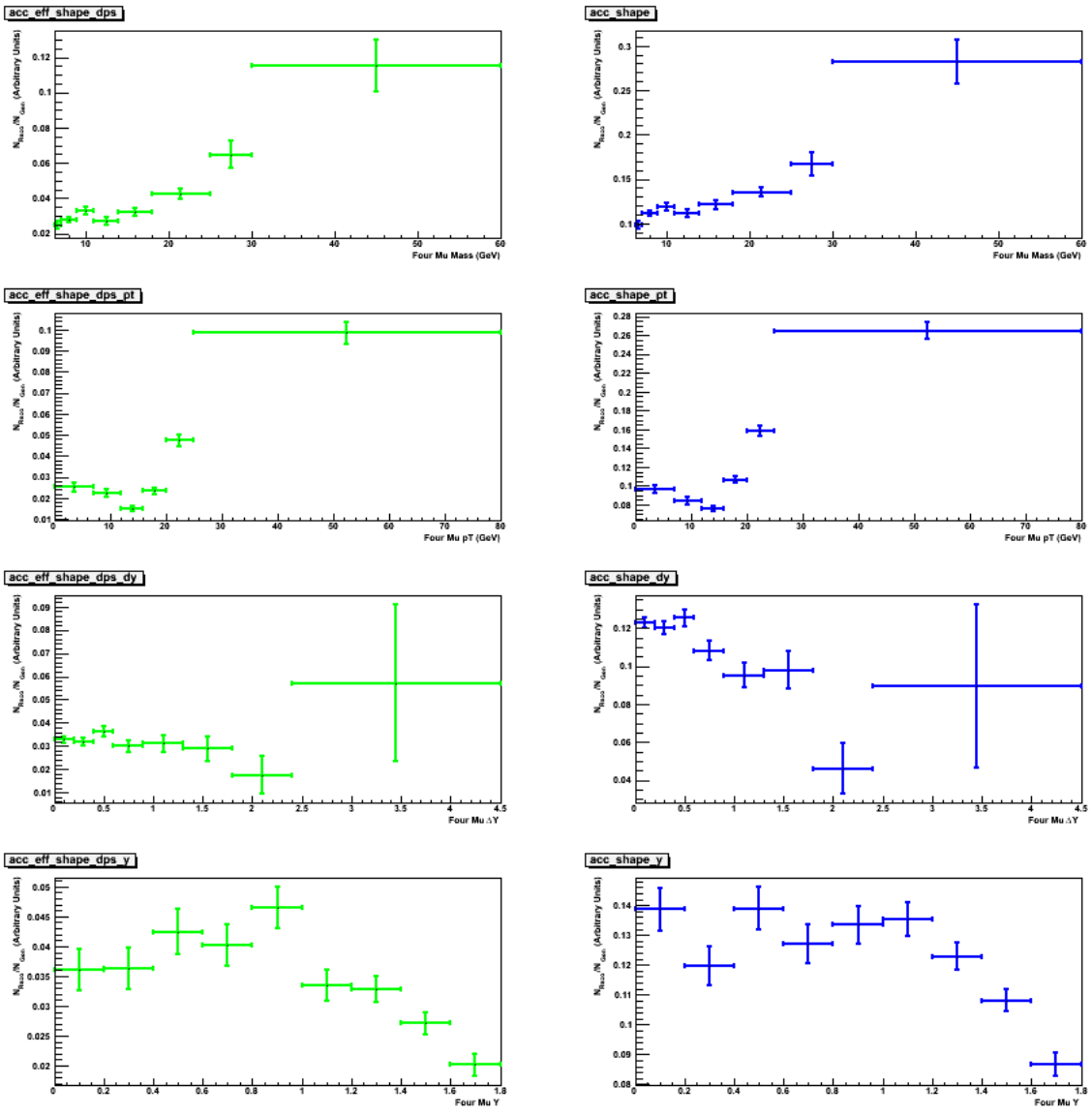



**Figure 4.14:** The left column shows the acceptance× efficiency correction in bins of several $J/\psi$ pair production variables obtained with the SPS-NLO MC simulation sample, the right column shows the corresponding acceptance correction, only.

0%. The fit is also shown on the 4-muon mass and the absolute rapidity difference between the $J/\psi$, however these distributions did not contribute to the chisquare calculation.

Acceptance times efficiency corrections are obtained separately from the different models. The global fraction is used to obtain the weighted average of the correction in each bin of the cross section variables. To account for the uncertainty in the relative contributions the DPS fraction is varied from 13% by absolute ± 5% corresponding to a relative change of about 40%. This is accounted for as systematic uncertainty.

### 4.7.2 Single Muon Efficiency

The efficiency correction for trigger and reconstruction relies on detector simulations. Therefore, additional studies are necessary to quantify the difference with a data based efficiency correction method. The latter, the Tag&Probe method, utilizes the well known $J/\psi \rightarrow \mu^+\mu^-$ decay reconstructed from simulation and data samples. A well identified muon, the so-called Tag, is combined with a second track in the event, called the Probe, that underwent specific selection steps. The Tag-Probe pairs are divided into two samples based on whether the probe satisfies criteria for the efficiency to be measured or not. The two corresponding Tag-Probe invariant mass distributions are then fit simultaneously for their $J/\psi$ signal content with a maximum likelihood fit resulting in a pass and fail yield. The efficiency is the ratio of number of passed $J/\psi$ divided by total number of $J/\psi$ in that step.

The total single muon efficiency $\epsilon_\mu$ is the product of several efficiencies where each one is exclusively defined relative to the previous selection step. The order of the efficiency steps has been defined by the MUON POG [100], and follows the sequence:

$$\epsilon_\mu = \epsilon_{track} \cdot \epsilon_{ID} \cdot \epsilon_{Quality} \tag{4.9}$$

- $\epsilon_{track}$: the track reconstruction efficiency, which has been found to be 99% or higher [53].
- $\epsilon_{ID}$: the muon identification efficiency, which is the probability that the reconstructed tracker track is identified as muon by the muon system.

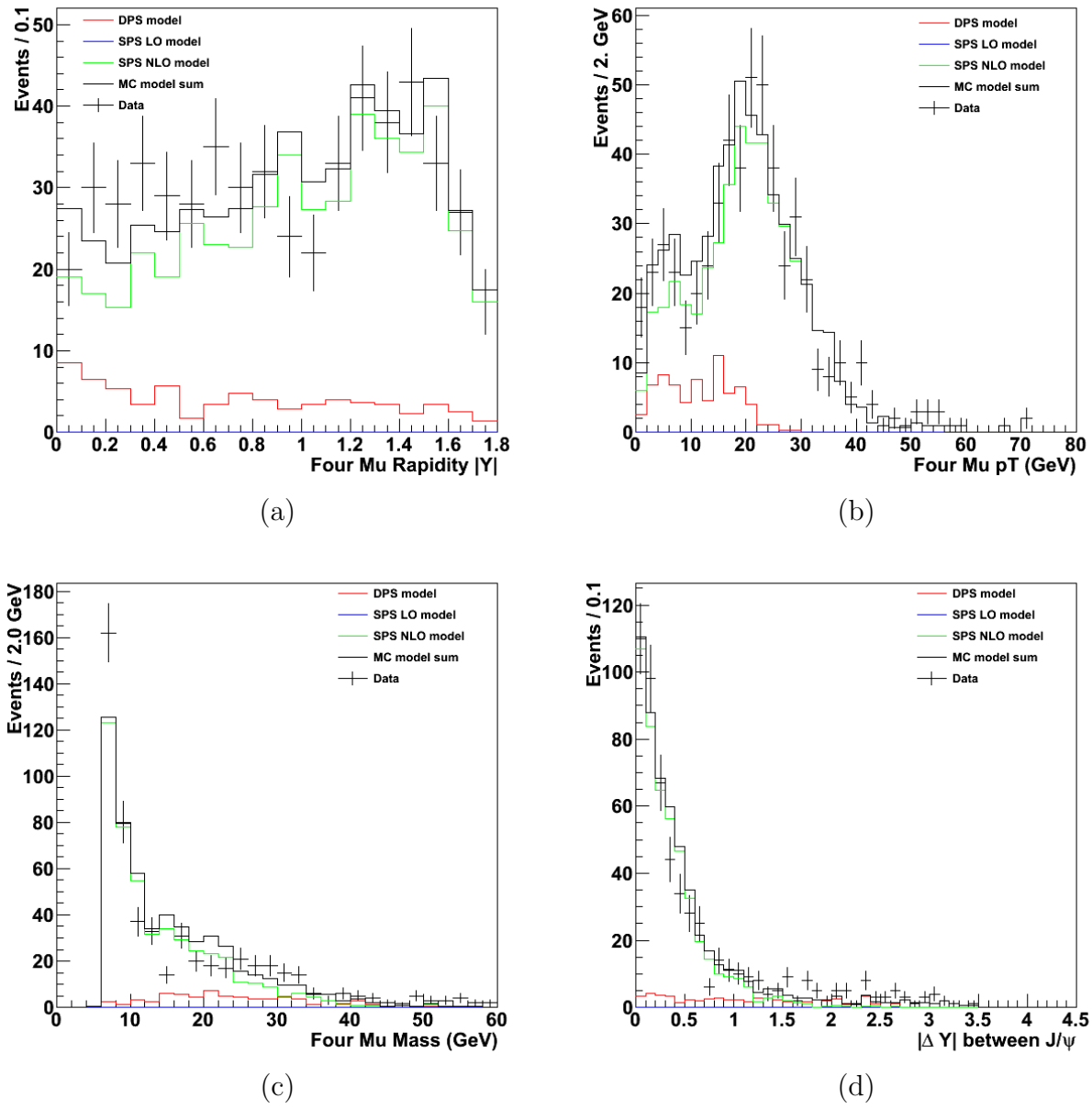



**Figure 4.15:** Distributions of 4-muon event variables (a) absolute rapidity, (b) transverse momentum, (c) invariant mass, and (d) absolute difference of the two $J/\psi$ candidate rapidities in data (error bars), with SPS-NLO (green histogram) and DPS (red histogram) simulated sample contributions according to the chisquare fit. The black histogram is the sum of the models.

- $\epsilon_{Quality}$: the efficiency for a muon to pass the quality requirements outlined in Sec. 4.4, Table 4.2.

The efficiency for a candidate event $\epsilon$ is derived as the product of the four single muon efficiencies times an efficiency that the event passed the trigger, $\epsilon_{HLT}$, that is evaluated at the HLT level also from single muon efficiencies:

$$\epsilon = \epsilon_{HLT} \cdot \prod_{i=1}^{4} \epsilon_{\mu_i} \tag{4.10}$$

The single muon efficiencies were available from lookup tables in terms of muon $p_{\mathrm{T}}$ and $\eta$ for data and simulation [109].

The trigger path requires at least three muons to be found at the L3 stage, and two oppositely charged muons must fit to a common vertex with a probability greater than 0.5%. The dimuon invariant mass must be in the range $2.85 \leq M^{\mu\mu} \leq 3.35$. The single muon HLT efficiency is determined as product of the L1·L2 and L3 trigger efficiencies. The per event HLT efficiency is calculated from the single muon HLT efficiencies $\epsilon^{\mu_i}_{HLT}$ (i=1,2,3,4 muon index) and di-muon vertexing efficiency $\epsilon_{vtx}$ as follows:

$$\begin{aligned}
\epsilon_{HLT} = {} & \epsilon^{\mu_1}_{HLT} \cdot \epsilon^{\mu_2}_{HLT} \cdot \epsilon^{\mu_3}_{HLT} \cdot \epsilon^{\mu_4}_{HLT} \cdot (2 \cdot \epsilon_{vtx} - \epsilon_{vtx} \cdot \epsilon_{vtx}) \\
& + \epsilon^{\mu_1}_{HLT} \cdot \epsilon^{\mu_2}_{HLT} \cdot \epsilon^{\mu_3}_{HLT} \cdot (1 - \epsilon^{\mu_4}_{HLT}) \cdot \epsilon_{vtx} \\
& + \epsilon^{\mu_1}_{HLT} \cdot \epsilon^{\mu_2}_{HLT} \cdot (1 - \epsilon^{\mu_3}_{HLT}) \cdot \epsilon^{\mu_4}_{HLT} \cdot \epsilon_{vtx} \\
& + \epsilon^{\mu_1}_{HLT} \cdot (1 - \epsilon^{\mu_2}_{HLT}) \cdot \epsilon^{\mu_3}_{HLT} \cdot \epsilon^{\mu_4}_{HLT} \cdot \epsilon_{vtx} \\
& + (1 - \epsilon^{\mu_1}_{HLT}) \cdot \epsilon^{\mu_2}_{HLT} \cdot \epsilon^{\mu_3}_{HLT} \cdot \epsilon^{\mu_4}_{HLT} \cdot \epsilon_{vtx} \ .
\end{aligned} \tag{4.11}$$

The first line in the above equation represents the efficiency for all four muons to be found by the HLT, with two of them fit to a common vertex. The four following lines represent the efficiency for all possible combinations of three muons found in the HLT and the fourth muon explicitly not in the HLT. The $J/\psi$ vertexing efficiency, $\epsilon_{vtx}$ of the HLT is adopted from the Tag&Probe study [109].

It should be noted that there is also an offline $J/\psi$ vertex fit requirement based on the fit probability. In the simulated signal samples the likelihood to successfully fit both vertices in an event is greater than 99%. Therefore, the offline event reconstruction efficiency is considered to be the product of muon reconstruction efficiencies only.

To arrive at an uncertainty and correction in the comparison data versus MC simulation the efficiencies are calculated from the Tag&Probe tables obtained from data ($\epsilon^{data}$), and from Tag&Probe tables obtained from Monte Carlo simulation ($\epsilon^{MC}$) [109]. The superscript refers to the origin of the table. The tables are evaluated either with the selected events in data or a sample consisting of a mixture of DPS and SPS-NLO according to the model contribution fit in Sec. 4.7.1. The distribution of the difference ($\epsilon^{data} - \epsilon^{MC}$) for data events is shown in Fig. 4.16 as data points. The plot also shows the distribution of the difference for the model simulation sample as histogram, normalized to the amount of events in data. The difference distributions agree between data and Monte Carlo events. The event efficiencies computed using the MC Tag&Probe tables are systematically underestimated when compared to data. Therefore, the event efficiency in Eqn. 4.8 in each bin of different event variables is multiplied by the factor $\kappa = 1 + 0.5 \cdot (\epsilon^{data} - \epsilon^{MC})/\epsilon^{MC} = 1 + \Delta$. The efficiency is varied by the shift ($\pm\Delta$) to estimate the systematic uncertainty of the cross section.

## 4.8 $J/\psi$ Polarization

The $J/\psi$ spin vector alignment with respect to the direction of flight is called polarization and influences the angular distribution of the decay muons. This changes the muon acceptance correction of the $J/\psi$ candidates. The $J/\psi$ pair production cross section is measured assuming that both $J/\psi$ are unpolarized. The muon helicity angle $\theta$ is defined as the angle between the positive muon direction in the rest frame of the $J/\psi$ with respect to the $J/\psi$ direction in the 4-muon center of mass frame. The distribution of $\theta$ is given as [50]:

$$w(\theta) \propto 1 + \lambda cos^2\theta \tag{4.12}$$

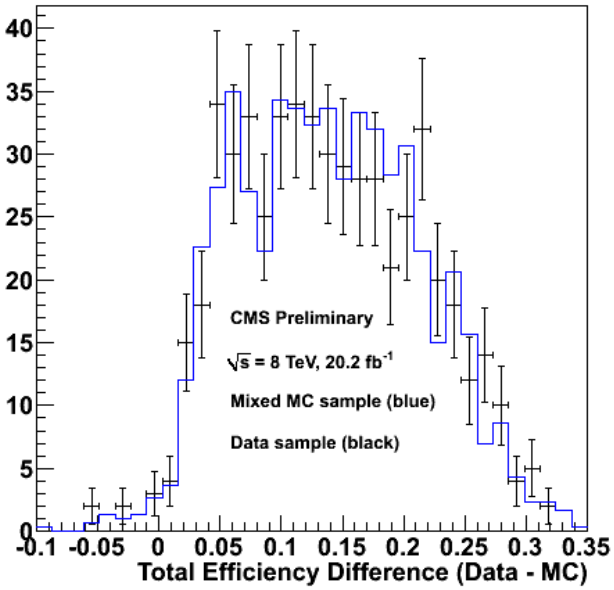



**Figure 4.16:** The difference of the event efficiency between the T&P tables from data and MC simulation ($\epsilon^{data} - \epsilon^{MC}$), evaluated with the selected data sample (data points) and with the reconstructed MC sample composed of 13% DPS events and 87% SPS-NLO events (blue histogram).

where is a polarization observable. $\lambda = +1$ corresponds to longitudinal polarization, $\lambda = -1$ corresponds to transverse polarization and $\lambda = 0$ corresponds to a uniform muon distribution. The polarization coefficient $\lambda$ for single $J/\psi$ mesons has been measured close to zero [50, 48, 22, 9, 21]. We vary this parameter by $\pm 20\%$, a reasonable envelope of the aforementioned measurements, to estimate the effect on the cross sections. Both $J/\psi$ are assumed to have the same polarization as this results in the largest deviation from the unpolarized case. We generate the decay muons according to the expected angular distribution repeatedly (10,000 times per event) and then apply the muon acceptance criteria. The acceptance for an event is given by the number of candidates within the acceptance divided by the number of generations. We find that in any scenario the acceptance changes uniformly in the 4-muon variables. This is demonstrated in Fig. 4.17 and in Fig. 4.18 for variable distributions according to the DPS and the SPS-NLO models respectively. The uniformity is shown using data in Fig. 4.19. The relative change in the fiducial cross section in all three samples with respect to the case of unpolarized $J/\psi$ ($\lambda = 0$) is found to be +11.4% for 20% longitudinal ($\lambda = +0.2$) and -11.1% for 20% transverse polarization ($\lambda = -0.2$).

For the extreme case $\lambda = +1$ the relative change of the cross section is +62%, and for $\lambda = -1$ it is -50%. With the available data both cases are difficult to distinguish in the helicity angle distribution within the CMS acceptance. The distribution of the angle $\theta$ for the extreme scenarios is shown in Fig. 4.20.

## 4.9 Systematic Uncertainties

The uncertainty of the cross section is a combination of several contributions which are listed below and summarized in Table 4.6.

1. **Efficiency:** The efficiency is obtained from Monte Carlo simulation. To estimate the uncertainty due to differences between data and MC, the efficiencies for both are calculated from Tag&Probe tables as described in Sec. 4.7. The efficiency is varied by half of the difference between the data and MC efficiency in each bin of the event variables and the corresponding change of the cross section is adopted as systematic uncertainty.

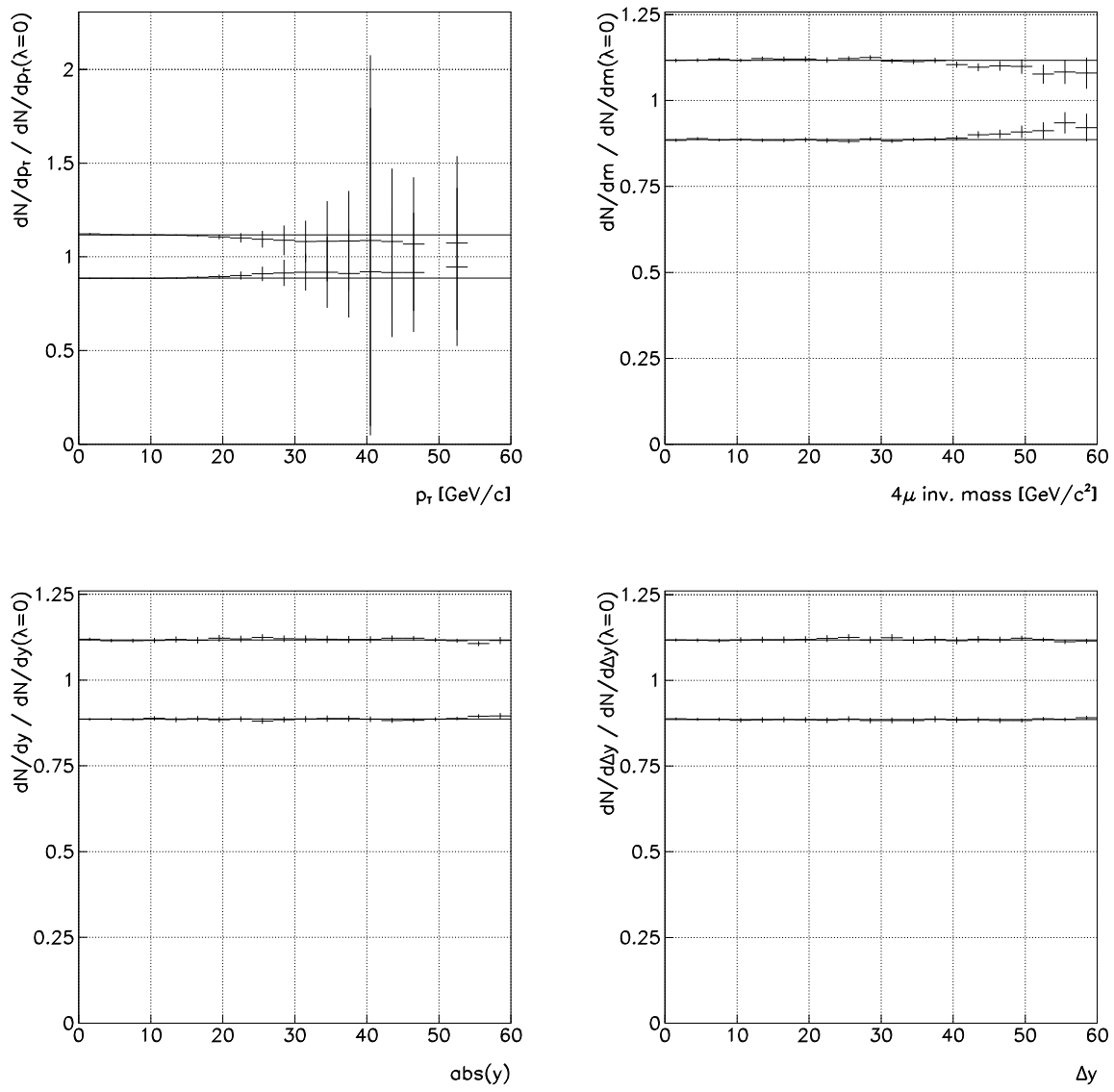



**Figure 4.17:** Ratios of acceptance corrected simulated DPS event distributions in 4-muon variables for different assumption of $J/\psi$ polarization. The two ratios in each plot correspond to $\lambda \pm 0.2$ and have been fit to straight lines that are superimposed to the plot.

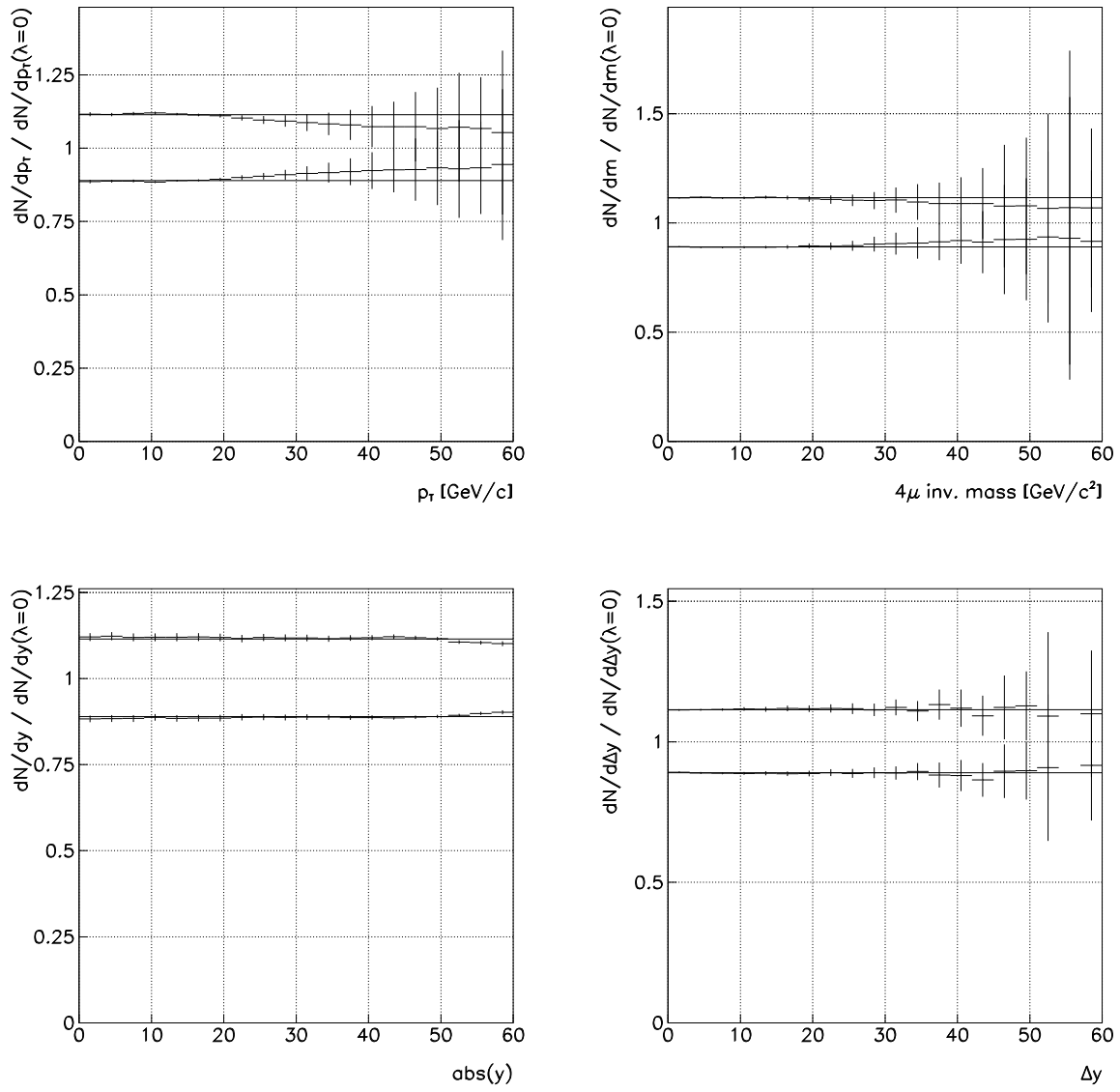



**Figure 4.18:** Ratios of acceptance corrected simulated SPS-NLO event distributions in 4-muon variables for different assumption of $J/\psi$ polarization. The two ratios in each plot correspond to $\lambda \pm 0.2$ and have been fit to straight lines that are superimposed to the plot.

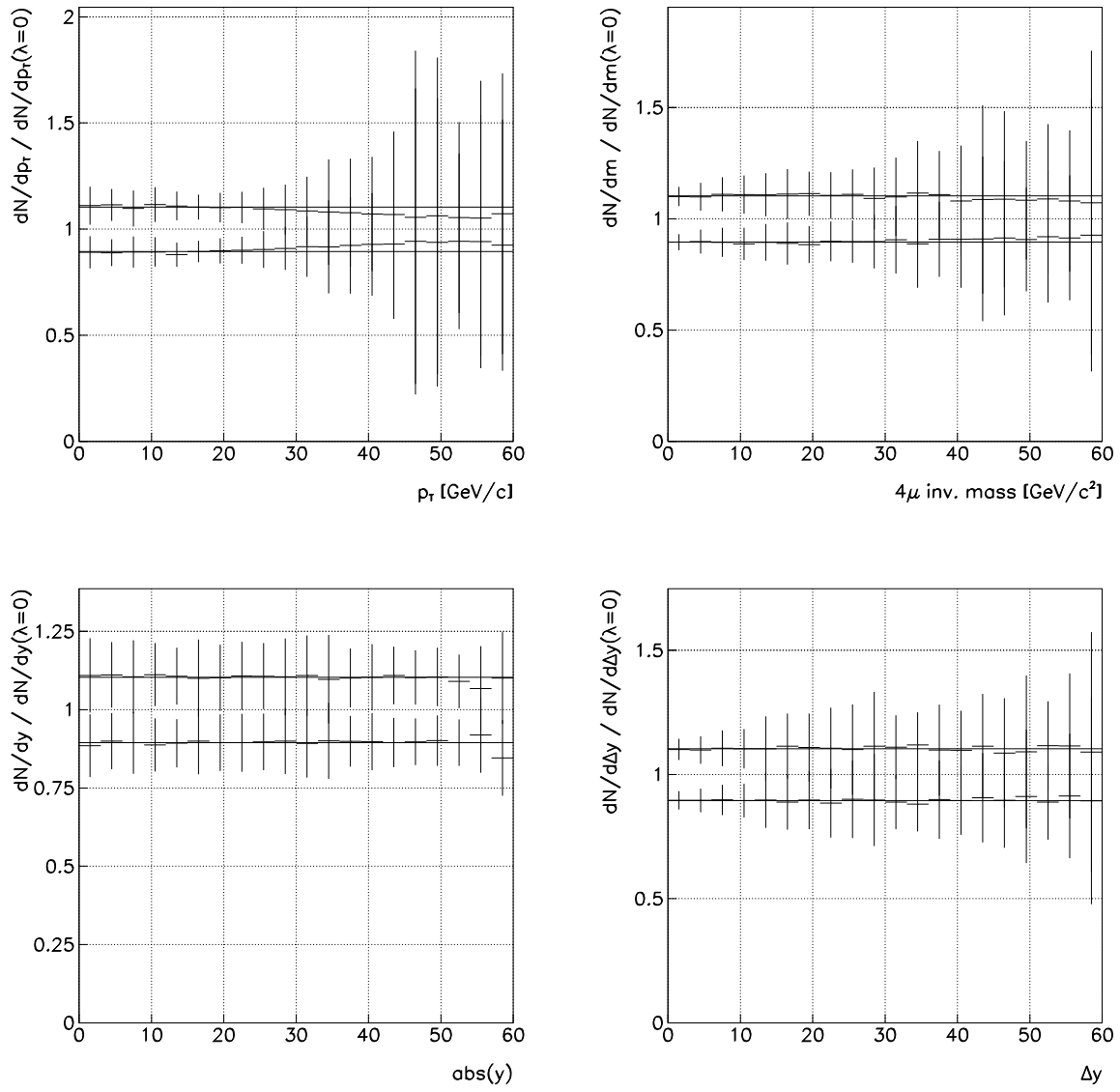



**Figure 4.19:** Ratios of acceptance corrected simulated data event distributions in 4-muon variables for different assumption of $J/\psi$ polarization. The two ratios in each plot correspond to $\lambda \pm 0.2$ and have been fit to straight lines that are superimposed to the plot.

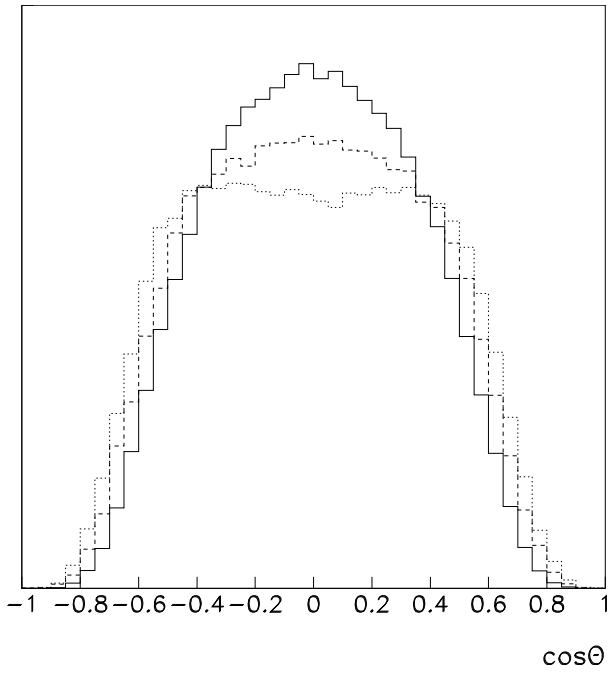



**Figure 4.20:** Normalized distributions of the angle $\theta$ between the positive decay muon momentum in the rest frame of the $J/\psi$ and the direction of flight of the $J/\psi$ in the laboratory frame for different assumptions for $\lambda$, within the CMS muon acceptance. The height of the distributions at $\cos\theta = 0$ increases in the order $\lambda = +1, 0, -1$.

2. ***J/ψ* Acceptance:** The $J/\psi$ acceptance limits in $p_{\mathrm{T}}^{J/\psi}$ (Eqn. 4.4) were varied by $\pm 150\,\mathrm{MeV}$ with respect to the quoted values, and any difference in the signal yield in the respective samples is accounted for as systematic uncertainty.

3. **Model Contribution Fit:** The reconstructed MC samples were fit to data to determine the relative contribution of DPS, SPS-LO and SPS-NLO in each bin of the cross section measurements. The fit resulted in no contribution from the SPS sample. The difference in cross section calculated by varying the absolute fraction of DPS by $\pm 5\%$ is accounted for as a systematic uncertainty.

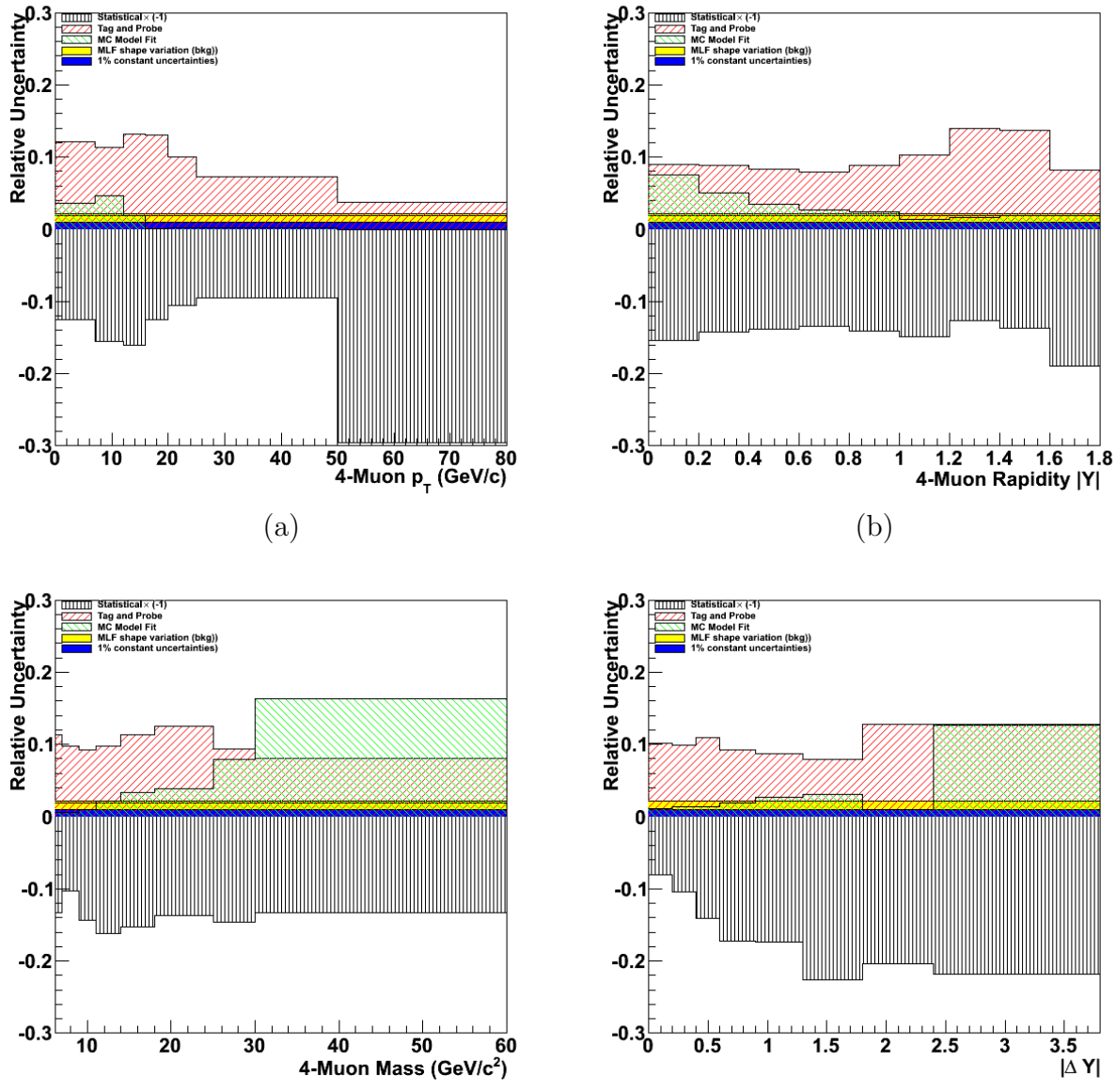
4. **Maximum Likelihood Fit:** The shapes used in the maximum likelihood fit were adjusted on both data and MC samples. A double Gaussian signal shape and a one parameter Chebyshev polynomial were used in the final fit, however other shapes were tested and the difference in signal yield is accounted for as systematic uncertainty. Alternatively to the Gaussian fit a Crystal Ball function [65] was applied for the signal shape, and a two parameter Chebyshev polynomial for the background shape.

**Table 4.6:** The summary of relative systematic uncertainties in the differential cross section measurements. The values with ranges show the highest and lowest systematic uncertainty for the 8 variables. The rows without ranges indicate that the systematic uncertainty is kept constant for all bins and all variables. The uncertainty on the branching fraction and luminosity are kept separate from the other uncertainties for the measurement, and not included in the differential plots.

| Source | Relative Uncertainty [% ] |
|---|---|
| Efficiency | 10.0 - 10.7 |
| $J/\psi$ Acceptance | 1.9 |
| Model Contribution Fit | 0.5 - 4.2 |
| ML Fit Signal | 1.0 |
| ML Fit Background | 2.2 |
| Branching Fraction | 1.2 |
| Luminosity | 2.6 |

5. **Branching Fraction and Luminosity:** The $J/\psi \rightarrow \mu^+\mu^-$ branching fraction uncertainty is given by the world average of measurements [90]. The uncertainty in the integrated luminosity for the 2012 run is given by [54]. These values are not included in the differential cross section plots and are listed separately in Table 4.6.

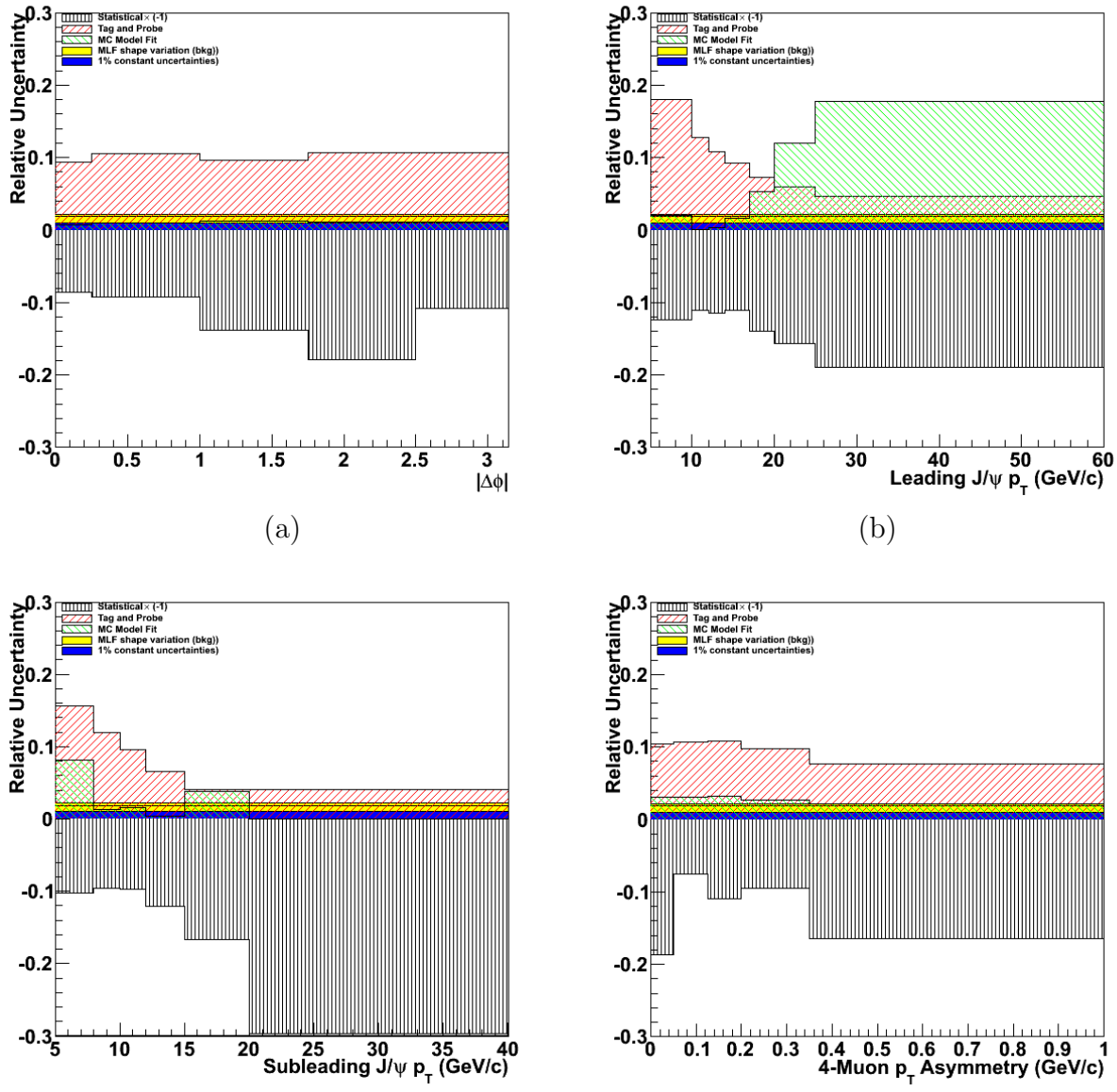
The systematic and statistical uncertainty contribution to each bin of the 8 differential cross section measurements can be seen in Fig. 4.21 and Fig. 4.22. Table 4.6 lists the smallest - largest systematic uncertainty due to each source from the 8 variables.




(a) (b)

(c) (d)

**Figure 4.21:** The uncertainties of each bin of the cross section, statistical is shown negative for clarity. (a) transverse momentum, (b) the absolute value of the rapidity, (c) invariant mass, and (d) the absolute difference in rapidity between the two $J/\psi$.




(a) (b)

(c) (d)

**Figure 4.22:** The uncertainties of each bin of the cross section, statistical is shown negative for clarity. (a) the delta phi between $J/\psi$, (b) the transverse momentum of the higher $p_{\mathrm{T}}$ $J/\psi$, (c) the transverse momentum of the lower $p_{\mathrm{T}}$ $J/\psi$, and (d) the asymmetry between the two $J/\psi$ $p_{\mathrm{T}}$.

## 4.10 Cross Section Measurement

The differential cross section can be measured across a distribution of variable "x" using the formula:

$$\frac{d\sigma}{dx} = \frac{N_{events}}{\omega * (BF_{J\to\mu\mu})^2 * Lumi * \Delta x} \tag{4.13}$$

where $\omega$ is the total acceptance X efficiency in a particular bin of width $\Delta x$, $N_{events}$ is the number of signal events in the bin after the fit to the $J/\psi_2$ mass, and BF is the branching fraction of $J/\psi \to \mu\mu$ .

The differential result in each distribution along with the statistical and systematic uncertainties and the uncorrected number of signal events found by the MLF to the low $p_{\mathrm{T}}$ $J/\psi$ are shown in Tables 4.7-4.14 .

The total cross section is determined by integrating the differential cross sections in the full range of the measurements in $p_{\mathrm{T}}^{JJ}$ and $|y^{JJ}|$.

$$p_{\mathrm{T}}^{JJ} : \sigma(pp \to J/\psi J/\psi) = \qquad 192.2 \pm 10.9 \pm 21.1 \text{ pb} \tag{4.14}$$

$$|y^{JJ}| : \sigma(pp \to J/\psi J/\psi) = \qquad 199.1 \pm 9.9 \pm 22.5 \text{ pb} \tag{4.15}$$

The uncertainties listed are statistical first, then systematic. The total cross section is the average of the two measurements. The highest relative statistical and systematic uncertainty among the measurements is adopted for the final result:

$$\sigma_{fid}(pp \to J/\psi J/\psi) = 195.7 \pm 11.1\ (stat) \pm 22.1\ (syst) \pm 5.1\ (lumi) \pm 2.3\ (BF) \text{ pb} \tag{4.16}$$

The uncertainties due to luminosity and branching fraction are not included in the differential cross section plots.

In a first step, the DPS cross section is derived with a chisquare fit of the generated distributions for DPS and SPS-NLO according to [95] to the measured differential cross sections. Hence, this extraction relies on the predicted variable distributions, not absolute

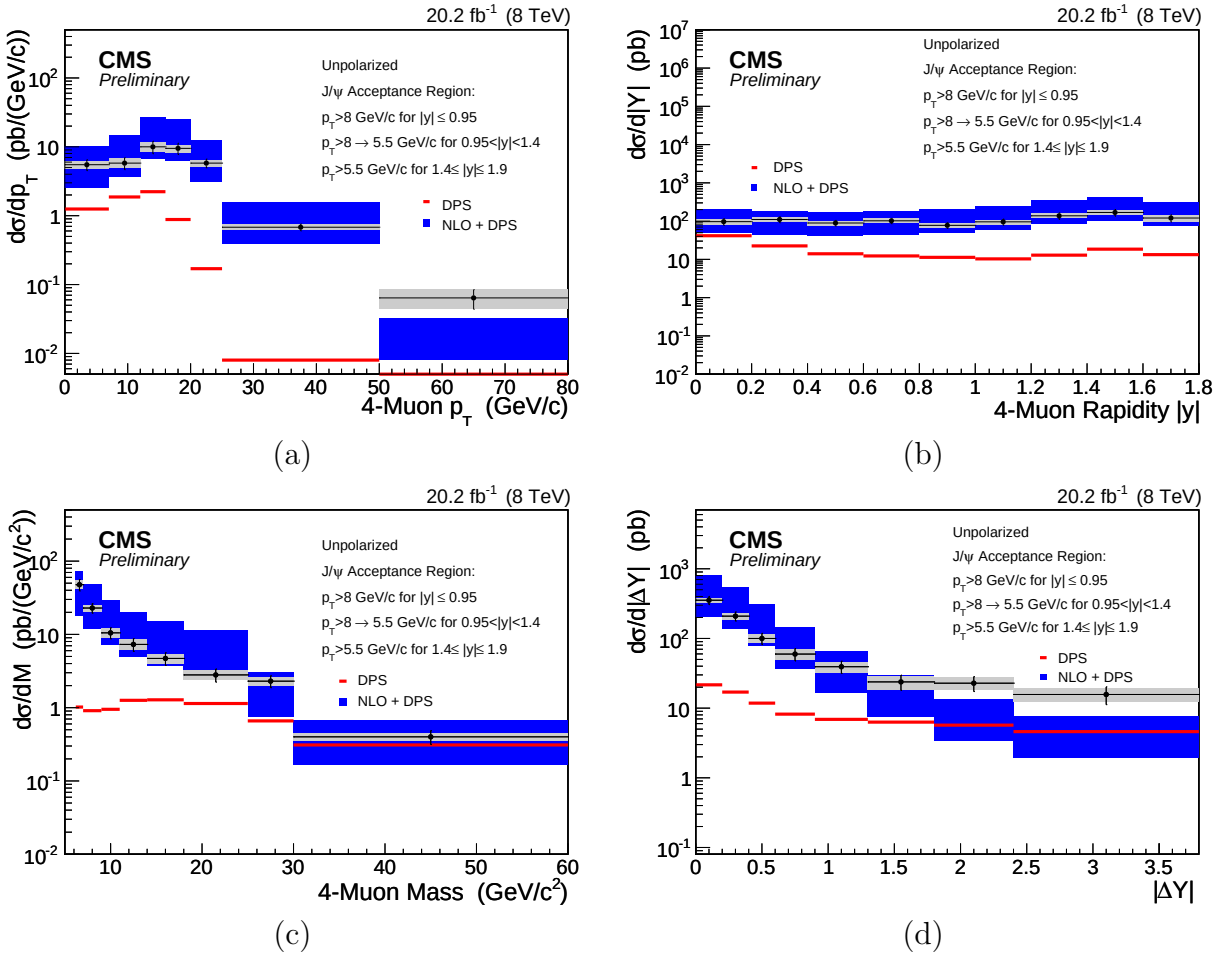



**Figure 4.23:** Differential cross section distributions for different 4-muon event variables, (a) transverse momentum, (b) the absolute value of the rapidity, (c) invariant mass, and (d) the absolute difference in rapidity between the two $J/\psi$. The points correspond to data, with statistical error shown as the gray box and the total uncertainty by the error bars. The NLO+DPS model is shown in blue with a model uncertainty of 60% as indicated by the blue boxes. The DPS contribution obtained relative to the cross section in data is shown in red without uncertainty.

cross section predictions. The sum of the MC samples is normalized to the measured cross section for the fit. The relative fraction between the DPS and SPS-NLO contributions is floated. Only the statistical uncertainty in data is taken into account for calculating the chisquare. The fit fraction of DPS is 18% of the total cross section. The DPS differential cross section is depicted by the red lines in the plots.

The DPS contribution can be compared to the fraction of DPS at reconstruction level of $f = 0.13 \pm 0.05$ estimated in Sec. 4.7.1, after the latter is corrected for acceptance and efficiency. The correction factor is $\omega = 0.015$ for DPS and $\omega' = 0.033$ for SPS-NLO. The corrected DPS fraction $F$ is given as:

$$F^{-1} = 1 + \frac{1-f}{f} \cdot frac\omega\omega' \tag{4.17}$$

It is estimated to be $F = 0.25 \pm 0.08$

In a second iteration, the absolute SPS-NLO differential cross section is predicted with the HELAC-Onia simulator [95] and scaled by a factor of 1.8 to account for contributions from decays of higher charmonium states as derived by the authors [82]. It is added to the DPS cross section obtained in the previous iteration described above. The SPS-NLO model uncertainty is estimated by changing the mass of the charm quark which is fixed at 3 GeV and by varying the PDF sets as used in [82]. The uncertainty for the DPS contribution estimate is added in quadrature. The relative model uncertainty is 60%. The predicted differential cross sections in different event variables are depicted by the blue boxes.

**Table 4.7:** Summary of the differential cross section measured in bins of 4-muon mass, $M^{JJ}$, listed together with the signal yield $N_{sig}$ extracted with a ML fit. The uncertainties are statistical first, then systematic.

| $M^{JJ} Bin(\mathrm{GeV}/c^2)$ | $d\sigma/dM^{JJ}(\ \mathrm{pb}/\mathrm{GeV}/c^2)$ | $N_{sig}$ |
|---|---|---|
| 6.2 - 7 | $47.3 \pm 6.3 \pm 5.6$ | $74 \pm 10$ |
| 7 - 9 | $22.8 \pm 2.4 \pm 2.3$ | $99 \pm 10$ |
| 9 - 11 | $10.5 \pm 1.5 \pm 1.0$ | $53 \pm 8$ |
| 11 - 14 | $7.3 \pm 1.2 \pm 0.8$ | $44 \pm 7$ |
| 14 - 18 | $4.7 \pm 0.7 \pm 0.6$ | $44 \pm 7$ |
| 18 - 25 | $2.7 \pm 0.4 \pm 0.4$ | $60 \pm 8$ |
| 25 - 30 | $2.3 \pm 0.3 \pm 0.3$ | $47 \pm 7$ |
| 30 - 60 | $0.4 \pm 0.05 \pm 0.07$ | $63 \pm 8$ |

**Table 4.8:** Summary of the differential cross section measured in bins of 4-muon transverse momentum, $p_{\mathrm{T}}^{JJ}$, listed together with the signal yield $N_{sig}$ extracted with a ML fit. The uncertainties are statistical first, then systematic.

| $p_{\mathrm{T}}^{JJ} Bin(\ \mathrm{GeV}/c)$ | $d\sigma/dp_{\mathrm{T}}^{JJ}(\ \mathrm{pb}/\ \mathrm{GeV}/c)$ | $N_{sig}$ |
|---|---|---|
| 0 - 7 | $5.5 \pm 0.7 \pm 0.7$ | $70 \pm 9$ |
| 7 - 12 | $5.8 \pm 0.9 \pm 0.7$ | $45 \pm 7$ |
| 12 - 16 | $9.8 \pm 1.6 \pm 1.3$ | $46 \pm 7$ |
| 16 - 20 | $9.5 \pm 1.2 \pm 1.3$ | $72 \pm 9$ |
| 20 - 25 | $5.7 \pm 0.6 \pm 0.6$ | $107 \pm 11$ |
| 25 - 50 | $0.7 \pm 0.06 \pm 0.05$ | $127 \pm 12$ |
| 50 - 80 | $0.06 \pm 0.019 \pm 0.003$ | $14 \pm 4$ |

**Table 4.9:** Summary of the differential cross section measured in bins of absolute 4-muon rapidity, $|y|$, listed together with the signal yield $N_{sig}$ extracted with a ML fit. The uncertainties are statistical first, then systematic.

| $\lvert y^{JJ}\rvert Bin$ | $d\sigma/d\lvert y^{JJ}\rvert(\ \mathrm{pb})$ | $N_{sig}$ |
|---|---|---|
| 0 - 0.2 | $96.6 \pm 14.9 \pm 11.7$ | $44 \pm 7$ |
| 0.2 - 0.4 | $110.2 \pm 15.6 \pm 11.7$ | $55 \pm 8$ |
| 0.4 - 0.6 | $89.0 \pm 12.4 \pm 8.5$ | $54 \pm 8$ |
| 0.6 - 0.8 | $101.5 \pm 13.6 \pm 9.1$ | $59 \pm 8$ |
| 0.8 - 1.0 | $77.4 \pm 10.9 \pm 7.5$ | $53 \pm 8$ |
| 1.0 - 1.2 | $95.5 \pm 14.2 \pm 10.3$ | $49 \pm 7$ |
| 1.2 - 1.4 | $137.2 \pm 17.4 \pm 19.8$ | $71 \pm 9$ |
| 1.4 - 1.6 | $167.9 \pm 22.9 \pm 23.8$ | $71 \pm 10$ |
| 1.6 - 1.8 | $120.1 \pm 22.7 \pm 10.8$ | $36 \pm 7$ |

**Table 4.10:** Summary of the differential cross section measured in bins of absolute difference in rapidity between the $J/\psi$, $|\Delta y|$, listed together with the signal yield $N_{sig}$ extracted with a ML fit. The uncertainties are statistical first, then systematic.

| $\lvert\Delta y\rvert Bin$ | $d\sigma/d\lvert\Delta y\rvert(\ \mathrm{pb})$ | $N_{sig}$ |
|---|---|---|
| 0 - 0.2 | $352.5 \pm 28.5 \pm 37.6$ | $178 \pm 14$ |
| 0.2 - 0.4 | $208.3 \pm 21.6 \pm 21.9$ | $102 \pm 11$ |
| 0.4 - 0.6 | $99.7 \pm 14.1 \pm 11.5$ | $56 \pm 8$ |
| 0.6 - 0.9 | $59.5 \pm 10.3 \pm 6.0$ | $40 \pm 7$ |
| 0.9 - 1.3 | $39.2 \pm 6.8 \pm 3.8$ | $35 \pm 6$ |
| 1.3 - 1.8 | $23.7 \pm 5.4 \pm 2.1$ | $23 \pm 5$ |
| 1.8 - 2.4 | $22.7 \pm 4.6 \pm 3.0$ | $25 \pm 5$ |
| 2.4 - 3.8 | $15.7 \pm 3.4 \pm 2.9$ | $23 \pm 5$ |

Also shown are the differential cross sections in four additional variables, the $\Delta\phi$ between the two $J/\psi$ the transverse momenta of the higher $p_{\mathrm{T}}$ (leading) $J/\psi$, and the subleading (lower $p_{\mathrm{T}}$) $J/\psi$, and the asymmetry between the individual $J/\psi$ $p_{\mathrm{T}}$ defined as $p_{\mathrm{T}}\mathcal{A} = |\frac{p_{\mathrm{T}}^{J_1} - p_{\mathrm{T}}^{J_2}}{p_{\mathrm{T}}^{J_1} + p_{\mathrm{T}}^{J_2}}|$.

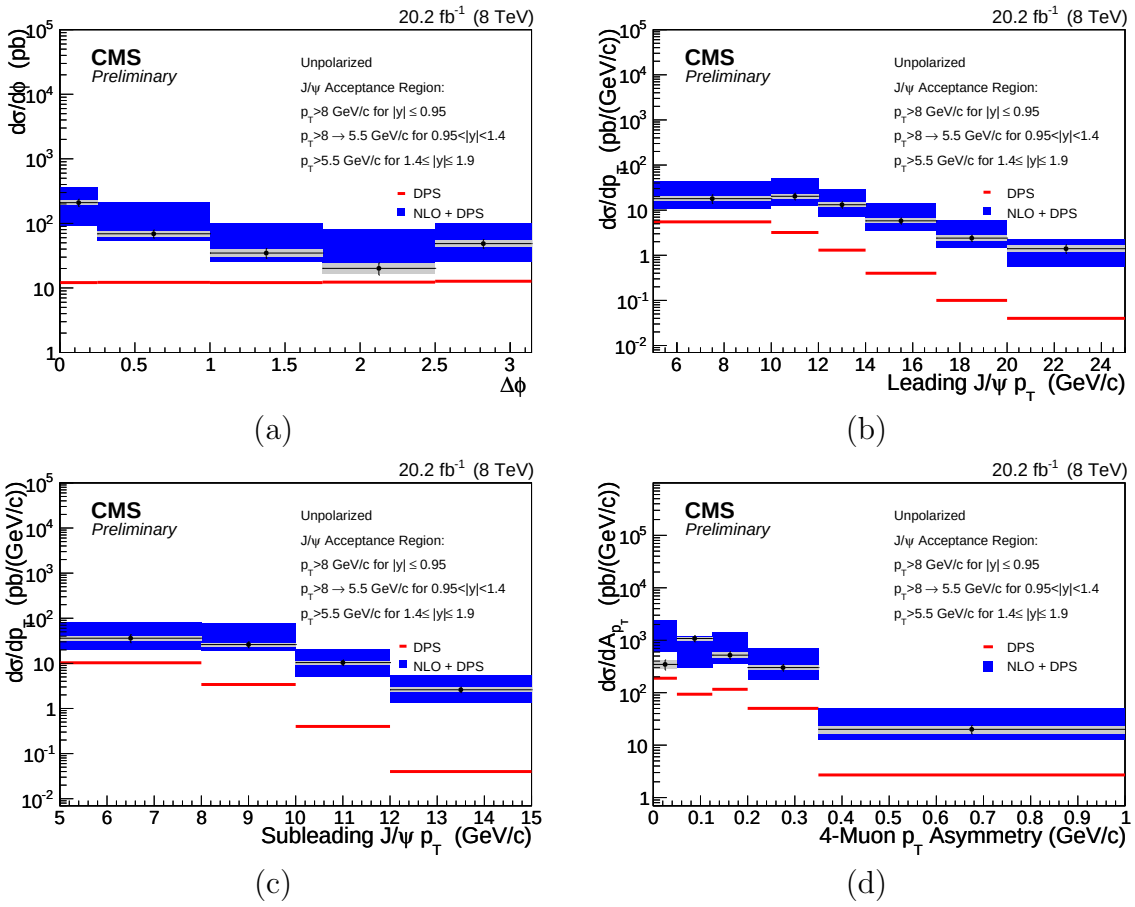



**Figure 4.24:** Differential cross section distributions for different 4-muon event variables, (a) the absolute difference in phi between the two $J/\psi$, (b) the transverse momentum of the leading $J/\psi$, (c) the transverse momentum of the subleading $J/\psi$, and (d) the asymmetry in $p_{\mathrm{T}}$ between the two $J/\psi$. The points correspond to data, with statistical error shown as the gray box and the total uncertainty by the error bars. The NLO+DPS model is shown in blue with a model uncertainty of 60% as indicated by the blue boxes. The DPS contribution obtained relative to the cross section in data is shown in red without uncertainty.

A summary of all integrated cross section values is shown in Table 4.15.

These values of total cross section have a spread which corresponds to an RMS of 9.6 pb. Integrating the variable distributions give 8 slightly different total cross section measurements. The difference is a consequence of evaluating the acceptance, efficiency and

**Table 4.11:** Summary of the differential cross section measured in bins of absolute difference in $\phi$ angle between the $J/\psi$, $|\Delta\phi|$, listed together with the signal yield $N_{sig}$ extracted with a ML fit. The uncertainties are statistical first, then systematic.

| $\lvert\Delta\phi\rvert Bin$ | $d\sigma/d\lvert\Delta\phi\rvert$( pb) | $N_{sig}$ |
|---|---|---|
| 0 - 0.25 | $209.5 \pm 17.9 \pm 20.8$ | $152 \pm 13$ |
| 0.25 - 1.0 | $69.0 \pm 6.4 \pm 7.7$ | $141 \pm 13$ |
| 1.0 - 1.75 | $34.7 \pm 4.8 \pm 3.6$ | $57 \pm 8$ |
| 1.75 - 2.5 | $20.1 \pm 3.6 \pm 2.3$ | $39 \pm 6$ |
| 2.5 - 3.142 | $48.6 \pm 5.3 \pm 5.5$ | $92 \pm 10$ |

**Table 4.12:** Summary of the differential cross section measured in bins of the transverse momentum momentum $p_{\mathrm{T}}^{J_1}$ for the high-$p_{\mathrm{T}}$ $J/\psi$, listed together with the signal yield $N_{sig}$ extracted with a ML fit. The uncertainties are statistical first, then systematic.

| $p_{\mathrm{T}}^{J_1} Bin$ | $d\sigma/dp_{\mathrm{T}}^{J_1}$( pb) | $N_{sig}$ |
|---|---|---|
| 5 - 10 | $18.0 \pm 2.2 \pm 3.3$ | $73 \pm 9$ |
| 10 - 12 | $20.3 \pm 2.2 \pm 2.7$ | $88 \pm 9$ |
| 12 - 14 | $13.2 \pm 1.5 \pm 1.5$ | $96 \pm 11$ |
| 14 - 17 | $5.8 \pm 0.64 \pm 0.6$ | $88 \pm 9$ |
| 17 - 20 | $2.4 \pm 0.33 \pm 0.2$ | $54 \pm 7$ |
| 20 - 25 | $1.4 \pm 0.22 \pm 0.2$ | $46 \pm 7$ |
| 25 - 60 | $0.14 \pm 0.03 \pm 0.03$ | $31 \pm 6$ |

**Table 4.13:** Summary of the differential cross section measured in bins of the transverse momentum $p_{\mathrm{T}}^{J_2}$ for the low-$p_{\mathrm{T}}$ $J/\psi$, listed together with the signal yield $N_{sig}$ extracted with a ML fit. The uncertainties are statistical first, then systematic.

| $p_{\mathrm{T}}^{J_2} Bin$ | $d\sigma/dp_{\mathrm{T}}^{J_2}$( pb) | $N_{sig}$ |
|---|---|---|
| 5 - 8 | $36.1 \pm 3.7 \pm 6.5$ | $108 \pm 11$ |
| 8 - 10 | $26.1 \pm 2.4 \pm 3.3$ | $126 \pm 12$ |
| 10 - 12 | $10.4 \pm 1.0 \pm 1.1$ | $123 \pm 12$ |
| 12 - 15 | $2.6 \pm 0.3 \pm 0.2$ | $76 \pm 9$ |
| 15 - 20 | $0.5 \pm 0.08 \pm 0.03$ | $36 \pm 6$ |
| 20 - 40 | $0.08 \pm 0.023 \pm 0.004$ | $11 \pm 3$ |

**Table 4.14:** Summary of the differential cross section measured in bins of The $p_{\mathrm{T}}$ asymmetry of the $J/\psi$, $p_{\mathrm{T}}^{J/\psi}\mathcal{A}$, together with the signal yield $N_{sig}$ extracted with a ML fit. The uncertainties are statistical first, then systematic.

| $p_{\mathrm{T}}^{J/\psi}\mathcal{A} Bin$ | $d\sigma/dp_{\mathrm{T}}^{J/\psi}\mathcal{A}$( pb) | $N_{sig}$ |
|---|---|---|
| 0 - 0.05 | $345.9 \pm 64.5 \pm 39.1$ | $34 \pm 6$ |
| 0.05 - 0.125 | $1079.7 \pm 81.7 \pm 124.6$ | $185 \pm 14$ |
| 0.125 - 0.2 | $519.3 \pm 57.1 \pm 60.6$ | $100 \pm 11$ |
| 0.2 - 0.35 | $301.3 \pm 28.8 \pm 32.0$ | $115 \pm 11$ |
| 0.35 - 1.0 | $20.0 \pm 3.3 \pm 1.7$ | $43 \pm 7$ |

**Table 4.15:** The integral of each differential cross section distribution. The uncertainty is statistical first, then systematic.

| Variable (X) | $d\sigma/dX^{JJ}$( pb) |
|---|---|
| $M^{JJ}$ | $187.7 \pm 9.4 \pm 23.2$ |
| $p_{\mathrm{T}}^{JJ}$ | $192.2 \pm 10.9 \pm 21.1$ |
| $\lvert y^{JJ}\rvert$ | $199.1 \pm 9.9 \pm 22.5$ |
| $\lvert\Delta y\rvert$ | $213.1 \pm 10.7 \pm 23.5$ |
| $\Delta\phi$ | $176.4 \pm 8.6 \pm 18.8$ |
| $p_{\mathrm{T}}^{J_1}$ | $193.2 \pm 12.7 \pm 25.2$ |
| $p_{\mathrm{T}}^{J_2}$ | $193.1 \pm 12.3 \pm 22.5$ |
| $p_{\mathrm{T}}^{J/\psi}(A)$ | $195.5 \pm 9.5 \pm 21.6$ |

total cross section in bins, with an independent binning for each variable. The total measured cross section is taken as the average of the two most uncorrelated variables, $p_{\mathrm{T}}$ and $|y|$ , however an average could be made using all 8 cross section integrals. The average for this collection would be 193.8 pb with an RMS of 9.6 pb.

## 4.11 Effective Cross Section

The measurement of a $\sigma_{eff}$, according to Eqn. 4.25, requires the single $J/\psi$ cross section measurement in the same acceptance regime as the $J/\psi$ pair measurement. The acceptance in this case is determined by the overlap between bins of the single $J/\psi$ cross section [76] and the measurement of the $J/\psi$ pair. The 7 TeV measurement of single $J/\psi$ is extrapolated to 8 TeV and scaled to the overlapping acceptance regime. The $p_{\mathrm{T}}^{J/\psi}$ and $|y^{J/\psi}|$ dependent region in the $J/\psi$ pair cross section acceptance cannot be replicated by scaling the 7 TeV measurement. Therefore, constant $p_{\mathrm{T}}$ cut is applied to the $J/\psi$ pair sample removing the region in question. For the measurement of $\sigma_{eff}$ made in this analysis, the $J/\psi$ acceptance is limited to the following regime for both single $J/\psi$ and $J/\psi$ pair production.

$$|y^{J/\psi}| \leq 1.9 \quad p_{\mathrm{T}}^{J/\psi} > 8.0\,\mathrm{GeV}/c \tag{4.18}$$

### 4.11.1 Single $J/\psi$ Cross Section Scaling

CMS has measured the single $J/\psi$ production cross section at both 7 TeV [76] and 13 TeV [57] center of mass energy. This section describes the derivation of scaling factors between different acceptances and cm energies. The scaling is based on the HELAC modeling of the single $J/\psi$ [95] production. Single $J/\psi$ are produced in HELAC according to a Crystal Ball function [65] in $p_{\mathrm{T}}^{J/\psi}$, and uniformly in $|y^{J/\psi}|$ separately. The user supplied acceptance cuts restrict the bounds of the distribution, and the total cross section is calculated. The $p_{\mathrm{T}}^{J/\psi}$ and $|y^{J/\psi}|$ are treated independently. The total scaling from the wider 7 TeV acceptance to the more restrictive acceptance in Eqn.4.18 is the product of the individual $p_{\mathrm{T}}^{J/\psi}$ and $|y^{J/\psi}|$ scales.

The scaling is calculated in each variable and compared to data to test this approach. The simulation uses 3 Crystal Ball functions to parameterize the $p_{\mathrm{T}}^{J/\psi}$ distribution derived from several measurements. The CDF[23] experiment taken alone, LHC (CMS[77], ATLAS[3], LHCb[7] combined) and a total combined LHC and CDF model. The maximum variation from the mean scaling calculated by the 3 PDFs is taken as systematic uncertainty.

The two 7 TeV measurements of CMS, [76, 77], have a partially overlapping acceptance. The overlapping range is

$$10 \leq p_{\mathrm{T}}^{J/\psi} \leq 30 \ \ \mathrm{GeV}/c \text{ and } |y^{J/\psi}| \leq 1.2\,. \tag{4.19}$$

with the measurements $\sigma_{J/\psi} = 115 \pm 7$ nb [77] and $\sigma_{J/\psi} = 109 \pm 29$ nb [76]. They are in agreement within their uncertainties. We use the second measurement as the 7 TeV baseline because it is conducted in a wider acceptance than the $J/\psi$ pair cross section, and the scaling in both $p_{\mathrm{T}}^{J/\psi}$ and $|y^{J/\psi}|$ can be interpolated, rather than extrapolated. The 13 TeV measurement of the single $J/\psi$ cross section [57] is provided in the acceptance range

$$20 \leq p_{\mathrm{T}}^{J/\psi} \leq 120 \ \ \mathrm{GeV}/c \text{ and } |y^{J/\psi}| \leq 1.2\,. \tag{4.20}$$

which completely overlaps with a portion of the 7 TeV measurement found in [77]. The ratio between the two measurements provides a cm energy scaling factor from $7 \rightarrow 13$ TeV. This ratio is measured at 25 points along the single $J/\psi$ $p_{\mathrm{T}}$ differential cross section [57] and a weighted average value is calculated. The average scaling factor of the cross section is measured to be 2.15 from $7 \rightarrow 13$ TeV using data. The models are used to generate single $J/\psi$ in the same acceptance range The scale from simulation is found to be 2.21 which is consistent with data within 3%.

The simulation is then used to predict the energy scaling from 7 to 8 TeV. A 3% systematic uncertainty is assigned due to the difference between data and model calculated energy scaling. The model predicts an increase in cross section from 7 to 8 TeV by a factor $1.15 \pm 0.03$.

The change in cross section with the $p_{\mathrm{T}}^{J/\psi}$ limit can be measured using 7 TeV data [76] in the intervals $6.5 \leq p_{\mathrm{T}}^{J/\psi}$ and $10.0 \leq p_{\mathrm{T}}^{J/\psi}$ using the bins present in the result. The cross section is found to increase by a factor of $6.3 \pm 0.7$ moving from the higher to the lower $p_{\mathrm{T}}^{J/\psi}$ cut. The model predicts $6.2 \pm 0.5$ which is within the data uncertainty. A relative systematic uncertainty of 8% is assigned due to the difference in the three PDFs used in the simulation. The cross section is simulated in the $p_{\mathrm{T}}^{J/\psi}$ interval for the 7 TeV measured

range of $6.5 \leq p_{\mathrm{T}}^{J/\psi}$ and the interval $8.0 \leq p_{\mathrm{T}}^{J/\psi}$ at 7 TeV. We obtain a $p_{\mathrm{T}}^{J/\psi}$ scale factor of $2.32 \pm 0.19$.

The scaling between the rapidity ranges is measured from [76] using the $|y^{J/\psi}| \leq 2.4$ and $|y^{J/\psi}| \leq 1.6$ regions. A factor of 1.4 is found. This scaling is reproduced by the model within the variation of the different PDFs.

According to the model, The cross section reduces by a factor of 1.22 from $|y^{J/\psi}| \leq 2.4$ to $|y^{J/\psi}| \leq 1.9$. With the assumption that the $|y^{J/\psi}|$ distribution is uniform, this factor is 2.4/1.9 which is within 4% of the model factor.

The cross section from Ref. [76] in the $6.5 \leq p_{\mathrm{T}}^{J/\psi} \leq 30$ interval is 1195 nb. It is divided by the total model generated scaling factor of 2.83 to estimate the interval $8 \leq p_{\mathrm{T}}^{J/\psi} \leq 30$ GeV/$c$ and $|y^{J/\psi}| \leq 1.9$. This produces a estimated cross section of 422.2 nb. The cross section scaling with the cm energy results in $\sigma_{J/\psi} = 485.5$ nb at 8 TeV. The relative statistical uncertainty on the single $J/\psi$ cross section is adopted from the measurement. The systematic uncertainty includes the following additional relative contributions: 3% for the energy scaling and 8% for the $p_{\mathrm{T}}$ scaling. The luminosity uncertainty has a refined value of 3.6% instead of 11% [87], calculated after the result was published. The estimate of the single $J/\psi$ cross section is:

$$\sigma_{J/\psi} = 485.5 \pm 14.6(stat) \pm 46.0(syst) \pm 17.5(lumi) \text{ nb.} \tag{4.21}$$

Alternatively, the range of the 7 TeV cross section measurement is divided into two ranges in transverse momentum, A) $6.5 < p_{\mathrm{T}}^{J/\psi} < 10$ GeV/$c$ and B) $10 < p_{\mathrm{T}}^{J/\psi} < 30$ GeV/$c$. The cross section in both ranges are scaled for the reduction of the rapidity acceptance. Furthermore, the range A) cross section is corrected for the change of the lower $p_{\mathrm{T}}^{J/\psi}$ limit from 6.5 GeV/$c$ to 8 GeV/$c$ as obtained from simulation [95]. The resulting single $J/\psi$ cross section agrees within 1%.

### 4.11.2 DPS Cross Section

The sample size of the DPS MC simulation is significantly reduced in this acceptance region. As the DPS process is simulated as independent 2-$J/\psi$ production, a data driven DPS sample by combining dimuons from different accepted events is made. Using data in this way ensures the kinematics of the $J/\psi$ remain the same and any correlations are avoided. The shuffled event sample is parameterized in the $|\Delta y|$ distribution by a polynomial. The PDF of the shuffled sample, shown in Fig. 4.25 compares well to the DPS MC shape. The SPS-NLO MC simulation distribution in $|\Delta y|$ is well described by an exponential decay.

The SPS and DPS parameterizations are used in a maximum likelihood fit to the $|\Delta y|$ distribution. $|\Delta y|$ is chosen to discriminate between the DPS and SPS-NLO sample because it is expected to be sensitive to the DPS contribution in high $|\Delta y|$ [82] due to the uncorrelated nature of the DPS production. The likelihood function for this fit is

$$l_j = N_{DPS}\left(P_{DPS}(|\Delta y|)\right) + N_{NLO}\left(P_{NLO}(|\Delta y|)\right) \tag{4.22}$$

The DPS-weighted distribution is then used in a second MLF with $J/\psi_2$ mass to extract the signal and background content. This fit is exactly the same as the fit described in Sec. 4.6 except the full sample is fit in 1-bin. The result of this fit is a sample of events which are weighted independently by DPS and signal likelihood. These DPS signal events are used as the measurement of the DPS production cross section in this acceptance region. As cross check rapidity and transverse momentum of the $J/\psi$ pair system are parameterized and used in a 2 dimensional MLF. DPS weights are extracted in the same way and the result is consistent within 5%. However, this method adds many more PDF parameters to describe the additional distributions and hence has a larger systematic uncertainty.

The total cross section of DPS is measured using the extracted signal weights from the MLFs described above. This value is then corrected by the DPS forward acceptance and efficiency from MC. The definition of uncertainties and their application are identical to the $J/\psi$ pair cross section measurement described in Sec. 4.9. The systematic uncertainties evaluated in the $J/\psi$ acceptance range for the effective cross section are listed in Table 4.16. The new terms due to the DPS fit are also included in the table. The DPS fit uncertainty

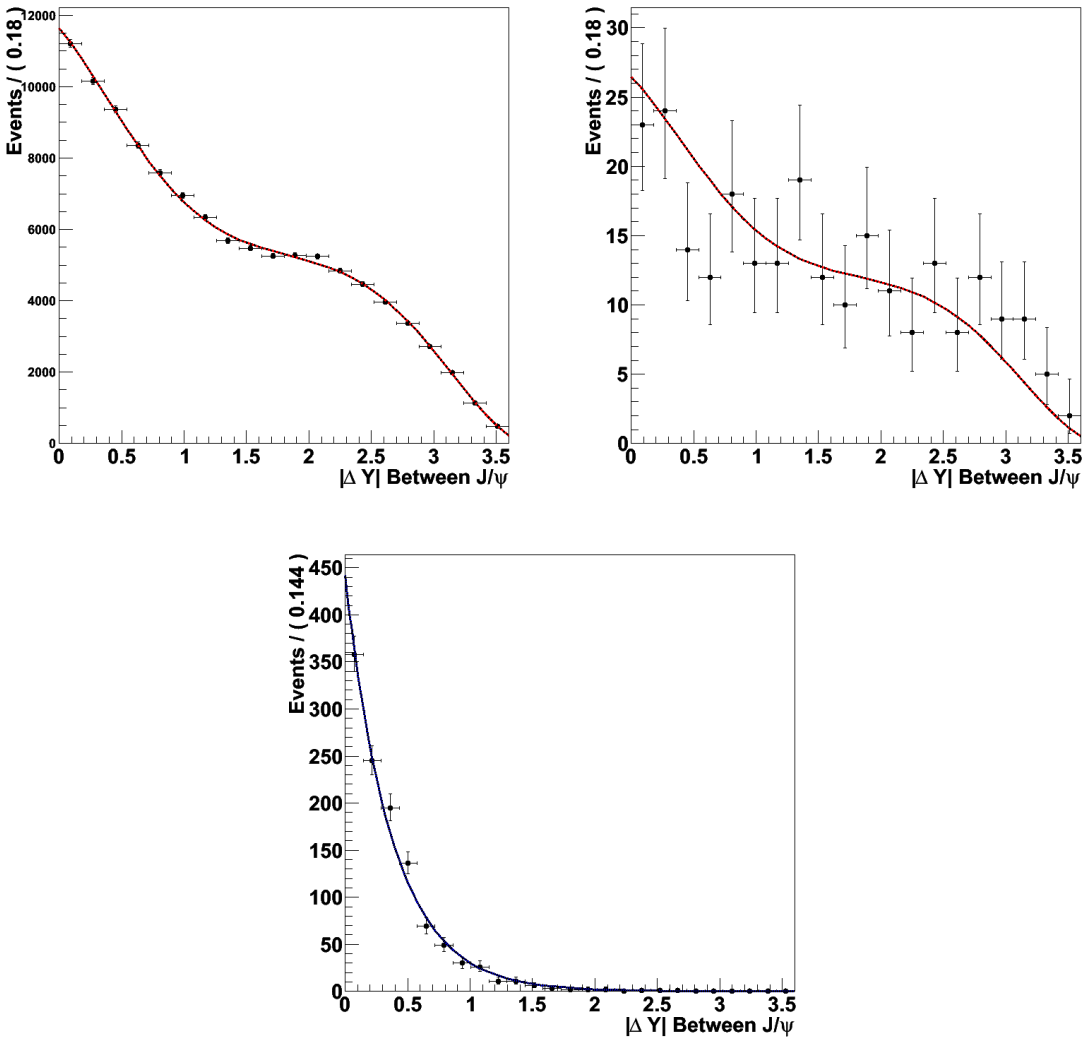



**Figure 4.25:** The top left plot shows the recombined data sample with a polynomial fit (line) on top. The same polynomial is shown in the top right plot on top of the low statistics reconstructed DPS MC sample (points with errors). This plot shows that the recombined shape still describes the original DPS MC. The bottom plot shows the exponential decay fit to reconstructed SPS-NLO events.

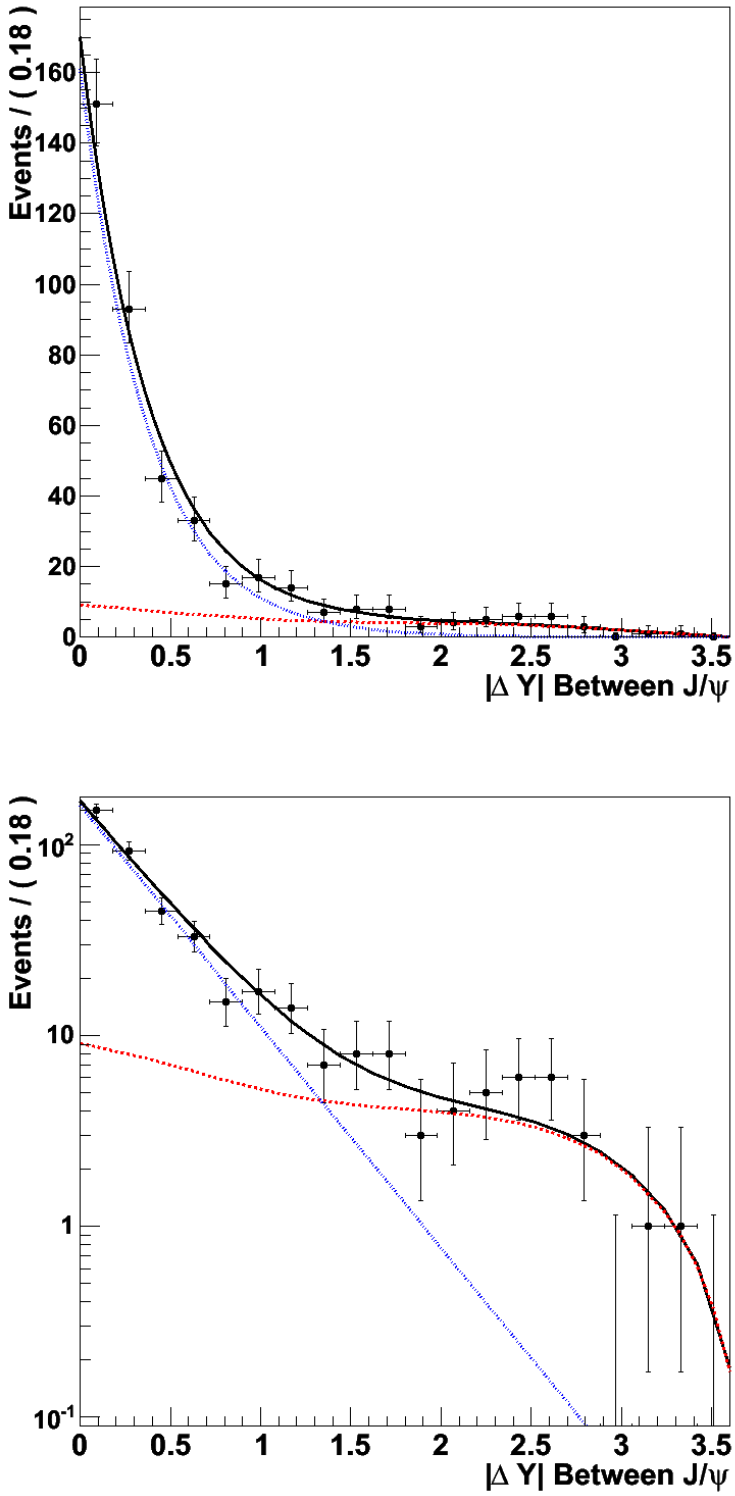



**Figure 4.26:** The plot on the top shows the data sample fit with the SPS (blue) and DPS (red) shapes. The bottom plot shows the same fit with a log scale.

is measured by varying the polynomial fit parameters within their uncertainties. The uncertainties are calculated during the fit to the shuffled DPS sample and correspond to the PDF uncertainty within the Poissonian error of the sample. Similarly, the SPS-NLO fit uncertainty is measured by varying the parameters of the SPS-NLO MC shape. The value for the cross section of DPS is found to be:

$$\sigma^{DPS}_{J/\psi J/\psi} = 25.6 \pm 3.7(stat) \pm 3.1(syst) \pm 0.7(lumi) \text{ pb} \tag{4.23}$$

within this acceptance regime.

**Table 4.16:** Summary of the relative systematic uncertainties.

| Source | Relative Uncertainty (%) |
|---|---|
| Muon Quality, ID and HLT | 9.7 |
| DPS fit uncertainty | 0.5 |
| SPS-NLO fit uncertainty | 4.1 |
| $J/\psi$ acceptance | 3.6 |
| MLF bkg-shape | 3.0 |
| MLF CB-shape | 3.2 |
| MLF fixed parameters | 0.5 |

### 4.11.3 Result

The effective cross section is calculated in the acceptance region defined by the kinematics of the $J/\psi$.

$$|y^{J/\psi}| \leq 1.9 \quad p_{\mathrm{T}}^{J/\psi} > 8.0\,\mathrm{GeV}/c \tag{4.24}$$

$$\sigma_{eff} = \frac{1}{2}\frac{\sigma J/\psi^2}{\sigma^{DPS}_{J/\psi J/\psi}} \tag{4.25}$$

Using Eqn. 4.25 to calculate the effective cross section, one finds that the branching fraction (and its uncertainty) cancels since $BF^2$ is a divisor of $\sigma^{DPS}_{J/\psi J/\psi}$ and $BF$ is a divisor of $\sigma_{J/\psi}$. The $J/\psi$ pair DPS cross section measurement is $\sigma^{DPS}_{J/\psi J/\psi} = 25.6 \pm 3.7(stat) \pm 3.1(syst) \pm 0.7(lumi)$ pb The scaled value of the single $J/\psi$ cross section at 8 TeV $\sigma_{J/\psi} = 485.5 \pm 14.6(stat) \pm 46.0(syst) \pm 17.5(lumi)$ nb. This results in the effective cross section for double

parton scattering of:

$$\sigma_{eff} = 4.6 \pm 0.7(stat) \pm 0.8(syst) \pm 0.2(lumi) \text{ mb} \tag{4.26}$$

The first uncertainty is of statistical nature, the second is systematic, and the third is due to the precision of the luminosity measurement at 7 TeV and 8 TeV cm energy.

# Chapter 5

# Conclusion

## 5.1 Review and Discussion

In this thesis several measurements of $J/\psi$ pair production using CMS data collected in 2012 at a cm energy of 8 TeV are presented. The $J/\psi$ pair differential cross section is measured in 8 kinematic variables. The total cross section is obtained from the integrals of 4-muon transverse momentum and absolute value of rapidity.

$$\sigma_{fid} = 195.7 \pm 11.1\ (stat) \pm 22.1\ (syst) \pm 5.1\ (lumi) \pm 2.3\ (BF)\ \text{pb}. \tag{5.1}$$

This result assumes unpolarized $J/\psi$ mesons. The $J/\psi$ polarization has been measured to be small in [21, 48, 22, 9, 50] and the $J/\psi$ pair polarization is yet unmeasured [12]. If $J/\psi$ polarization is varied by $\pm 20\%$ the relative change in the fiducial cross section is found to be $+11.4\%, -11.1\%$.

This measurement probes a high $p_{\mathrm{T}}$ region where contributions from higher order SPS production and color octet states are expected to become more significant [82]. Differential cross sections are compared to models for SPS at leading and next to leading order using the CTEQ6M PDF set [95]. The SPS MC sample is color singlet only and does not account for $J/\psi$ produced due to feed down from higher states. This is accounted for via a factor of 1.8 applied to the generator level distributions [82]. Hadronization is simulated with the Pythia8 generator using the same PDF set. DPS events are simulated and hadronized in Pythia8

using the CTEQ6L1 PDF set [97]. This simulation produces a double hard scattering event forced through the $J/\psi \to \mu^+\mu^-$ channel. The 4-muon transverse momentum and absolute value of rapidity differential cross sections are fit using the DPS and SPS distributions. The SPS-LO is found to contribute a negligible amount. The best fit yields the DPS contribution to 18% and the SPS-NLO contribution to 82%. The absolute differential cross section prediction for the SPS-NLO sample is then added to the DPS distribution. The model can be seen to fit well in most bins of the cross section, however it underestimates the data in the higher $J/\psi$ pair $p_{\mathrm{T}}$ and $|\Delta y|$. Higher order, i.e. NNLO production is expected to contribute at higher $J/\psi$ pair $p_{\mathrm{T}}$, as well as CO production which gains significance over CS when $J/\psi$ pair $p_{\mathrm{T}} > 50\,\mathrm{GeV}/c$ and when $|\Delta y| > 2.5$ [82]. Hence, this measurement helps to motivate higher order calculations. For example the NNLO process require evaluation of more than 2000 Feynman diagrams. Simulations of the contributions are still under development.

In the following paragraphs, the effective cross section, introduced in Chapter 4.11 is discussed. The $J/\psi$ pair measurements from other experiments, together with measurements in several different final states are displayed in Fig. 5.1. All measurements of the effective cross section have relatively high uncertainty, so no significant distinctions are made. More precise measurements are needed. The hadronic measurements are listed toward the top of the figure, while the quarkonia based values are at the bottom. These two categories can be seen to have different trends in $\sigma_{eff}$ where jet measurements tend toward higher effective cross sections than quarkonia. The measurement presented in this thesis supports this trend.

The value of the effective cross section measured in this thesis is

$$\sigma_{eff} = 4.6 \pm 0.7(stat) \pm 0.9(syst) \pm 0.2(lumi)\ \mathrm{mb} \tag{5.2}$$

within the $J/\psi$ acceptance $p_{\mathrm{T}}^{J/\psi} \geq 8\,\mathrm{GeV}/c$ and $|y^{J/\psi}| < 1.9$. This effective cross section can be compared to recent measurements from ATLAS which were performed using 8 TeV data. The ATLAS experiment measures $\sigma_{eff} = 6.3 \pm 1.6(stat) \pm 1.0(syst) \pm 0.1(BF) \pm 0.1(lumi)$ mb in the $J/\psi$ acceptance region $p_{\mathrm{T}}^{J/\psi} \geq 8.5\,\mathrm{GeV}/c$ and $|y^{J/\psi}| \leq 2.1$ [2]. The CMS and ATLAS measurements are consistent within the total uncertainty. The larger luminosity uncertainty in the CMS value is due to the single $J/\psi$ cross section measurement at 7 TeV that is based

on early data. CMS has also measured prompt $\Upsilon(1S)$ pair production for the first time at 8 TeV [56] in the acceptance defined by $p_{\mathrm{T}}^{\Upsilon} \leq 50\,\mathrm{GeV}/c$ and $|y^{\Upsilon}| < 2.0$. This measurement can be combined with the single $\Upsilon(1S)$ cross section measured in [49]. The single $\Upsilon$ cross section measures within the $\Upsilon$ pair acceptance is found to be $\sigma_{\Upsilon} * BR = 7.5$ nb. It can be estimated, assuming a range of DPS contributions from 10% to 30% that the effective cross section, $\sigma_{eff}$ ranges from 2.2 - 6.6 mb [70]. This estimate is shown on the summary plot Fig. 5.1 as a point with error bars, where the error bars represent the spread of effective cross section values due to the estimated range of the DPS fraction. The CMS value of the effective cross section for $J/\psi$ pair production at a cm energy of 7 TeV is the result of a fit to CMS data [103] and a predicted single $J/\psi$ production cross section [82]. It is calculated to be $\sigma_{eff} = 8.2 \pm 2.0 \pm 2.9$ mb. The first uncertainty combines the $J/\psi$ pair data and SPS theory uncertainty, while the second originates from the single $J/\psi$ template model. This value is also in agreement with the measurement made in this thesis. The LHCb experiment measures the $J/\psi$ pair production cross section at a cm energy of 13 TeV in a complementary acceptance to CMS of $p_{\mathrm{T}}^{J/\psi} \leq 10\,\mathrm{GeV}/c$ and $2.0 < |y^{J/\psi}| < 4.5$ [12]. The effective cross section is estimated by fitting each kinematic variable with one of 3 different SPS models and a DPS model. The resulting $\sigma_{eff}$ measurements range from $9.2 \pm 3.9$ mb to $14.4 \pm 4.9$ mb. This measurement is indicated in the plot by a point with errors which encompasses the range of $9.2 - 3.9 \rightarrow 14.4 + 4.9$ i.e. the maximum range of uncertainty. The measured values are higher than the other $J/\psi$ pair measurements shown in the plot. This may be due to the LHCb acceptance which includes lower $p_{\mathrm{T}}$ and higher $|y^{J/\psi}|$ than CMS. This probes a different range of partonic $p_{\mathrm{T}}$ values, and a region of production due to less central collisions. Two measurements from the D0 experiment are also included, a $J/\psi$ pair final state and a $J/\psi$ $+\Upsilon$. The $J/\psi$ pair value is consistent with the measurement in this thesis, the $J/\psi$ $+\Upsilon$ measurement is lower. $J/\psi$ $+\Upsilon$, unlike other quarkonia production, is expected to be dominated by DPS[16]. The $J/\psi$ $+\Upsilon$ cross section is measured in the acceptance $p_{\mathrm{T}}^{J/\psi} > 2\,\mathrm{GeV}/c$ and $|y^{J/\psi}| < 2.0$.

Further up the summary plot are 5 LHCb measurements[11, 8] including a $J/\psi$ or $\Upsilon$ meson and one so called open charm (C) meson. The $\Upsilon + C$ measurement is an average of 4 effective cross section measurements, the $\Upsilon + D^0$ 7 TeV, $\Upsilon + D^+$ 7 TeV, $\Upsilon + D^0$ 8 TeV and

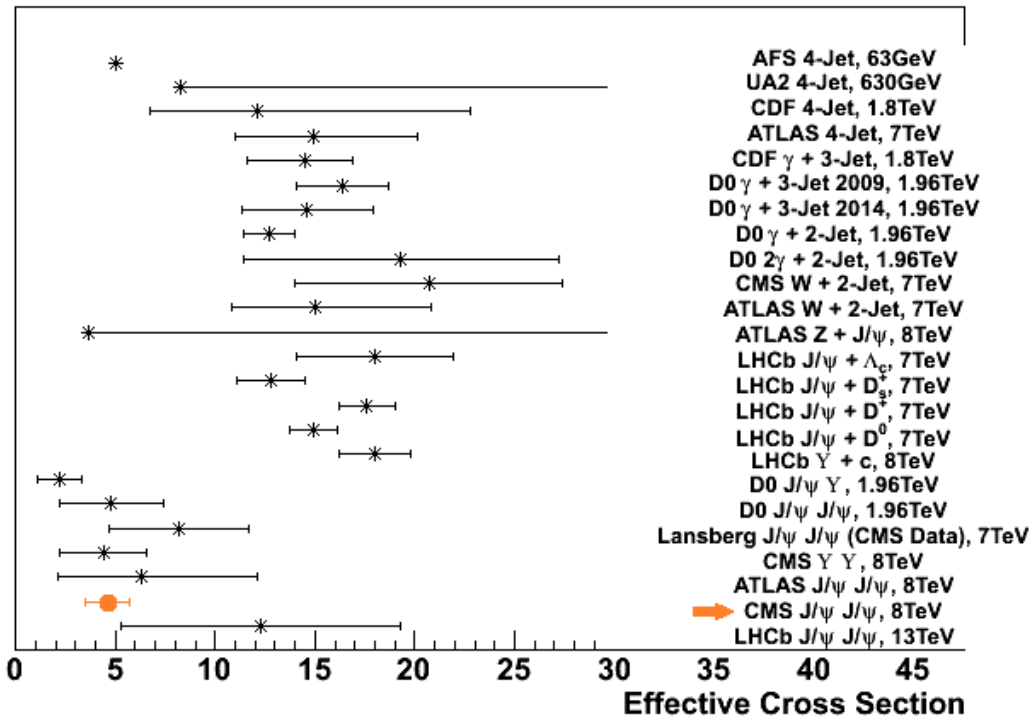



**Figure 5.1:** Effective cross section values from different experiments at various center of mass energies and for different final states. Values measured by the UA2 experiment [58], AFS experiment [24], ATLAS experiment [1, 4, 6, 2], the LHCb experiment [11, 8, 12], The D0 experiment [15, 16, 18, 13, 14], the CDF experiment [20, 19] and the CMS experiment [82, 51, 56]. The measurement made in this thesis is marked with orange.

$\Upsilon + D^+$ 8 TeV. All were made within the acceptance $p_{\mathrm{T}}^{\Upsilon} < 15\,\mathrm{GeV}/c$, $2.0 < |y^{\Upsilon}| < 4.5$, $1 < p_{\mathrm{T}}^{C} < 20\,\mathrm{GeV}/c$ and $2.0 < |y^{C}| < 4.5$. The $J/\psi$ and associated open charm were measured at 7 TeV in the acceptance $p_{\mathrm{T}}^{J/\psi} < 12\,\mathrm{GeV}/c$, $2.0 < |y^{J/\psi}| < 4.0$, $3 < p_{\mathrm{T}}^{C} < 12\,\mathrm{GeV}/c$ and $2.0 < |y^{C}| < 4.0$. The open charm in the final state can originate from the sea quarks in the interacting protons [8], in contrast to pure charmonium final states which probe only the gluon content of the pp interaction. In addition, the $\Upsilon + C$ is expected to be dominated by DPS production [11].

The next measurement in the plot is the ATLAS measurement of associated $Z + J/\psi$ production[6]. This final state is measured in the acceptance $p_{\mathrm{T}}^{J/\psi} > 8.5\,\mathrm{GeV}/c$ and $|y^{J/\psi}| < 2.1$. The inclusion of a vector boson probes a higher interaction energy than the lighter $J/\psi$ pair production. The associated final state is also expected to have significantly higher contribution from CO production than $J/\psi$ pair [6].

Next are two measurements of the associated production of a $W + 2jets$, which can result from gluon-gluon or quark-gluon interactions. The CMS and ATLAS measurements of $W + 2jets$ require the jets to have $p_{\mathrm{T}} > 20\,\mathrm{GeV}/c$, which samples a different kinematic regime than the $J/\psi$ pair measurement. The high $p_{\mathrm{T}}$ of the final state indicates higher parton transverse momentum, and can be sampled by the central region of the detector.

The next 5 measurements of effective cross section utilize a $\gamma + jets$ final state. The $\gamma + jet$ production mainly occurs through quark-gluon scattering in a Compton type reaction, $qg \to q\gamma$, and in a quark-quark annihilation process $q\bar{q} \to g\gamma$. The use of the $\gamma$ provides a greater sensitivity than 4 jet measurements due to the better resolution of gamma reconstruction [14]. The two production reactions allow this final state to probe multiple types of double parton interactions.

Finally, at the top of the figure are the 4-jet final state measurements. 4-jet measurements probe the production of di-jet pairs, or 3-jet + 1-jet in combination. This measurement probes the DPS production through the $|\Delta y^{jet}|$ variable. DPS is modeled as 2 independent hard scatters which populate the high $|\Delta y^{jet}|$ and low $p_{\mathrm{T}}^{2-jet}$ regions. The 4-jet channel probes very high parton $p_{\mathrm{T}}$, as jet $p_{\mathrm{T}}$ is generally required to be higher than $20\,\mathrm{GeV}/c$, with the ATLAS measurement requiring one jet with $p_{\mathrm{T}} > 42.5\,\mathrm{GeV}/c$ [1].

The trend in the effective cross section between jet based and quarkonia based measurements is not yet established[82]. The effective cross section calculation in Eqn. 4.25 assumes that $\sigma_{eff}$ is independent of cm energy and final state process. However, there is no theoretical need for this to be the case. The simulation of $J/\psi$ pair DPS assumes uncorrelated production, effectively using two single $J/\psi$ producers simultaneously. The PDFs used by this producer are developed only for single parton interactions. Introducing correlations to produce specific multi-parton generators is a work in progress. It is also possible that PDFs which include no parton transverse momentum terms are not descriptive enough to correctly model DPS cross sections. A concise summary of the development of transverse momentum dependent parton distribution functions is available in [25].

The values of effective cross sections are consistent among the quarkonia pair measurements, that tend to be lower than measurements made using other final states. Also there is no significant dependence on the cm energy. However, such behavior could become more apparent with higher precision measurements.

## 5.2 Summary and Outlook

The cross section for the prompt production of $J/\psi$ meson pairs in proton-proton (pp) collisions at $\sqrt{s} = 8$ TeV from a sample corresponding to an integrated luminosity of $20.2 \pm 0.5$ fb$^{-1}$is measured with the CMS detector at the LHC . It provides unique insight into particle production and proton structure in pp collisions. The two $J/\psi$ mesons are fully reconstructed in their $\mu^+\mu^-$ decay. An acceptance region is defined by the individual $J/\psi$ transverse momentum $p_{\mathrm{T}}^{J/\psi}$ and rapidity $|y^{J/\psi}|$. The total fiducial cross section assuming unpolarized prompt $J/\psi$ pair production is found to be

$$\sigma_{fid} = 195.7 \pm 11.1\ (stat) \pm 22.1\ (syst) \pm 5.1\ (lumi) \pm 2.3\ (BF)\ \text{pb}. \tag{5.3}$$

In addition, the single $J/\psi$ production cross section scaling is estimated from theory and applied to data. Single $J/\psi$ production is compared to the pair production via DPS and

quantified via an effective cross section.

$$\sigma_{eff} = 4.6 \pm 0.7(stat) \pm 0.8(syst) \pm 0.2(lumi) \text{ mb} \tag{5.4}$$

These results show the significant contribution of DPS production in the $J/\psi$ pair final state. Model builders can use the differential cross section measurements to develop the production modeling more thoroughly, including partonic $p_{\mathrm{T}}$ distributions in the initial state and double parton PDFs which appropriately account for correlations between partons. Also, higher order SPS and color octet production models can be developed which may account for the mismatch in the high bins of 4-muon $p_{\mathrm{T}}$ and $|\Delta y|$. The better understanding of these modes of non resonant $J/\psi$ pair production allows for tighter background constraints in resonance searches. Several resonances are predicted to decay through the $J/\psi$ pair channel. Multi quark states such as tetra-quarks are allowed in the SM due to their color neutrality. If a bound state of $c\bar{c}c\bar{c}$ exists, a $J/\psi$ pair decay is expected [35]. Models also predicts a light pseudo-scalar Higgs [61] not part of the SM which can decay through two $J/\psi$. The 4-Muon mass distribution is inspected as a part of the cross section measurement and no significant excesses are found.

The effective cross section measurement can be made using 13 TeV data taken in 2016-17 with CMS to test the assumed energy independence. Also measurements of $J/\psi + \Upsilon$ can be made with more statistics to test the DPS contribution dominance in that channel. Studies of the relative polarization of the two $J/\psi$ can be performed through an angular analysis of the final state muons. This final state will benefit from the increased statistics and higher center of mass energy in available in future runs of the LHC.

# Bibliography

[1] Aaboud, M. et al. (2016). Study of hard double-parton scattering in four-jet events in pp collisions at $\sqrt{s} = 7$ TeV with the ATLAS experiment. *JHEP*, 11:110. xxi, 103, 104

[2] Aaboud, M. et al. (2017). Measurement of the prompt J/ $\psi$ pair production cross-section in pp collisions at $\sqrt{s} = 8$ TeV with the ATLAS detector. *Eur. Phys. J.*, C77(2):76. xxi, 101, 103

[3] Aad, G. et al. (2011). Measurement of the differential cross-sections of inclusive, prompt and non-prompt $J/\psi$ production in proton-proton collisions at $\sqrt{s} = 7$ TeV. *Nucl. Phys.*, B850:387–444. 92

[4] Aad, G. et al. (2013a). Measurement of hard double-parton interactions in $W(\rightarrow l\nu)+$ 2 jet events at $\sqrt{s}$=7 TeV with the ATLAS detector. *New J. Phys.*, 15:033038. xxi, 103

[5] Aad, G. et al. (2013b). Measurement of hard double-parton interactions in $W(\rightarrow l\nu)+$ 2 jet events at $\sqrt{s}$=7 TeV with the ATLAS detector. *New J. Phys.*, 15:033038. 49

[6] Aad, G. et al. (2015). Observation and measurements of the production of prompt and non-prompt $J/\psi$ mesons in association with a $Z$ boson in $pp$ collisions at $\sqrt{s} = 8$ TeV with the ATLAS detector. *Eur. Phys. J.*, C75(5):229. xxi, 103, 104

[7] Aaij, R. et al. (2011). Measurement of $J/\psi$ production in $pp$ collisions at $\sqrt{s} = 7$ TeV. *Eur. Phys. J.*, C71:1645. 92

[8] Aaij, R. et al. (2012). Observation of double charm production involving open charm in pp collisions at $\sqrt{s}$=7 TeV. *JHEP*, 1206:141. xxi, 102, 103, 104

[9] Aaij, R. et al. (2013). Measurement of $J/\psi$ polarization in $pp$ collisions at $\sqrt{s} = 7$ TeV. *Eur. Phys. J.*, C73(11):2631. 50, 77, 100

[10] Aaij, R. et al. (2014). Measurement of $\psi(2S)$ polarisation in $pp$ collisions at $\sqrt{s} = 7$ TeV. *Eur. Phys. J.*, C74(5):2872. 50

[11] Aaij, R. et al. (2016). Production of associated Y and open charm hadrons in pp collisions at $\sqrt{s} = 7$ and 8 TeV via double parton scattering. *JHEP*, 07:052. xxi, 102, 103, 104

[12] Aaij, R. et al. (2017). Measurement of the J/$\psi$ pair production cross-section in pp collisions at $\sqrt{s} = 13$ TeV. *JHEP*, 06:047. [Erratum: JHEP10,068(2017)]. xxi, 100, 102, 103

[13] Abazov, V. M. et al. (2010). Double parton interactions in $\gamma$+3 jet events in $pp^-$ bar collisions $\sqrt{s} = 1.96$ TeV. *Phys. Rev.*, D81:052012. xxi, 103

[14] Abazov, V. M. et al. (2014a). Double parton interactions in $\gamma + 3$ jet and $\gamma + b/cjet + 2$ jet events in $p\bar{p}$ collisions at $\sqrt{s} = 1.96$ TeV. *Phys. Rev.*, D89(7):072006. xxi, 49, 103, 104

[15] Abazov, V. M. et al. (2014b). Observation and studies of double $J/\psi$ production at the Tevatron. *Phys. Rev.*, D90(11):111101. xxi, 49, 103

[16] Abazov, V. M. et al. (2016a). Evidence for simultaneous production of $J/\psi$ and $\Upsilon$ mesons. *Phys. Rev. Lett.*, 116(8):082002. xxi, 49, 102, 103

[17] Abazov, V. M. et al. (2016b). Evidence for simultaneous production of $J/\psi$ and $\Upsilon$ mesons. *Phys. Rev. Lett.*, 116(8):082002. 47

[18] Abazov, V. M. et al. (2016c). Study of double parton interactions in diphoton + dijet events in $p\bar{p}$ collisions at $\sqrt{s} = 1.96$ TeV. *Phys. Rev.*, D93(5):052008. xxi, 49, 103

[19] Abe, F. e. (1993). Study of four-jet events and evidence for double parton interactions in $p\overline{p}$ collisions at $\sqrt{s} = 1.8$ tev. *Phys. Rev. D*, 47:4857–4871. xxi, 103

[20] Abe, F. e. (1997). Measurement of double parton scattering in $\overline{p}p$ collisions at $\sqrt{s} = 1.8tev$. *Phys. Rev. Lett.*, 79:584–589. xxi, 103

[21] Abelev, B. et al. (2012). $J/\psi$ polarization in $pp$ collisions at $\sqrt{s} = 7$ TeV. *Phys. Rev. Lett.*, 108:082001. 50, 77, 100

[22] Abulencia, A. et al. (2007). Polarization of $J/\psi$ and $\psi_{2S}$ mesons produced in $p\bar{p}$ collisions at $\sqrt{s} = 1.96$-TeV. *Phys. Rev. Lett.*, 99:132001. 77, 100

[23] Acosta, D. et al. (2005). Measurement of the $J/\psi$ meson and $b-$hadron production cross sections in $p\bar{p}$ collisions at $\sqrt{s} = 1960$ GeV. *Phys. Rev.*, D71:032001. 92

[24] Akesson, T. et al. (1987). Double Parton Scattering in $pp$ Collisions at $\sqrt{s} = 63$-GeV. *Z. Phys.*, C34:163. xxi, 103

[25] Angeles-Martinez, R. et al. (2015). Transverse Momentum Dependent (TMD) parton distribution functions: status and prospects. *Acta Phys. Polon.*, B46(12):2501–2534. 105

[26] Artoisenet, P., Lansberg, J., and Maltoni, F. (2007). Hadroproduction of $J/\psi$ and $\upsilon$ in association with a heavy-quark pair. *Phys.Lett.*, B653:60–66. 46

[27] Badier, J. et al. (1982). Evidence for $\psi\psi$ Production in $\pi^-$ Interactions at 150-GeV/$c$ and 280-GeV/$c$. *Phys.Lett.*, B114:457. 46

[28] Badier, J. et al. (1985). $\psi\psi$ Production and Limits on Beauty Meson Production From 400-GeV/$c$ Protons. *Phys.Lett.*, B158:85. 46

[29] Baier, R. and Ruckl, R. (1981). Hadronic Production of J/psi and Upsilon: Transverse Momentum Distributions. *Phys. Lett.*, B102:364–370. 46

[30] Baier, R. and Ruckl, R. (1983). Hadronic Collisions: A Quarkonium Factory. *Z. Phys.*, C19:251. 46

[31] Baranov, S. P., Snigirev, A. M., and Zotov, N. P. (2011). Double heavy meson production through double parton scattering in hadronic collisions. *Phys. Lett.*, B705:116–119. 47

[32] Baranov, S. P., Snigirev, A. M., Zotov, N. P., Szczurek, A., and Schafer, W. (2013). Interparticle correlations in the production of $J/\psi$ pairs in proton-proton collisions. *Phys. Rev.*, D87(3):034035. 47

[33] Barbero, M. e. (2004). Design and test of the cms pixel readout chip. 517:349–359. 34

[34] Bentele, B., Cumalat, J. P., Schaeffer, D., Wagner, S. R., Riley, G., and Spanier, S. (2016). Rate dependence, polarization, and light sensitivity of neutron-irradiated scCVD diamond sensors. *Nuclear Instruments and Methods in Physics Research A*, 838:74–81. 36, 40

[35] Berezhnoy, A., Likhoded, A., Luchinsky, A., and Novoselov, A. (2011). Double J/psi-meson Production at LHC and 4c-tetraquark state. *Phys.Rev.*, D84:094023. 46, 53, 106

[36] Berezhnoy, A., Likhoded, A., Luchinsky, A., and Novoselov, A. (2012). Double $c\bar{c}$ production at LHCb. *Phys.Rev.*, D86:034017. 47

[37] Blok, B., Dokshitzer, Y., Frankfurt, L., and Strikman, M. (2014a). Perturbative qcd correlations in multi-parton collisions. *The European Physical Journal C*, 74(6):2926. 47

[38] Blok, B., Dokshitzer, Yu., Frankfurt, L., and Strikman, M. (2014b). Perturbative QCD correlations in multi-parton collisions. *Eur. Phys. J.*, C74:2926. 49

[39] Bodwin, G. T., Braaten, E., and Lepage, G. P. (1995). Rigorous QCD analysis of inclusive annihilation and production of heavy quarkonium. *Phys. Rev.*, D51:1125–1171. [Erratum: Phys. Rev.D55,5853(1997)]. 46

[40] Boslaugh, S. (2012). *Statistics in a Nutshell, 2nd Edition*. O'Reilly Media, Incorporated. 57

[41] Brüning, O. S., Collier, P., Lebrun, P., Myers, S., Ostojic, R., Poole, J., and Proudlock, P. (2004). *LHC Design Report*. CERN Yellow Reports: Monographs. CERN, Geneva. 11

[42] Calucci, G. and Treleani, D. (1998). Mini - jets and the two-body parton correlation. *Phys. Rev.*, D57:503–511. 47

[43] Calucci, G. and Treleani, D. (1999). Proton structure in transverse space and the effective cross-section. *Phys. Rev.*, D60:054023. 47

[44] Campbell, J. M., Maltoni, F., and Tramontano, F. (2007). QCD corrections to J/psi and Upsilon production at hadron colliders. *Phys.Rev.Lett.*, 98:252002. 46

[45] Chang, C.-H. (1980). Hadronic Production of $J/\psi$ Associated With a Gluon. *Nucl. Phys.*, B172:425–434. 46

[46] Chatrchyan, S. et al. (2008). The CMS Experiment at the CERN LHC. *JINST*, 3:S08004. 16, 24

[47] Chatrchyan, S. et al. (2012). Observation of a new boson at a mass of 125 GeV with the CMS experiment at the LHC. *Phys. Lett.*, B716:30–61. 1, 3

[48] Chatrchyan, S. et al. (2013a). Measurement of the prompt $J/\psi$ and $\psi$(2S) polarizations in $pp$ collisions at $\sqrt{s} = 7$ TeV. *Phys. Lett.*, B727:381–402. 50, 77, 100

[49] Chatrchyan, S. et al. (2013b). Measurement of the $\Upsilon(1S), \Upsilon(2S)$, and $\Upsilon(3S)$ cross sections in pp collisions at $\sqrt{s} = 7$ TeV. *Phys. Lett.*, B727:101–125. 102

[50] Chatrchyan, S. et al. (2013c). Measurement of the $Y(1S), Y(2S)$ and $Y(3S)$ polarizations in $pp$ collisions at $\sqrt{s} = 7$ TeV. *Phys. Rev. Lett.*, 110(8):081802. 50, 75, 77, 100

[51] Chatrchyan, S. et al. (2014). Study of double parton scattering using W + 2-jet events in proton-proton collisions at $\sqrt{s} = 7$ TeV. *JHEP*, 03:032. xxi, 49, 103

[52] CMS Collaboration (2010a). Commissioning and performance of the cms pixel tracker with cosmic ray muons. *Journal of Instrumentation*, 5(03):T03007. 19

[53] CMS Collaboration (2010b). Measurement of tracking efficiency. CMS Physics Analysis Summary CMS-PAS-TRK-10-002, CERN. 72

[54] CMS Collaboration (2013). Cms luminosity based on pixel cluster counting - summer 2013 update. CMS Physics Analysis Summary CMS-PAS-LUM-13-001, CERN. 31, 51, 82

[55] CMS Collaboration (2016). Dimuon spectrum 2016. (CMS-DP-2016-059). 26

[56] CMS Collaboration (2016a). Observation of double Upsilon at CMS. xxi, 102, 103

[57] CMS Collaboration (2016b). Quarkonium production cross sections in pp collisions at $\sqrt{s} = 13$ TeV. 92, 93

[58] Collaboration, U. (1991). A study of multi-jet events at the cern pp collider and a search for double parton scattering. *Physics Letters B*, 268(1):145 – 154. xxi, 103

[59] Contardo, D., Klute, M., Mans, J., Silvestris, L., and Butler, J. (2015). Technical Proposal for the Phase-II Upgrade of the CMS Detector. Technical Report CERN-LHCC-2015-010. LHCC-P-008. CMS-TDR-15-02, Geneva. Upgrade Project Leader Deputies: Lucia Silvestris (INFN-Bari), Jeremy Mans (University of Minnesota) Additional contacts: Lucia.Silvestris@cern.ch, Jeremy.Mans@cern.ch. 30

[60] Del Fabbro, A. and Treleani, D. (2001). Scale factor in double parton collisions and parton densities in transverse space. *Phys. Rev.*, D63:057901. 47

[61] Dermisek, R. and Gunion, J. F. (2005). Escaping the large fine tuning and little hierarchy problems in the next to minimal supersymmetric model and h –¿ aa decays. *Phys.Rev.Lett.*, 95:041801. 106

[62] Diehl, M., Kasemets, T., and Keane, S. (2014). Correlations in double parton distributions: effects of evolution. *JHEP*, 05:118. 49

[63] Dimopoulos, S. and Georgi, H. (1981). Softly broken supersymmetry and su(5). *Nuclear Physics B*, 193(1):150 – 162. 4

[64] Fruhwirth, R. (1987). Application of Kalman filtering to track and vertex fitting. *Nucl.Instrum.Meth.*, A262:444–450. 27, 53, 54

[65] Gaiser, J. E. (1982). *Charmonium Spectroscopy From Radiative Decays of the $J/\psi$ and $\psi'$*. PhD thesis, SLAC. 65, 81, 92

[66] Glashow, S. L. (1961). Partial Symmetries of Weak Interactions. *Nucl. Phys.*, 22:579–588. 6

[67] Gong, B. and Wang, J.-X. (2008). QCD corrections to polarization of $J/\psi$ and $\upsilon$ at Tevatron and LHC. *Phys.Rev.*, D78:074011. 46

[68] Greenberg, O. W. (1964). Spin and unitary-spin independence in a paraquark model of baryons and mesons. *Phys. Rev. Lett.*, 13:598–602. 4

[69] Griffiths, D. (2005). *Introduction to Quantum Mechanics*. Pearson international edition. Pearson Prentice Hall. 2, 3

[70] Haytmyradov, M. (2017). *The First Observation Of* $\Upsilon$*(1s) Pair Production And Hadron Calorimetry Upgrade At Cms*. PhD thesis, University of Iowa. 102

[71] Humpert, B. and Mery, P. (1983). psi psi PRODUCTION AT COLLIDER ENERGIES. *Z.Phys.*, C20:83. 46

[72] Kagan, H., Roe, S., and Weilhammer, P. (2008). RD42 Status Report: Development of Diamond Tracking Detectors for High Luminosity Experiments at the LHC. Technical Report LHCC-RD-016. CERN-LHCC-2008-005, CERN, Geneva. 37

[73] Karbach, T. M. and Schlupp, M. (2012). Constraints on Yield Parameters in Extended Maximum Likelihood Fits. 59

[74] Kartvelishvili, V. G. and Esakiya, S. M. (1983). ON HADRON INDUCED PRODUCTION OF J / PSI MESON PAIRS. (IN RUSSIAN). *Yad. Fiz.*, 38:722–726. 46

[75] Kasemets, T. and Diehl, M. (2013). Angular correlations in the double Drell-Yan process. *JHEP*, 01:121. 49

[76] Khachatryan, V. et al. (2011). Prompt and non-prompt $J/\psi$ production in $pp$ collisions at $\sqrt{s} = 7$ TeV. *Eur. Phys. J.*, C71:1575. 92, 93, 94

[77] Khachatryan, V. et al. (2015). Measurement of $J/\psi$ and $\psi(2S)$ Prompt Double-Differential Cross Sections in pp Collisions at $\sqrt{s}$=7 TeV. *Phys. Rev. Lett.*, 114(19):191802. 92, 93

[78] Ko, P., Yu, C., and Lee, J. (2011). Inclusive double-quarkonium production at the Large Hadron Collider. *JHEP*, 1101:070. 46, 47

[79] Kom, C., Kulesza, A., and Stirling, W. (2011). Pair Production of J/psi as a Probe of Double Parton Scattering at LHCb. *Phys.Rev.Lett.*, 107:082002. 47

[80] Kornmayer, A. (2016). The cms pixel luminosity telescope. *Nuclear Instruments and Methods in Physics Research Section A: Accelerators, Spectrometers, Detectors and*

*Associated Equipment*, 824(Supplement C):304 – 306. Frontier Detectors for Frontier Physics: Proceedings of the 13th Pisa Meeting on Advanced Detectors. 32

[81] Lansberg, J.-P. and Shao, H.-S. (2013). Production of $J/\psi + \eta_c$ versus $J/\psi + J/\psi$ at the LHC: Importance of Real $\alpha_s^5$ Corrections. *Phys. Rev. Lett.*, 111:122001. 46

[82] Lansberg, J.-P. and Shao, H.-S. (2015). $J/\psi$-pair production at large momenta: Indications for double parton scatterings and large $\alpha_s^5$ contributions. *Phys. Lett.*, B751:479–486. xxi, 46, 47, 69, 87, 95, 100, 101, 102, 103, 105

[83] Leonard, J. L. (2014). Luminosity measurement at CMS. *PoS*, TIPP2014:348. 31

[84] Li, R., Zhang, Y.-J., and Chao, K.-T. (2009). Pair Production of Heavy Quarkonium and B(c)(*) Mesons at Hadron Colliders. *Phys. Rev.*, D80:014020. 46

[85] Li, Y.-J., Xu, G.-Z., Liu, K.-Y., and Zhang, Y.-J. (2013). Relativistic Correction to J/psi and Upsilon Pair Production. *JHEP*, 07:051. 46

[86] Lujan, P. (2017). https://twiki.cern.ch/twiki/bin/view/CMSPublic/PLTPerformanceRun2. 36

[87] Marlow, D. e. a. (2011). Absolute calibration of luminosity measurement at cms. *CMS Note*. 94

[88] Mohr, P. J., Newell, D. B., and Taylor, B. N. (2016). Codata recommended values of the fundamental physical constants: 2014. *Rev. Mod. Phys.*, 88:035009. 6

[89] Mulders, M. et al. (2008). Muon identification in cms. *CMS Note*, , http://cms.cern.ch/iCMS/jsp/openfile.jsp?tp=draft&files=AN2008_098_v1.pdf. 53

[90] Patrignani, C. et al. (2016). Review of Particle Physics. *Chin. Phys.*, C40(10):100001. 50, 82

[91] Pernegger, H., Roe, S., Weilhammer, P., Eremin, V., Frais-K?lbl, H., Griesmayer, E., Kagan, H., Schnetzer, S., Stone, R., Trischuk, W., Twitchen, D., and Whitehead, A. (2005). Charge-carrier properties in synthetic single-crystal diamond measured with the transient-current technique. *Journal of Applied Physics*, 97(7):073704. 41, 42

[92] Qiao, C.-F., Sun, L.-P., and Sun, P. (2010). Testing Charmonium Production Mechamism via Polarized J/psi Pair Production at the LHC. *J.Phys.G*, G37:075019. 46

[93] Salam, A. (1968). Weak and Electromagnetic Interactions. *Conf. Proc.*, C680519:367–377. 6

[94] Shao, H.-S. (2013). HELAC-Onia: An automatic matrix element generator for heavy quarkonium physics. *Comput. Phys. Commun.*, 184:2562–2570. 52

[95] Shao, H.-S. (2016). HELAC-Onia 2.0: an upgraded matrix-element and event generator for heavy quarkonium physics. *Comput. Phys. Commun.*, 198:238–259. 52, 85, 87, 92, 94, 100

[96] Sjostrand, T., Mrenna, S., and Skands, P. Z. (2006). PYTHIA 6.4 Physics and Manual. *JHEP*, 0605:026. 53

[97] Sjostrand, T., Mrenna, S., and Skands, P. Z. (2008). A Brief Introduction to PYTHIA 8.1. *Comput.Phys.Commun.*, 178:852–867. 52, 101

[98] Sun, L.-P., Han, H., and Chao, K.-T. (2016). Impact of $J/\psi$ pair production at the LHC and predictions in nonrelativistic QCD. *Phys. Rev.*, D94(7):074033. 46

[99] Taylor, L. and McCauley, T. (2011). CMS collision events (7 TeV): candidate ZZ to 2e+2mu. CMS Collection. xv, 29

[100] The CMS Collaboration (2012). Performance of CMS muon reconstruction in pp collision events at $\sqrt{s} = 7TeV$. *Journal of Instrumentation*, 7:2P. 54, 69, 72

[101] The CMS Collaboration (2013). The performance of the CMS muon detector in proton-proton collisions at $\sqrt{s} = 7$ TeV at the LHC. *JINST*, 8(arXiv:1306.6905. CMS-MUO-11-001. CERN-PH-EP-2013-072):P11002. 101. 27

[102] The CMS Collaboration (2014a). Description and performance of track and primary-vertex reconstruction with the CMS tracker. *JINST*, 9(arXiv:1405.6569. CERN-PH-EP-2014-070. CMS-TRK-11-001):P10009. 80 p. 27

[103] The CMS Collaboration (2014b). Measurement of prompt $J/\psi$ pair production in pp collisions at $\sqrt{s} = 7$ Tev. *JHEP*, 09:094. 47, 60, 61, 69, 102

[104] van der Meer, S. (1968). Calibration of the Effective Beam Height in the ISR. 30

[105] Verkerke, W. and Kirkby, D. (2003). The RooFit toolkit for data modeling. *ArXiv Physics e-prints*. 60

[106] Veszpremi, V. (2015). Radiation experience with the cms pixel detector. *Journal of Instrumentation*, 10(04):C04039. 19

[107] Vogt, R. and Brodsky, S. (1995). Intrinsic charm contribution to double quarkonium hadroproduction. *Phys.Lett.*, B349:569–575. 46

[108] Weinberg, S. (1967). A model of leptons. *Phys. Rev. Lett.*, 19:1264–1266. 2, 6

[109] Wöhri, H., Krätschmer, I., Zhang, L., Knünz, V., Faccioli, P., Lourenço, C., and Abbiendi, G. (2012). Low $p_t$ muon and dimuon efficiencies. CMS Note 2012/088, CERN. 55, 74, 75

# Vita

Grant Riley was born on August 29, 1989. He attended Buckeye Senior High School in Valley City, Ohio and graduated in 2007. He then enrolled in Miami University (OH), and completed a B.S. in Physics in 2011. Grant was then accepted into the Ph.D. candidate program at the University of Tennessee, Knoxville where he served as a T.A. for one year before joining the CMS group and beginning his thesis research.